Osaka University Knowledge Archive

Title	Energy spectrum and topological gap labeling in two-dimensional quasi-periodic systems
Author(s)	岡, 裕樹
Citation	大阪大学, 2024, 博士論文
Version Type	VoR
URL	https://doi.org/10.18910/96377
rights	
Note	

Osaka University Knowledge Archive : OUKA

https://ir.library.osaka-u.ac.jp/

Osaka University

Doctoral Thesis

Energy spectrum and topological gap labeling in two-dimensional quasi-periodic systems

Hiroki Oka

Department of Physics
Osaka University

2024

Contents

List of publications **5**

1 Introduction **7**

1.1 Purpose of the Study 7

1.2 Moiré stacking of two-dimensional materials 9

1.2.1 Twisted bilayer graphene 10

1.2.2 Graphene/hBN heterostructures 12

1.3 Moiré trilayer systems 14

1.4 1D Quasi-crystalline and Hofstadter's butterfly 16

2 Theoretical Backgrounds **21**

2.1 Electronic Properties of Graphene Layer(s) 21

2.2 Interlayer coupling between lattice mismatched layers 25

2.3 Twisted bilayer graphene 27

2.4 Graphene/hBN heterostructure 31

3 hBN/Graphene/hBN **35**

3.1 Commensurate approximation 35

3.2 Hamilotonian 39

3.3 Results 42

3.3.1 Electronic spectrum 42

3.3.2 Topological invariants for band gaps 47

3.4 Quasi-Brillouin Zone 52

4 Twisted quasicrystal **57**

4.1 Zone quantum numbers 58

4.1.1 General formulation 58

4.1.2 Example: Twisted triangular potentials 59

4.1.3 Quasi Brillouin zones 64

4.2 Adiabatic charge pumping 69

4.2.1 1D systems 70

4.2.2 2D systems 71

4.3 4D quantum Hall effect and the second Chern numbers 74

5 Conclusion **81**

Acknowledgement **99**

List of publications

- Paper I

Fractal energy gaps and topological invariants in hBN/graphene/hBN double moiré systems

Hiroki Oka, and Mikito Koshino

Physical Review B **104**, 035306 (2021)

- Paper II

Topological invariants in two-dimensional quasicrystals

Mikito Koshino, and Hiroki Oka

Physical Review Research **4**, 013028 (2022)

Chapter 1

Introduction

1.1 Purpose of the Study

Since the experimental synthesis of graphene in 2004 [1], extensive research has been conducted on various two-dimensional materials [2, 3]. One particularly notable focus in recent years has been on composite two-dimensional materials [4, 5, 6, 7, 8, 9, 10, 11, 12, 13, 14, 15, 16, 17, 18, 19, 20, 21, 22, 23], such as moiré superlattices like twisted bilayer graphene (TBG). When two-dimensional materials are stacked with a slight twist, it creates a solid-state system with a substantially large periodic structure, recognized as a moiré pattern. The moiré periodicity, which varies depending on the twist angle, gives rise to unique properties that are never observed in individual atomic layers. For exapmle, a twisted bilayer graphene (TBG) stacked with a so-called magic angle about 1 degree was shown to exhibit superconductivity and correlated insulating phases [12, 13, 17, 16]. The exploration of moiré materials were also extended to various two-dimensional materials, such as hexagonal boron-nitride (hBN) and transition metal dichalcogenides.

Recent advancements in experiments have enabled the creation of three-layered structures from various two-dimensional materials [24, 25, 26, 27, 28, 29, 30, 31]. In contrast to bilayer systems, a three-layer system is characterized

by two twist angles, resulting in double moiré structure. The two moiré patterns are typically not aligned, exhibiting a quasi-periodicity referred to as a moire-of-moiré pattern. Describing the physical properties arising from the dual periodic structures is a challenging problem, since the conventional band theories based on the periodicity do not apply to these systems. Hence, a new approach is needed to characterize the quasi-periodic properties of two-dimensional systems.

This study explores the energy spectrum and topological gap labeling in quasi-periodic double moiré systems. As a representative example, we calculate the electronic band structure of hBN/graphene/hBN trilayer system as a function of twist angles [32, 33]. We find that the energy spectrum exhibits a fractal pattern with multiple mini-gaps that continuously change with the twist angle. Moreover, each mini-gap is found to be characterized by a unique set of topological integers, which are associated with multiple Brillouin zones arising from the multiple periodicity. Finally we extend our analysis to general two-dimensional quasi-periodic systems, and establish that the numbers characterizing energy gaps can are regarded as topological invariant of four-dimensional quantum Hall effect, by a formal mapping to higher dimensional systems.

The thesis is organized as follows. In the rest of this chapter, we review the previous works on moiré two-dimensional materials and quasi-crystalline systems with double periodicity. Chapter 2 provides a theoretical basis to describe electronic structures of graphene, hBN, and a graphene/hBN single-moiré system. In chapter 3, we introduce methodologies of calculation of hBN/graphene/hBN trilayer system by commensurate approximant method. Then we show the typical band structures of the trilayer system, and the twist-angle dependence of the electric spectrum. We identify characteristic integers for each band gap, which corresponds to quasi-Brillouin zones. In chapter 4, we describe the topological nature of the characteristic integers by considering adiabatic charge pumping and four-dimensional quantum Hall effect. The formulation shows the integers can be expressed as second Chern numbers. Finally, we conclude this thesis in chapter 5.

1.2 Moiré stacking of two-dimensional materials

Since the successful isolation of graphene [1], extensive research has been conducted on a variety of two-dimensional (2D) materials. Graphene is an atomic-layer material where carbon atoms are arranged in a honeycomb lattice, exhibiting high charge mobility arising from the Dirac-particle nature of electrons. Additionally, various types of two-dimensional materials, such as hexagonal boron nitride (hBN) [34] and transition metal dichalcogenides (TMDCs), were also intensively investigated. These two-dimensional materials exhibit properties distinct from their bulk (3D) counterparts, showcasing unique characteristics.

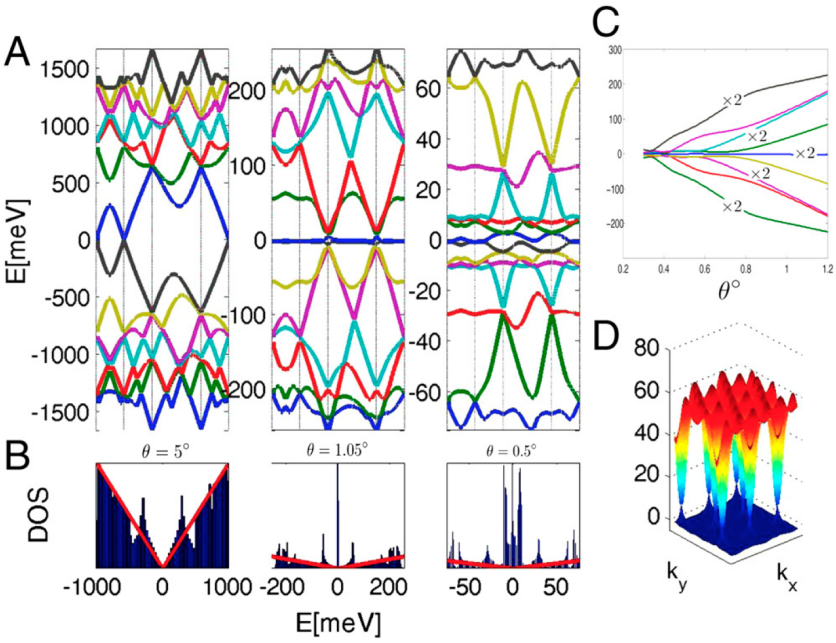

Figure 1.1: Twist angle dependence of the energy bands in twisted bilayer graphene [9].

In recent years, there has been active investigation into moiré 2D materials, which are created by stacking 2D materials in an incommensurate manner. In these materials, a rotational misalignment and/or lattice mismatch between stacked materials give rise to a moiré interference pattern, leading to various physical phenomena depending on the twist angle between the layers. In the case

of twisted bilayer graphene [19, 4, 5, 6, 7, 18, 19, 21, 22, 23], for instance, it was experimentally shown that the system with a specific stacking angle led to a superconducting state [8, 9, 10, 11, 12, 14, 15, 16, 17]. This striking example demonstrated that the moiré superlattice effect not only modulates the original physical properties, but also gives rise to novel emergent phenomena that were inaccessible in monolayer graphene. Following this discovery, various moiré systems comprised of diverse 2D materials have been extensively investigated to uncover novel properties not present in the individual monolayers.

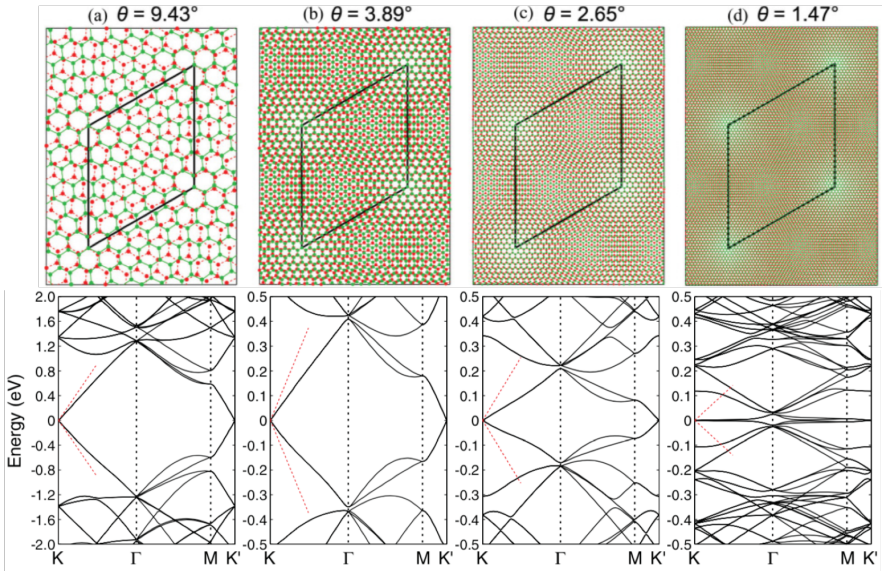

Figure 1.2: The moiré unit-cells and the band structures of twisted bilayer graphene in different twist angles [23].

1.2.1 Twisted bilayer graphene

When two graphene layers are stacked on top of each other, the interlayer twist angle θ assumes a pivotal role in determining the electronic structures. This configuration of twisted bilayer graphene (TBG) inherently embodies a quasiperiodic nature, arising from the mutual irrationality in lattice periods between the individual graphene layers. Nevertheless, for relatively small values of θ (less than approximately 10°), the low-energy physics is primarily governed by the long-

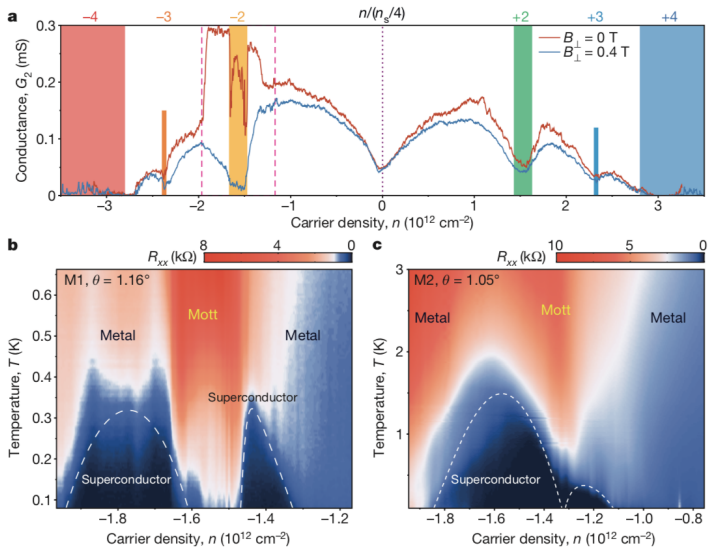

Figure 1.3: TBG shows superconductivity in magic angle [12]

range moiré interference pattern, and the electronic properties can be effectively described through the moiré effective theory [4, 5, 6, 22, 23]. In essence, this effective theory approximates TBG as a translationally symmetric system, with the moiré period dominating its behavior. The observed phenomena in the low-angle regime, encompassing the formation of flat bands [8, 9, 12, 13, 14, 15, 16, 17] and the manifestation of the Hofstadter butterfly under the influence of a magnetic field [10, 35, 36], can be well explained within the framework of the moiré effective theory.

Conversely, in TBG characterized by a large θ, the moiré period is comparable to the atomic length scale, yielding a quasiperiodic behavior. Particularly, when $\theta = 30°$, the superposed hexagonal lattices transform into a 12-fold rotationally symmetric quasicrystalline lattice in absense of translational symmetry, as initially elucidated by Stampfli [38]. Recently, TBG with an accurately controlled rotation angle of 30° has been experimentally realized in epitaxially grown samples on the SiC surface, and its electronic spectrum has been measured. Furthermore, similar TBGs have been fabricated on the Ni surface using a transfer method. Additionally, another stack of atomic layers rotated by 30° has been suc-

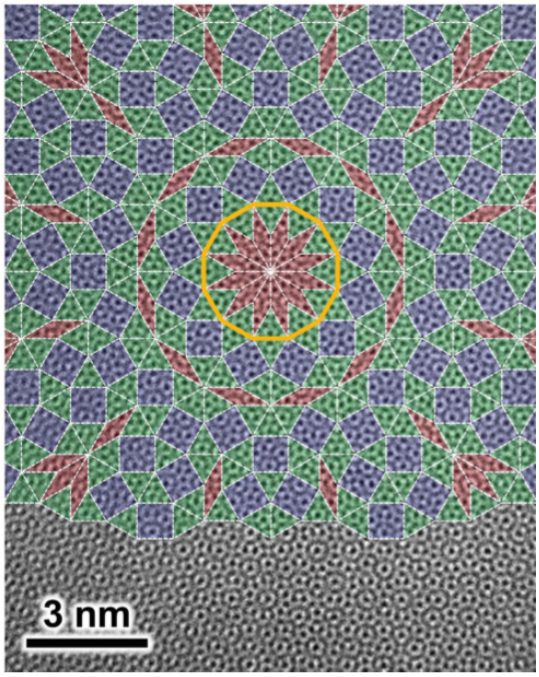

Figure 1.4: 12-fold rotationally symmetric quasicrystalline lattice in 30° twist-stacked graphene layers [37].

cessfully achieved by depositing graphene on top of the BN layer and the MoSe2 bilayer system. In the realm of such quasicrystalline TBG (QC-TBG), the aforementioned moiré effective theory proves inadequate, as its primary postulate that the moiré pattern governs the system no longer holds valid. There have been several theoretical attempts to describe the electronic structure of the 30° TBG by unconventional approach beyond the Bloch framework [39, 40, 37, 41, 42].

1.2.2 Graphene/hBN heterostructures

Another representative example of the moiré superlattices is a compose system formed by stacking graphene on top of hBN [34, 43, 44, 45, 46, 47, 48, 49, 50, 51, 34, 52, 17, 49, 48, 53, 54, 55, 56, 57, 58, 59]. Although sharing a common structural arrangement, hBN differs from graphene in a placement of distinct boron and nitrogen atoms on A and B sublattices, leading to the introduction of an insulating energy gap in its electronic structure. Even in a non-rotated stack-

ing, graphene/hBN system has an moiré pattern attributed to a 1.8% lattice mismatch. The electronic structure of graphene-hBN bilayer is primarily dominated by graphene's low-energy spectrum, since the wide energy gap of hBN. However, the superlattice potential significantly reshapes graphene's Dirac cone, resulting in the emergence of the primary gap in the charge neutral point as well as mini-Dirac bands in the electron and hole sides [51]. The intricate mini-band structure of the system can be described by an effective continuum model, akin to the method employed for TBG [43, 44, 45, 46, 47].

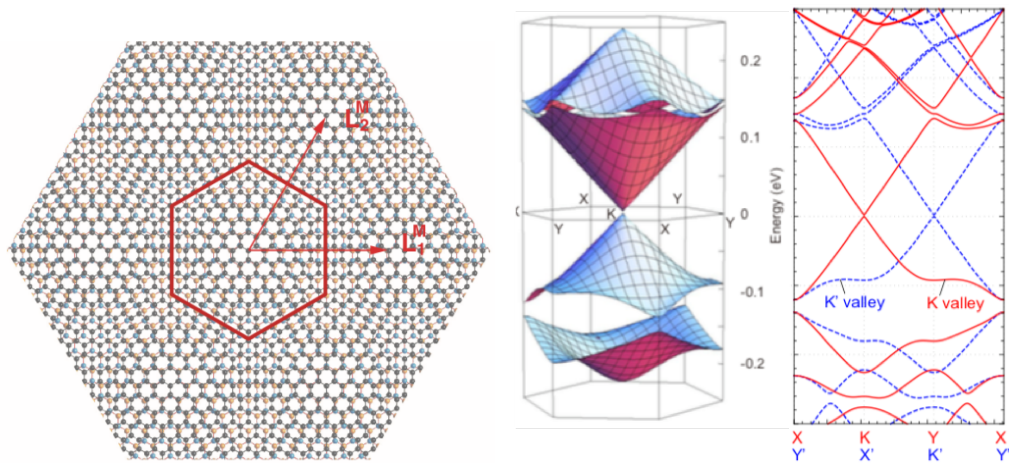

(a) (b)

Figure 1.5: (a) The atomically crystalline of a graphene layer and a hBN layer by no-twisted stacking. (b) The energy band structure of graphene/hBN bilayer system [47].

When a magnetic field weaves its influence into the multilayer fabric boasting an incommensurate moiré pattern, the energy spectrum metamorphoses into a self-similar fractal structure referred to as the Hofstadter butterfly [60]. The complicated spectral structure arises from the interplay between Bragg's reflection within the periodic potential and the cyclotron motion induced by the magnetic field. It is noteworthy that the fractal gap structure and the associated quantum Hall effect have been first observed within the graphene-hBN moiré structure [50, 48].

1.3 Moiré trilayer systems

In addition to basic moiré bilayer systems, attention has also directed towards trilayer configurations [24, 25, 26, 27, 30, 31, 28, 29]. Twisted trilayer graphene (TTG) [61, 62, 63, 64, 65, 66, 67], akin to its bilayer counterpart TBG, exhibits the remarkable phenomenon of superconductivity at the magic angle, where an intricate interplay of three Dirac cones adds an additional complexity in the phenomena. Moreover, the exploration of trilayer systems extends to heterostructures comprising different 2D materials. In particular, trilayer assemblies hBN-graphene-hBN layers exhibit a complicated minigap structures distinct from its bilayer counterpart [24, 25, 26, 27, 28, 29, 68].

Central to these trilayer systems is the concept of dual moiré patterns. The independent twist angles between upper and lower bilayers give rise to distinctive moiré superlattices, giving rise to an inherent incommensurability, which is rarely encountered in conventional crystal structures [25, 26]. This departure from the familiar periodicity is a hallmark of quasi-periodic systems, reminiscent of the intricacies found in quasicrystals [69, 70, 71, 72, 73] and cold-atom setups [74, 75, 76, 77]. However, the theoretical analysis of such quasi-periodic structures presents an intriguing challenge [30, 31, 68, 78, 61, 65, 67]. The traditional band theories, built on the foundation of periodicity, struggle to provide insight into the electronic properties of these systems. The lack of system-wide periodicity results in the collapse of the Brillouin zone, rendering conventional band predictions ineffective. In light of these complexities, the comprehending the properties of quasi-periodic 2D material systems demands the evolution of theoretical frameworks.

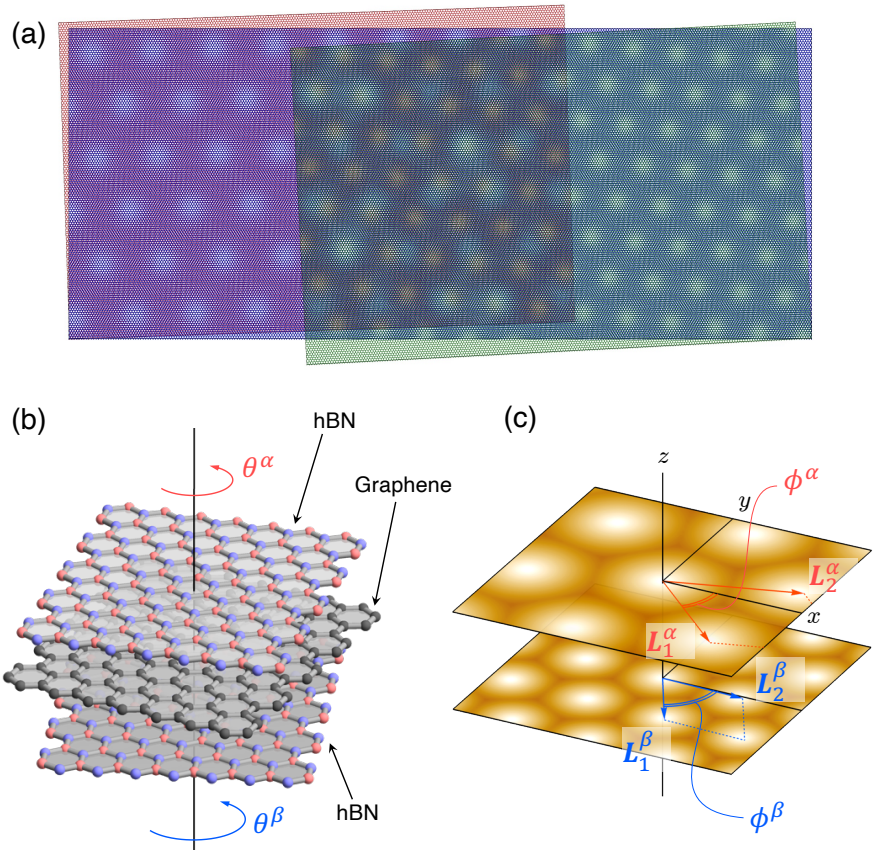

Figure 1.6: (a) Incommensurate moiré structure in trilayer system. (b) The atomic model of hBN/graphene/hBN trilayer system. Top and bottom hBN layers are stacked with twist angles θ^α and θ^β from middle graphene layer. (c) Top and bottom moiré patterns. The moiré superlattice vector is depending on the twist angle, and the moiré angle ϕ increases as the twist angle increases.

1.4 1D Quasi-crystalline and Hofstadter's butterfly

As mentioned above, trilayer moiré systems generally exhibit a quasi-periodic dual-moiré structure with no overall periodicity [79, 80, 81, 82, 83, 84, 85, 86]. In one-dimension (1D), a similar issue of dual period has long been studied as a fundamental problem, and and it holds significant implications when considering the two-dimensional quasi-periodic moiré systems discussed in this thesis. In this subsection, we will provide a brief overview of the 1D double-period problem [87, 74, 88, 89, 90, 91, 71, 92, 93, 94, 95, 96].

Let us consider the simplest one-dimensional periodic system as shown in Fig. 1.7, which is a 1D tight-binding lattice with lattice constant a, under a periodic potential of period λ. The periodic potential at site i is explicitly expressed as $V_i = V\cos(2\pi\alpha i + \delta)$, where $\alpha = \lambda/a$ and δ is a phase factor. When α, or the ratio of the periodic potential to the lattice constant is irrational, the two periodicities become incommensurate, and the overall system is quasi-periodic.

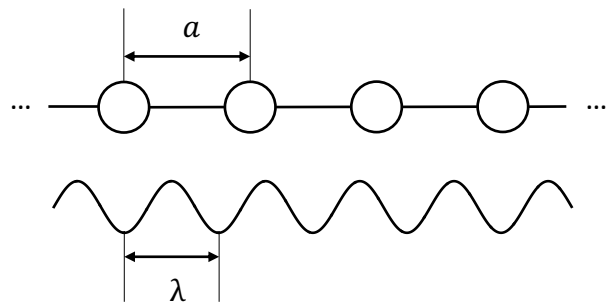

Figure 1.7: An image of one-dimensional double periodicity problem with lattice spaceing a and periodic potential with period λ.

We define the reciprocal vectors corresponding to the individual periods as $G_1 = 2\pi/a$ and $G_2 = 2\pi/\lambda$. In a single-period system, band gaps occur at positions corresponding to integer multiples of the only reciprocal vectors G, i.e.,

the electron density below the gap is quantized as $n_e = mG/(2\pi)$ (m:integer) as shown in 1.8(b) and (c). In a doubly-periodic system, similarly, energy gaps occurs at the electron density of $n_e = (m_1G_1 + m_2G_2)/(2\pi)$, where m_1, m_2 are integers. When this ratio $\alpha = \lambda/a$ is varied, the spectrum reveals a fractal-like spectrum known as Hofstadter's butterfly as shown in Fig. 1.9 [87]. There, each single energy gap is labelled by integers m_1 and m_2.

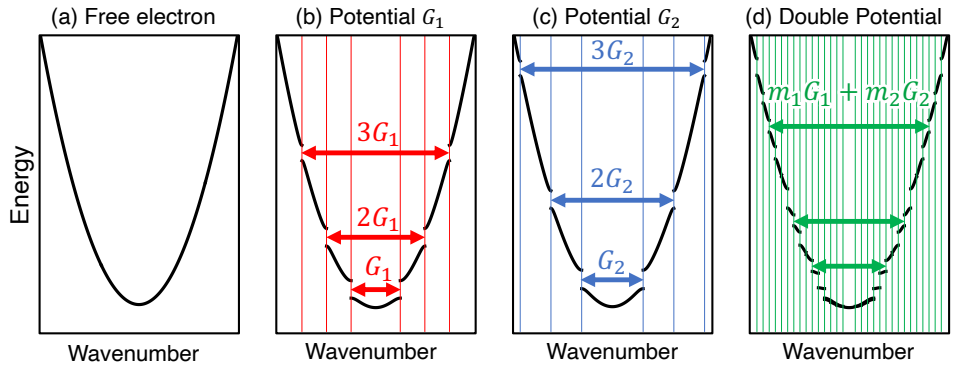

Figure 1.8: From left to right: (a) Free electrons, (b) Solely possessing a periodic potential with a period of a_1, (c) Similarly, with only a period of a_2, and (d) When both periods are simultaneously considered.

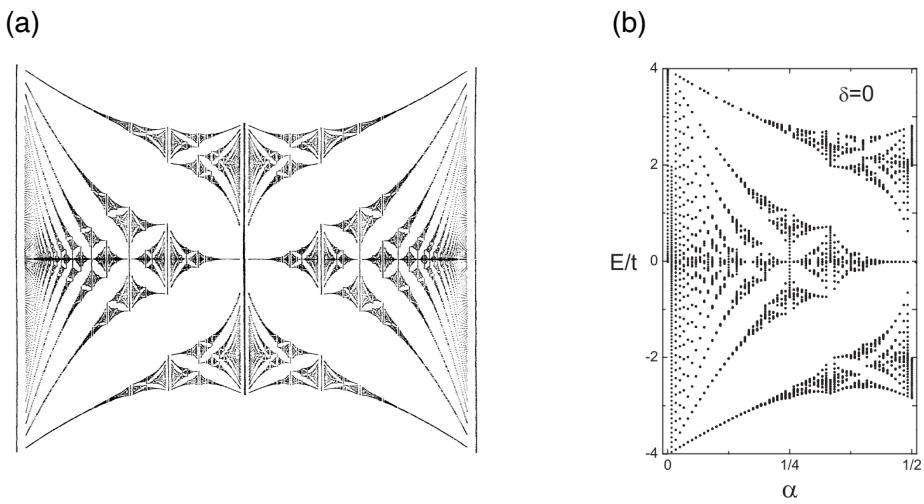

Figure 1.9: (a) Hofstadter's butterfly calculated by original problem [60]. (b) The similar plot of (a) calculated by one-dimensional double periodicities problem [87].

Importantly, this doubly-periodic 1D system can be entirely correlated with

a two-dimensional lattice with a perpendicular magnetic field. Let us consider a two-dimensional tight-binding square lattice with period a subjected to a perpendicular magnetic field $\boldsymbol{B}$. Let $\phi = Ba^2/(h/e)$ be the number of magnetic flux quanta penetrating a unit cell. It can be shown that the tight-binding Schrödinger equation of the 2D system can be reduced to a 1D tight-binding equation with a periodic potential $-2t_y \cos(2\pi\phi i + k_y)$. By substituting $\alpha \to \phi$ and $\delta \to -k_y$, a complete correspondence can be established with the one-dimensional bilayer periodic system. Therefore the energy spectrum of the 2D system also becomes a Hofstadter butterfly of Fig. 1.9.

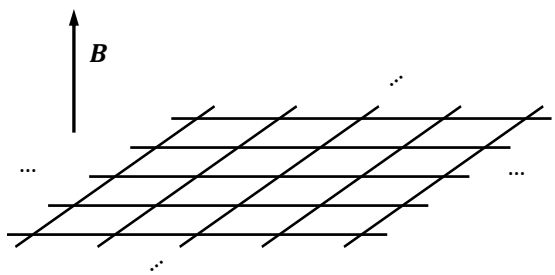

Figure 1.10: An image of the Hofstadter's problem as a two-dimensional square lattice in vertical magnetic field.

When the Fermi energy lies in an any of the fractal gaps, the Hall conductivity is integer-quantized as $\sigma_{xy} = \sum_n C_n(-e^2/h)$ where C_n is the first Chern number (integer) for the n-th band, defined by [97, 98, 88, 84]

$$C_n = \frac{1}{2\pi} \int_{BZ} d^2\boldsymbol{k} \left(\frac{\partial \mathcal{A}_{n,y}}{\partial k_x} - \frac{\partial \mathcal{A}_{n,x}}{\partial k_y} \right), \tag{1.1}$$

Here $\mathcal{A}_n(\boldsymbol{k}) = i\langle n, \boldsymbol{k}|\partial_{\boldsymbol{k}}|n, \boldsymbol{k}\rangle$ is the Berry connection and $|n, \boldsymbol{k}\rangle$ is the eigenstate of the n-th band at the Bloch wave number $\mathbf{k}$. This quantity remains constant during any continuous deformations that do not close the band gap. Interestingly, there exists a mathematical proof establishing the equivalence between the integer m_2 in the earlier expression $n_e = (m_1G_1+m_2G_2)/(2\pi)$ and the first Chern number C_n.

In this manner, the one-dimensional double-periodic structure can be mapped onto the problem of a two-dimensional lattice in a magnetic field, via the correspondence between the first Chern number and the integer quantizing electron density. In this thesis, we address the doubly-periodic problem in two-dimensions by examining twisted trilayer systems featuring two independent moiré patterns. We will show that the energy gaps are labeled a set of integers in a similar manner to the Hofstadter butterfly. Furthermore, these individual integers can be written as second Chern numbers, which quantizes the electro-magnetic response in the four-dimensional system. This is parallel to a 1D system, where the gap-labeling integer is written as a first Chern number, which corresponds to the 2D quantum Hall effect.

Chapter 2

Theoretical Backgrounds

This chapter explains how to formulate effective continuum models for the lattice-mismatched bilayer system exemplified by twisted bilayer graphene (TBG) and graphene-hexagonal boron nitride (G-hBN) bilayer. We begin by establishing the tight-binding Hamiltonian for the monolayer graphene and then present a general formula of the effective continuum model for dual atomic lattices. Subsequently, we apply this general form to specific examples, TBG and G-hBN bilayers.

2.1 Electronic Properties of Graphene Layer(s)

In this section, we derive the Hamiltonian of graphene based on the tight-binding model [99] and present the characteristic band structure. Graphene includes four valence electrons, with three of them forming covalent bonds within a honeycomb lattice. The remaining electron arises from the $2p_z$ orbital and behaves as itinerant electron. This itinerant electron exhibits characteristics resembling a massless Dirac fermion [2, 3], which consequently gives rise to the distinctive electronic state of graphene.

This itinerant electron in the graphene is well-described by the tight-binding model of p_z orbital on a honeycomb lattice as illustrated in Fig. 2.1(a). The

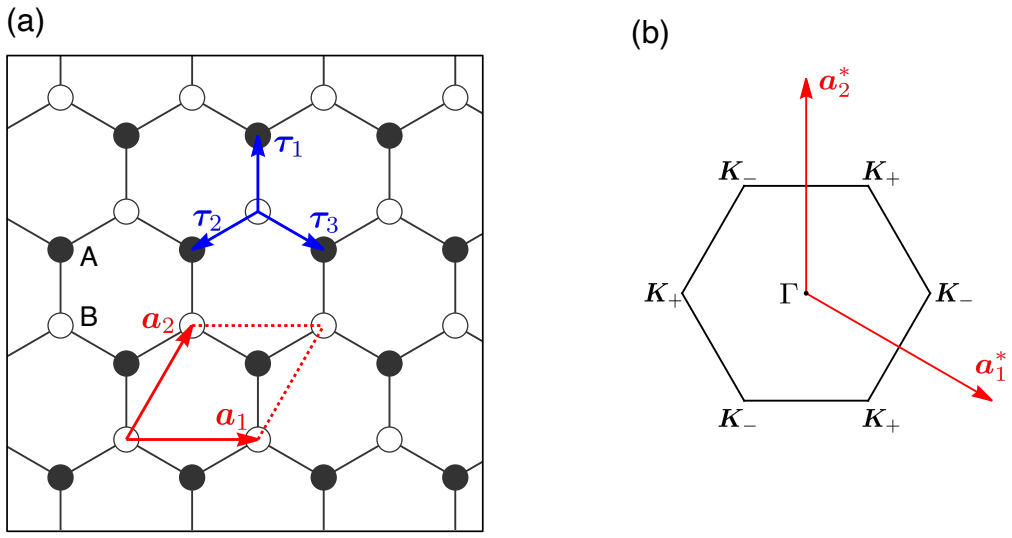

Figure 2.1: (a) The lattice structure of graphene and (b) the Brillouin zone of graphene.

lattice vectors are defined as

$$\boldsymbol{a}_1 = a\,(1,0)\,, \qquad \boldsymbol{a}_2 = a\left(\frac{1}{2}, \frac{\sqrt{3}}{2}\right), \tag{2.1}$$

where $a \approx 0.246$ nm represents the lattice constant of graphene [see Fig. 2.1(a)]. The honeycomb lattice has two sublattices named A and B sites, indicated by black and white dots in Fig. 2.1(a). In addition, three vectors define the relative positions of nearest-neighbor atoms:

$$\boldsymbol{\tau}_1 = a\left(0, \frac{1}{\sqrt{3}}\right), \quad \boldsymbol{\tau}_2 = a\left(-\frac{1}{2}, \frac{1}{2\sqrt{3}}\right), \quad \boldsymbol{\tau}_3 = a\left(\frac{1}{2}, \frac{1}{2\sqrt{3}}\right). \tag{2.2}$$

This enables us to express the positions $\boldsymbol{R}_A$ and $\boldsymbol{R}_B$ of the A and B sites as follows:

$$\begin{aligned} \boldsymbol{R}_A &= n_1\boldsymbol{a}_1 + n_2\boldsymbol{a}_2 \\ \boldsymbol{R}_B &= \boldsymbol{R}_A - \boldsymbol{\tau}_1, \end{aligned} \tag{2.3}$$

where n_1 and n_2 are integers.

For the honeycomb lattice, the first Brilloiuin zone (BZ) is spanned by the

reciprocal lattice vectors defined as:

$$\boldsymbol{a}_1^* = \frac{2\pi}{a}\left(1, \frac{1}{\sqrt{3}}\right), \qquad \boldsymbol{a}_2^* = \frac{2\pi}{a}\left(0, \frac{2}{\sqrt{3}}\right). \tag{2.4}$$

The corners of the BZ, $\boldsymbol{K}-$ and $\boldsymbol{K}+$ indicated in Fig. 2.1(b) are expressed as:

$$\boldsymbol{K}_- = \frac{2\pi}{a}\left(-\frac{2}{3}, 0\right), \qquad \boldsymbol{K}_+ = \frac{2\pi}{a}\left(\frac{2}{3}, 0\right). \tag{2.5}$$

Note that the relation between $\boldsymbol{K}_\pm$ and the $\boldsymbol{\tau}$ vectors is given by:

$$\begin{aligned} &\sum_{l=1}^{3} e^{i\boldsymbol{K}_\pm\cdot\boldsymbol{\tau}_l} = 0, \\ &\sum_{l=1}^{3} e^{i\boldsymbol{K}_\pm\cdot\boldsymbol{\tau}_l}\boldsymbol{\tau}_l = \frac{\sqrt{3}}{2}a(\pm i, 1). \end{aligned} \tag{2.6}$$

Using the basis of the atomic orbit located at position $\boldsymbol{R}$ as $|\boldsymbol{R}\rangle$, we can express the tight-binding wave function of the electron in graphene as:

$$|\psi(\boldsymbol{r})\rangle = \sum_{\boldsymbol{R}_A} c_A(\boldsymbol{R}_A)\,|\boldsymbol{R}_A\rangle + \sum_{\boldsymbol{R}_B} c_B(\boldsymbol{R}_B)\,|\boldsymbol{R}_B\rangle\,. \tag{2.7}$$

The Schrödinger equation for the wave function Eq. (2.7) is described by

$$H\sum_{\boldsymbol{R}_X} c_X(\boldsymbol{R}_X)\,|\boldsymbol{R}_X\rangle = E\sum_{\boldsymbol{R}_X} c_X(\boldsymbol{R}_X)\,|\boldsymbol{R}_X\rangle\,, \tag{2.8}$$

where $X = A, B$. The tight-binding Hamiltonian can be expressed as:

$$H = \sum_{\boldsymbol{R},\boldsymbol{R}'} |\boldsymbol{R}\rangle\,\langle\boldsymbol{R}|\,H\,|\boldsymbol{R}'\rangle\,\langle\boldsymbol{R}'|\,. \tag{2.9}$$

In this case, the positions of the nearest-neighbor atoms are described by Eq. (2.2). If we consider only nearest-neighbor hoppings as:

$$\langle\boldsymbol{R}_A|\,H\,|\boldsymbol{R}_B\rangle = -t, \quad (\boldsymbol{R}_A = \boldsymbol{R}_B + \boldsymbol{\tau}_l; \quad l = 1, 2, 3) \tag{2.10}$$

where t represents the transfer integral, the Hamiltonian for graphene can be expressed as:

$$H = -t\sum_{l=1}^{3}\sum_{\boldsymbol{R}_A=\boldsymbol{R}_B+\boldsymbol{\tau}_l} (|\boldsymbol{R}_A\rangle\,\langle\boldsymbol{R}_B| + |\boldsymbol{R}_B\rangle\,\langle\boldsymbol{R}_A|). \tag{2.11}$$

The Hamiltonian given in Eq. (2.11) and Schrd̈inger eqauation (2.8) lead to the following set of equations:

$$
\begin{aligned}
-t\sum_{l=1}^{3} c_B(\boldsymbol{R}_A-\boldsymbol{\tau}_l) &= Ec_A(\boldsymbol{R}_A)\\
-t\sum_{l=1}^{3} c_A(\boldsymbol{R}_B-\boldsymbol{\tau}_l) &= Ec_B(\boldsymbol{R}_B).
\end{aligned}
\tag{2.12}
$$

Applying Bloch theorem, we rewrite the wave function as:

$$
\begin{aligned}
c_A(\boldsymbol{R}_A) &= e^{i\boldsymbol{k}\cdot\boldsymbol{R}_A} f_A\\
c_B(\boldsymbol{R}_B) &= e^{i\boldsymbol{k}\cdot\boldsymbol{R}_B} f_B.
\end{aligned}
\tag{2.13}
$$

By substituting Eq (2.13) into Eq. (2.12), we obtain the eigenvalue equation in the momentum space,

$$
\begin{pmatrix} 0 & h(\boldsymbol{k}) \\ h(\boldsymbol{k})^* & 0 \end{pmatrix}
\begin{pmatrix} f_A \\ f_B \end{pmatrix}
= E
\begin{pmatrix} f_A \\ f_B \end{pmatrix},
\tag{2.14}
$$

where $h(\boldsymbol{k})$ is given by

$$
h(\boldsymbol{k}) = -t\sum_{l=1}^{3} e^{-i\boldsymbol{k}\cdot\boldsymbol{\tau}_l}.
\tag{2.15}
$$

The eigenenergy E is obtained by diagonalizing Eq. (2.14) as

$$
E_\pm(\boldsymbol{k}) = \pm|h(\boldsymbol{k})|.
\tag{2.16}
$$

Taking the origin of $\boldsymbol{k}$ at $\boldsymbol{K}_\pm$ and expanding $h(\boldsymbol{k}+K_\pm)$ up to liner in $\boldsymbol{k}$, we have

$$
h(\boldsymbol{K}_\pm+\boldsymbol{k}) \approx -t\sum_{l=1}^{3} e^{-i\boldsymbol{K}_\pm\cdot\boldsymbol{\tau}_l}(1-i\boldsymbol{k}\cdot\boldsymbol{\tau}_l) = \hbar v(\pm k_x + ik_y),
\tag{2.17}
$$

where we use Eq. (2.6) and define the velocity

$$
v = \frac{\sqrt{3}}{2}\frac{at}{\hbar}
\tag{2.18}
$$

Therefore, the effective Hamiltonian of graphene leads to

$$
H_{\mathrm{G}}(\boldsymbol{k}) = v(\pm\sigma_x k_x + \sigma_y k_y).
\tag{2.19}
$$

by using Pauli matrices σ_x and σ_y acting on the basis of A and B sites. Clearly the eigen energy is approximated as

$$E_{\pm}(\boldsymbol{K}_{+} + \boldsymbol{k}) = E_{\pm}(\boldsymbol{K}_{-} + \boldsymbol{k}) \approx \pm\hbar v k, \tag{2.20}$$

Remarkably, this indicate that graphene exhibits a linear dispersion relation with its crossing point located at $\boldsymbol{K}_{\pm}$, known as the Dirac cone and v corresponds to its band velocity.

2.2 Interlayer coupling between lattice mismatched layers

To formulate the effective continuum model of lattice mismatched bilayers, which is a main target of the present study, we introduce their interlayer coupling. We define a pair of the lattice vectors $\boldsymbol{a}_1$ and $\boldsymbol{a}_2$ for layer 1, and another pair $\tilde{\boldsymbol{a}}_1$ and $\tilde{\boldsymbol{a}}_2$ for layer 2. The reciprocal lattice vectors $\boldsymbol{G}_i$ and $\tilde{\boldsymbol{G}}_i$ are defined for layers 1 and 2 by $\boldsymbol{a}_i \cdot \boldsymbol{G}_j, = \tilde{\boldsymbol{a}}_i \cdot \tilde{\boldsymbol{G}}_j = 2\pi\delta_{ij}$. The unit cell areas are denoted by $S = |\boldsymbol{a}_1 \times \boldsymbol{a}_2|$ and $\tilde{S} = |\tilde{\boldsymbol{a}}_1 \times \tilde{\boldsymbol{a}}_2|$. Due to the generalized Umklapp process [100], electron coupling occurs only under the condition:

$$\boldsymbol{k} + \boldsymbol{G} = \tilde{\boldsymbol{k}} + \tilde{\boldsymbol{G}}, \tag{2.21}$$

where $\boldsymbol{G} = m_1\boldsymbol{G}_1 + m_2\boldsymbol{G}_2$ and $\tilde{\boldsymbol{G}} = \tilde{m}_1\tilde{\boldsymbol{G}}_1 + \tilde{m}_2\tilde{\boldsymbol{G}}_2$. This implies that the Bloch state $\phi^{(1)}_{\boldsymbol{k}}$ of layer 1 can be expressed as a summation of $e^{i(\boldsymbol{k}+\boldsymbol{G})}$ over reciprocal lattice vectors $\boldsymbol{G}$, and the Bloch state $\phi^{(2)}_{\tilde{\boldsymbol{k}}}$ of layer 2 can be expressed as a summation of $e^{i(\tilde{\boldsymbol{k}}+\tilde{\boldsymbol{G}})}$ over reciprocal lattice vectors $\tilde{\boldsymbol{G}}$. The Hamiltonian of the entire system can be constructed using the Fourier components of $\boldsymbol{G}$ and $\tilde{\boldsymbol{G}}$. Consequently, the matrix elements $\langle\phi^{(2)}_{\tilde{\boldsymbol{k}}}|\, H\, |\phi^{(1)}_{\boldsymbol{k}}\rangle$ exist only under the conditions specified in Eq. (2.21).

The positions of the atoms can be expressed as follows, where $X = A, B$ and

$\tilde{X} = \tilde{A}, \tilde{B}$:

$$\boldsymbol{R}_X = n_1\boldsymbol{a}_1 + n_2\boldsymbol{a}_2 + \boldsymbol{\tau}_X$$
$$\boldsymbol{R}_{\tilde{X}} = \tilde{n_1}\tilde{\boldsymbol{a}}_1 + \tilde{n_2}\tilde{\boldsymbol{a}}_2 + \boldsymbol{\tau}_{\tilde{X}}. \tag{2.22}$$

Here, n_i and $\tilde{n_i}$ are integers, and $\boldsymbol{\tau}_X$ and $\boldsymbol{\tau}_{\tilde{X}}$ represent the positions of the sublattices within the unit cells. When we set the interlayer distance to d, we can express $\boldsymbol{\tau}_X \cdot \boldsymbol{e}_z = 0$ and $\boldsymbol{\tau}_{\tilde{X}} \cdot \boldsymbol{e}_z = d$. We define the atomic state of sublattice X at the $\boldsymbol{R}_X$ as $|\boldsymbol{R}_X\rangle \equiv \phi_X(\boldsymbol{r} - \boldsymbol{R}_X)$ and we assume the transfer integral from $\boldsymbol{R}_X$ to $\boldsymbol{R}_{\tilde{X}}$ as $-T_{\tilde{X}X}(\boldsymbol{R}_{\tilde{X}} - \boldsymbol{R}_X)$. Consequently, the interlayer Hamiltonian can be written as:

$$U = -\sum_{X,\tilde{X}} T_{\tilde{X}X}(\boldsymbol{R}_{\tilde{X}} - \boldsymbol{R}_X)\,|\boldsymbol{R}_{\tilde{X}}\rangle\,\langle\boldsymbol{R}_X| + h.c. \tag{2.23}$$

In cases where the period of the moiré superlattice is significantly larger, and a larger number of lattice points are included in the unit cell of the entire system, the Hamiltonian in the real basis becomes excessively complex since every pair of lattice points from layers 1 and 2 is required. On the other hand, the interlayer interaction can be clearly expressed in momentum space. We define the Bloch basis as follows:

$$|\boldsymbol{k}, X\rangle = \frac{1}{\sqrt{N}}\sum_{\boldsymbol{R}_X} e^{i\boldsymbol{k}\cdot\boldsymbol{R}_X}\,|\boldsymbol{R}_X\rangle$$
$$|\tilde{\boldsymbol{k}}, \tilde{X}\rangle = \frac{1}{\sqrt{\tilde{N}}}\sum_{\boldsymbol{R}_{\tilde{X}}} e^{i\tilde{\boldsymbol{k}}\cdot\boldsymbol{R}_{\tilde{X}}}\,|\boldsymbol{R}_{\tilde{X}}\rangle\,. \tag{2.24}$$

Here, $\boldsymbol{k}$ and $\tilde{\boldsymbol{k}}$ are two-dimensional Bloch vectors, and N and $\tilde{N}$ are the numbers of atoms in the area of the whole system S_{tot}.

In general, when layers 1 and 2 are incommensurate, we assume the existence of a finite area $S_{\text{tot}} = NS = \tilde{N}\tilde{S}$, and normalize the wavefunctions accordingly. By substituting Eq. (2.24) into Eq. (2.23), we obtain the matrix elements of interlayer interaction in the Bloch basis as follows:

$$U_{\tilde{X}X}(\tilde{\boldsymbol{k}}, \boldsymbol{k}) \equiv \langle\tilde{\boldsymbol{k}}, \tilde{X}|\,U\,|\boldsymbol{k}, X\rangle$$
$$= -\sum_{\boldsymbol{G},\tilde{\boldsymbol{G}}} t_{\tilde{X}X}(\boldsymbol{k}+\boldsymbol{G})e^{-i\boldsymbol{G}\cdot\boldsymbol{\tau}_X + i\tilde{\boldsymbol{G}}\cdot\boldsymbol{\tau}_{\tilde{X}}}\delta_{\boldsymbol{k}+\boldsymbol{G},\tilde{\boldsymbol{k}}+\tilde{\boldsymbol{G}}} \tag{2.25}$$

These elements are non-zero only in Eq. (2.21). Here, we define the Fourier transform of the transfer integral $t(\boldsymbol{q})$ as:

$$t_{\tilde{X}X}(\boldsymbol{q}) = \frac{1}{\sqrt{S\tilde{S}}} \int T_{\tilde{X}X}(\boldsymbol{r} + z_{\tilde{X}X}\boldsymbol{e}_z) e^{-i\boldsymbol{q}\cdot\boldsymbol{r}} d^2r. \tag{2.26}$$

Here, $z_{\tilde{X}X}\boldsymbol{e}_z = (\boldsymbol{\tau}_{\tilde{X}} - \boldsymbol{\tau}_X) \cdot \boldsymbol{e}_z$, and the integral is taken over the entire plane on which $\boldsymbol{r}$ can vary. The quantity $t_{\tilde{X}X}(\boldsymbol{q})$ rapidly diminishes for large $\boldsymbol{q}$, so we need not calculate the large summation in Eq. (2.25).

2.3 Twisted bilayer graphene

We consider twisted bilayer graphene (TBG), where one graphene layer is stacked upon another graphene layer with a twisted angle θ and interlayer distance d. We define the lattice vectors a_1 and a_2 in layer 1 as shown in Eq. (2.1), while the lattice vectors of layer 2 can be expressed as $\tilde{a}_i = Ra$, where R is a rotation matrix with an angle of θ. The reciprocal lattice vectors $\boldsymbol{G}_1$ and $\boldsymbol{G}_2$ in layer 1 are defined as given in Eq. (2.4), while the reciprocal lattice vectors in layer 2 are defined as $\tilde{\boldsymbol{G}}_i = R\boldsymbol{G}_i$. The atomic positions are described as follows:

$$\begin{aligned} \boldsymbol{R}_X &= n_1\boldsymbol{a}_1 + n_2\boldsymbol{a}_2 + \boldsymbol{\tau}_X \\ \boldsymbol{R}_{\tilde{X}} &= \tilde{n_1}\tilde{\boldsymbol{a}}_1 + \tilde{n_2}\tilde{\boldsymbol{a}}_2 + \boldsymbol{\tau}_{\tilde{X}}. \end{aligned} \tag{2.27}$$

Here, $X = A, B$ corresponds to atoms in layer 1, while $\tilde{X} = \tilde{A}, \tilde{B}$ refers to atoms in layer 2. The specific expressions for the position vectors are as follows:

$$\begin{aligned} \boldsymbol{\tau}_A &= 0 \\ \boldsymbol{\tau}_B &= (\boldsymbol{a}_1 - 2\boldsymbol{a}_2)/3 \\ \boldsymbol{\tau}_{\tilde{A}} &= d\boldsymbol{e}_z + \boldsymbol{\tau}_0 \\ \boldsymbol{\tau}_{\tilde{B}} &= d\boldsymbol{e}_z + \boldsymbol{\tau}_0 + (\boldsymbol{a}_1 - 2\boldsymbol{a}_2)/3. \end{aligned} \tag{2.28}$$

In this context, we have defined the origin to be at the position of atom A, and $\boldsymbol{\tau}_0$ represents the intralayer vector denoting the relative positional transformation within layer 2.

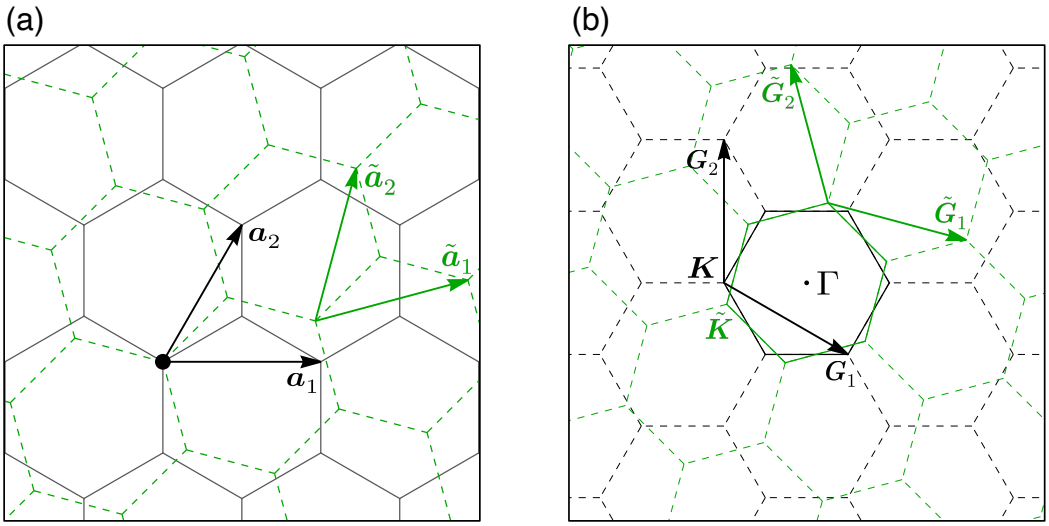

Figure 2.2: (a) The lattice vectors in $\theta = 15°$ and (b) Brillouin zone in $\theta = 15°$.

In order to describe the dynamics of electrons, we adopt a one-orbital tight-binding model for the p_z orbitals of the atoms. Consequently, the interlayer transfer integral $T_{X\tilde{X}}(\boldsymbol{R})$ becomes independent of the labels X and $\tilde{X}$ and can be approximated using the Slater-Koster parameters [101]. It can be expressed as:

$$-T(\boldsymbol{R}) = V_{pp\pi}\left[1 - \left(\frac{\boldsymbol{R}\cdot\boldsymbol{e}_z}{R}\right)^2\right] + V_{pp\sigma}\left(\frac{\boldsymbol{R}\cdot\boldsymbol{e}_z}{R}\right)^2$$
$$V_{pp\pi} = V^0_{pp\pi}e^{-(R-a/\sqrt{3})/r_0}, \quad V_{pp\sigma} = V^0_{pp\sigma}e^{-(R-d)/r_0}. \tag{2.29}$$

Here, $a \simeq 0.246[\mathrm{nm}], d \simeq 0.335[\mathrm{nm}], V^0_{pp\pi} \simeq -2.7[\mathrm{eV}], V^0_{pp\sigma} \simeq 0.48[\mathrm{eV}], \mathrm{and} r_0 \simeq 0.184a$ represent the graphene's parameters. These expressions determine the amplitude of the coupling, denoted as $t(\boldsymbol{K}+\boldsymbol{G})$, which relies on the distance from the origin in k-space. From the given parameters, we have the following values: $t(K) \simeq 100[\mathrm{meV}], t(2K) \simeq 1.6[\mathrm{meV}], t(\sqrt{7}K) \simeq 0.062[\mathrm{meV}]$, where $K = |\boldsymbol{K}| = 4\pi/3a$.

When the difference between the lattice vectors of the layer 1 and layer 2 is small, i.e., when the rotation angle θ is small, the interference of these lattice structures gives rise to long-period moíre structures. In this case, the rotation

matrix R approaches the unitary matrix. The reciprocal lattice vector of the moiré superlattice is given by

When the disparity between the lattice vectors of layer 1 and layer 2 is minimal, specifically when the rotation angle θ is small, the combination of these lattice structures gives rise to intricate moiré patterns with long periodicity. In such instances, the rotation matrix R approximates the identity matrix. The reciprocal lattice vector of the moiré superlattice is defined as:

$$\boldsymbol{G}_i^M = \boldsymbol{G}_i - \tilde{\boldsymbol{G}}_i = [1 - R]\,\boldsymbol{G}_i \tag{2.30}$$

The matrix elements pertaining to the interlayer hopping for the long-range waves can be expressed as follows:

$$\begin{aligned} &U_{\tilde{X}X}(\boldsymbol{k} + m_1\boldsymbol{G}_1^M + m_2\boldsymbol{G}_2^M, \boldsymbol{k}) \\ &\quad = t_{\tilde{X}X}(\boldsymbol{k} + m_1\boldsymbol{G}_1 + m_2\boldsymbol{G}_2)e^{-i(m_1\boldsymbol{G}_1+m_2\boldsymbol{G}_2)\cdot\boldsymbol{\tau}_X + i(m_1\tilde{\boldsymbol{G}}_1+m_2\tilde{\boldsymbol{G}}_2)\cdot\boldsymbol{\tau}_{\tilde{X}}}. \end{aligned} \tag{2.31}$$

Here, m_1 and m_2 represent integers. Since the low-energy spectrum of graphene

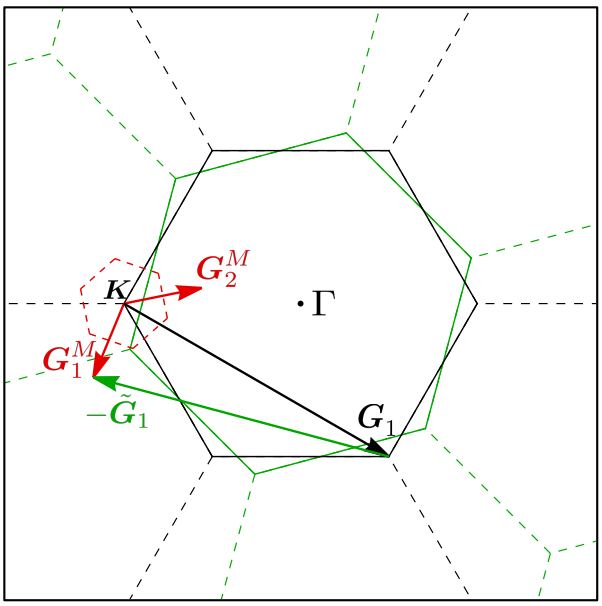

Figure 2.3: The moiré reciprocal lattice vectors in $\theta = 15°$. $\boldsymbol{G}_1^M$ is constructed by $\boldsymbol{G}_1 - \tilde{\boldsymbol{G}}_1$.

is dominated by the electronic states around the Brillouin Zone corner K and K'

points, we consider the matrix elements of the K vectors near these. K and K' points at each layer are at

$$\begin{aligned}\boldsymbol{K}_\xi &= -\xi(2\boldsymbol{G}_1 + \boldsymbol{G}_2)/3 \\ \tilde{\boldsymbol{K}}_\xi &= -\xi(2\tilde{\boldsymbol{G}}_1 + \tilde{\boldsymbol{G}}_2)/3\end{aligned} \tag{2.32}$$

where $\xi = \pm 1$ serve as the labels for K and K'. Presently, the electron $\boldsymbol{k} = \boldsymbol{K}_+$ located at $(\boldsymbol{K}_+)$ in layer 1 interacts with the electron at $\boldsymbol{K}_+ + m_1\boldsymbol{G}_1 + m_2\boldsymbol{G}_2$ in the layer 2, with a magnitude of $t(\boldsymbol{K}_+ + m_1\boldsymbol{G}_1 + m_2\boldsymbol{G}_2)$. Here, $t(K) \simeq 100[\text{meV}], t(2K) \simeq 1.6[\text{meV}], t(\sqrt{7}K) \simeq 0.062[\text{meV}]$ and other couplings from $\boldsymbol{K}$ points is negligibly small. When the vector $\boldsymbol{k}$ deviates slightly from $\boldsymbol{K}_+$, the matrix elements undergo alterations. However, for our purpose, we treat $\boldsymbol{k}$ as being in proximity to $\boldsymbol{K}_+$, disregarding this dependence. Based on the aforementioned considerations, we derive an interlayer Hamiltonian in the vicinity of $\boldsymbol{K}_+$.

$$\begin{aligned}U =& \begin{pmatrix} U_{\tilde{A}A} & U_{\tilde{A}B} \\ U_{\tilde{B}A} & U_{\tilde{B}B} \end{pmatrix} \\ =& t(K)\left[\begin{pmatrix} 1 & 1 \\ 1 & 1 \end{pmatrix} + \begin{pmatrix} 1 & \omega^{-\xi} \\ \omega^{\xi} & 1 \end{pmatrix} e^{i\xi\boldsymbol{G}_1^M\cdot\boldsymbol{r}} + \begin{pmatrix} 1 & \omega^{\xi} \\ \omega^{-\xi} & 1 \end{pmatrix} e^{i\xi(\boldsymbol{G}_1^M+\boldsymbol{G}_2^M)\cdot\boldsymbol{r}}\right] \\ &+ t(2K)\left[\begin{pmatrix} 1 & 1 \\ 1 & 1 \end{pmatrix} e^{i\xi(2\boldsymbol{G}_1^M+\boldsymbol{G}_2^M)\cdot\boldsymbol{r}} + \begin{pmatrix} 1 & \omega^{-\xi} \\ \omega^{\xi} & 1 \end{pmatrix} e^{i\xi\boldsymbol{G}_2^M\cdot\boldsymbol{r}} + \begin{pmatrix} 1 & \omega^{\xi} \\ \omega^{-\xi} & 1 \end{pmatrix} e^{-i\xi\boldsymbol{G}_2^M\cdot\boldsymbol{r}}\right] \\ &+ \cdots\end{aligned} \tag{2.33}$$

Here, $\boldsymbol{r}$ donates the intralayer position, $\omega = e^{2\pi i/3}$, $\boldsymbol{\tau}_0 = \boldsymbol{0}$. The Hamiltonian of entire system can be expressed in the basis $\{A, B, \tilde{A}, \tilde{B}\}$ as follows:

$$U_{\text{eff}}^{(\xi)} = \begin{pmatrix} H_1 & U^\dagger \\ U & H_2 \end{pmatrix}. \tag{2.34}$$

Where H_1, H_2 represent the intralayer Hamilotonian for layer 1 and layer 2, re-

spectively:

$$H_1 \simeq -\hbar v(\boldsymbol{k} - \boldsymbol{K}_\xi) \cdot (\xi\sigma_x, \sigma_y)$$
$$H_2 \simeq -\hbar v \left[R^{-1}(\boldsymbol{k} - \tilde{\boldsymbol{K}}_\xi)\right] \cdot (\xi\sigma_x, \sigma_y). \tag{2.35}$$

Here, we have employed the Pauli matrices $\boldsymbol{\sigma}_x, \boldsymbol{\sigma}_y$ and the band velocity of graphene, denoted by v.

2.4 Graphene/hBN heterostructure

Hexagonal boron nitride (hBN) exhibits a honeycomb lattice structure similar to graphene, where nitrogen atoms occupy the A sites and boron atoms occupy the B sites. The low energy electronic states of hBN is described by the tight binding model of p_z orbital of boron and nitrogen atoms, incorporating onsite potentials [102]

$$V_{\mathrm{B}} = 3.34[\mathrm{eV}], \qquad V_{\mathrm{N}} = -1.40[\mathrm{eV}]. \tag{2.36}$$

relative to those of graphene (where $V_{\mathrm{G}} = 0$). Importantly, the lattice constant of hBN ($a_{\mathrm{hBN}} \simeq 0.2504$ [nm]) differs from that of graphene ($a \simeq 0.246$ [nm]). For our analysis, we assume perfect flatness for both graphene and hBN, a constant interlayer distance $d_{\mathrm{G-hBN}} \simeq 0.322$[nm], and a twist angle θ between the two layers.

The lattice vectors of graphene are defined according to Eq. (2.1), while those of hBN are given by

$$\tilde{\boldsymbol{a}}_i = MR\boldsymbol{a}_i, \tag{2.37}$$

where R represents a rotation matrix with an angle θ, and M denotes isotropic expansion expressed by the identity matrix I. The difference in lattice constants, $1 + \varepsilon = a_{\mathrm{hBN}}/a \simeq 1.018$, is incorporated as $M = (1 + \varepsilon)I$. Reciprocal lattice vectors of graphene and hBN, denoted as $\boldsymbol{G}_i$ and $\tilde{\boldsymbol{G}}_i$ respectively, are defined by the condition $\boldsymbol{a}_i \cdot \boldsymbol{G}_j = \tilde{\boldsymbol{a}}_i \cdot \tilde{\boldsymbol{G}}_j = 2\pi\delta_{ij}$. When the twist angle is small, moiré

superlattice vectors can be defined as

$$\boldsymbol{G}_i^M = (I - M^{-1}R)\boldsymbol{G}_i \tag{2.38}$$

and the moiré period can be obtained as

$$L_M = \frac{2\pi}{|\boldsymbol{G}_i^M|} = \frac{1+\varepsilon}{\sqrt{\varepsilon^2 + 2(1+\varepsilon)(1-\cos\theta)}}a \tag{2.39}$$

which evaluates to $L_M \simeq 13.8$[nm] at $\theta = 0°$.

In the case of a sufficiently small twist angle θ that results in a moiré period significantly longer than the atomic scale, the low-energy electronic state can be described by effective continuum model. The Hamiltonian for the entire system is expressed as a 4×4 matrix:

$$H_{\mathrm{G-hBN}} = \begin{pmatrix} H_{\mathrm{G}} & U^\dagger \\ U & H_{\mathrm{hBN}} \end{pmatrix}, \tag{2.40}$$

where the basis consists of graphene's A and B sites, as well as hBN's $\tilde{\mathrm{A}}$ and $\tilde{\mathrm{B}}$ sites $\{A, B, \tilde{A}, \tilde{B}\}$. Here, H_{hBN} represents the Hamiltonian of the hBN monolayer. By neglecting kinetic terms and considering only onsite potentials, we obtain an approximate expression for the hBN Hamiltonian:

$$H_{\mathrm{hBN}} \simeq \begin{pmatrix} V_{\mathrm{B}} & 0 \\ 0 & V_{\mathrm{N}} \end{pmatrix}. \tag{2.41}$$

The interlayer coupling is obtained from the general form Eq. (2.25),

$$U = u_0 \left[\begin{pmatrix} 1 & 1 \\ 1 & 1 \end{pmatrix} + \begin{pmatrix} 1 & \omega^{-\xi} \\ \omega^{\xi} & 1 \end{pmatrix} e^{i\xi \boldsymbol{G}_1^M \cdot \boldsymbol{r}} + \begin{pmatrix} 1 & \omega^{\xi} \\ \omega^{-\xi} & 1 \end{pmatrix} e^{i\xi(\boldsymbol{G}_1^M + \boldsymbol{G}_2^M)\cdot \boldsymbol{r}} \right] \tag{2.42}$$

where $\boldsymbol{G}_i^M$ represents the moiré reciprocal lattice vectors of graphene/hBN and $u_0 = t(K) \simeq 150$[meV]. Since the hBN states are energetically far from the low energy spectrum of graphene, these effect is incorporated by the second-order perturbation,

$$\begin{aligned} H_{\mathrm{G-hBN}}^{(red)} &= H_{\mathrm{G}} + U^\dagger(-H_{\mathrm{hBN}})^{-1}U \\ &\equiv H_{\mathrm{G}} + V_{\mathrm{hBN}} \end{aligned} \tag{2.43}$$

Here, the term V_{hBN} can be expressed as:

$$\begin{aligned} V_{\mathrm{hBN}} &\equiv U^{\dagger}(-H_{\mathrm{hBN}})^{-1}U \\ &= V_0 \begin{pmatrix} 1 & 0 \\ 0 & 1 \end{pmatrix} + \Bigg\{ V_1 e^{i\xi\psi} \Bigg[\begin{pmatrix} 1 & \omega^{-\xi} \\ 1 & \omega^{-\xi} \end{pmatrix} e^{i\xi \boldsymbol{G}_1^M \cdot \boldsymbol{r}} \\ &\quad + \begin{pmatrix} 1 & \omega^{\xi} \\ \omega^{\xi} & \omega^{-\xi} \end{pmatrix} e^{i\xi \boldsymbol{G}_2^M \cdot \boldsymbol{r}} + \begin{pmatrix} 1 & 1 \\ \omega^{-\xi} & \omega^{-\xi} \end{pmatrix} e^{i\xi \boldsymbol{G}_3^M \cdot \boldsymbol{r}} \Bigg] + \mathrm{h.c.} \Bigg\}, \end{aligned} \tag{2.44}$$

where

$$\begin{aligned} V_0 &= -3u_0^2 \left(\frac{1}{V_{\mathrm{N}}} + \frac{1}{V_{\mathrm{B}}} \right), \qquad V_1 e^{i\psi} = -u_0^2 \left(\frac{1}{V_{\mathrm{N}}} + \omega \frac{1}{V_{\mathrm{B}}} \right), \\ \boldsymbol{G}_3^M &= -\boldsymbol{G}_1^M - \boldsymbol{G}_2^M. \end{aligned} \tag{2.45}$$

Chapter 3

hBN/Graphene/hBN

In order to compute the trilayer system characterized by a double moiré structure, we employed a commensurate approximation. Typically, the periods of the double moiré pattern are incommensurate; however, numerous nearly commensurate points exist where the two moiré patterns closely approach each other. We treated these points as the exact periods of the trilayer system, thereby yielding the Hamiltonian in a finite-dimensional space.

Within this chapter, we elucidate the methodology for acquiring the commensurate approximants and corresponding Hamiltonians. Subsequently, we present the outcomes of numerical computations, revealing a fractal energy gap behavior. We then explore the principles governing these fractal energy gaps and deduce six characteristic integers by leveraging six unit volumes, accounting for the periodicity redundancies. Lastly, we engage in a discourse pertaining to one of the interpretations of these six integers, specifically related to quasi-Brillouin zones.

3.1 Commensurate approximation

We consider a trilayer system composed of hBN/graphene/hBN, where the top hBN layer (indexed by $\lambda = \alpha$) has a twist angle of θ^α, and the bottom hBN layer (indexed by $\lambda = \beta$) has a twist angle of θ^β. Graphene and hBN share

a honeycomb structure with slightly different lattice constants: approximately $a \approx 0.246\,\mathrm{nm}$ for graphene and $a_{\mathrm{hBN}} \approx 0.2504\,\mathrm{nm}$ for hBN [103]. In our notation, A and B represent the sublattices of graphene, while θ^α and θ^β represent the nitrogen and boron sites of the λ-th hBN layer, respectively. The geometry is defined such that $\theta^\lambda = 0$ corresponds to the alignment of the AB bond and the $A^\lambda B^\lambda$ bond, which are parallel to each other. The lattice vectors of graphene are denoted as $\boldsymbol{a}_1 = a(1,0)$ and $\boldsymbol{a}_2 = a(1/2, \sqrt{3}/2)$, while those of the λ-th hBN layer are given by [47, 100]

$$\boldsymbol{a}_i^\lambda = MR(\theta^\lambda)\,\boldsymbol{a}_i \quad (i = 1, 2), \tag{3.1}$$

where $R(\theta^\lambda)$ represents a two-dimensional rotation matrix with an angle θ^λ, and $M = (1+\varepsilon)\mathbf{1}$ corresponds to an isotropic expansion factor of $1 + \varepsilon = a_{\mathrm{hBN}}/a \approx 1.018$. In the following discussion, we assume that the twist angles θ^α and θ^β are sufficiently small (a few degrees or less) so that the moiré superperiod greatly exceeds the atomic lattice constant a. The primitive lattice vectors of the moiré superlattice for the λ-th layer are defined as

$$\boldsymbol{L}_i^\lambda = [\mathbf{1} - R(\theta^\lambda)^{-1} M^{-1}]^{-1} \boldsymbol{a}_i \quad (i = 1, 2). \tag{3.2}$$

and the corresponding reciprocal lattice vectors are given by

$$\boldsymbol{G}_i^\lambda = [\mathbf{1} - M^{-1} R(\theta^\lambda)] \boldsymbol{a}_i^* \quad (i = 1, 2), \tag{3.3}$$

where $\boldsymbol{a}_i^*$ represents the reciprocal lattice vectors for graphene, satisfying $\boldsymbol{a}_i \cdot \boldsymbol{a}_j^* = 2\pi\delta_{ij}$. The moiré superlattice period is determined by

$$|\boldsymbol{L}_1^\lambda| = |\boldsymbol{L}_2^\lambda| = \frac{1+\varepsilon}{\sqrt{\varepsilon^2 + 2(1+\varepsilon)(1-\cos\theta^\lambda)}}\, a \tag{3.4}$$

where ε is the expansion factor.

The moiré rotation angle, denoted as the relative angle between $\boldsymbol{L}_i^\lambda$ and $\boldsymbol{a}_i$, is expressed as

$$\phi^\lambda = \arctan\left(\frac{-\sin\theta^\lambda}{1+\varepsilon-\cos\theta^\lambda}\right). \tag{3.5}$$

Fig. 3.1 presents the plots of (a) the moiré superlattice period L and (b) the moiré rotation angle ϕ as functions of the twist angle θ. The super period L exhibits a

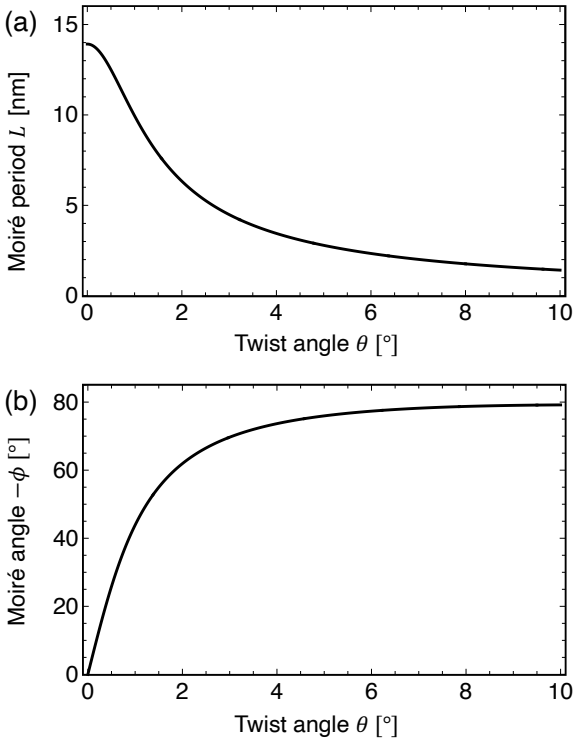

Figure 3.1: (a) Moiré period L [Eq. (3.4)] and (b) the moiré rotation angle ϕ [Eq. (3.5)] as functions of the twist angle θ

value of 13.8 nm at $\theta = 0°$, decreasing with increasing θ. The rotation angle ϕ is zero at $\theta = 0°$ and rapidly increases in the negative direction as θ increases. For simplicity, the subscripts are redefined as follows:

$$(\boldsymbol{G}_1, \boldsymbol{G}_2, \boldsymbol{G}_3, \boldsymbol{G}_4) = (\boldsymbol{G}_1^\alpha, \boldsymbol{G}_2^\alpha, \boldsymbol{G}_1^\beta, \boldsymbol{G}_2^\beta). \tag{3.6}$$

In general, the two moiré superlattices are incommensurate, indicating the absence of a unit cell in the trilayer system as a whole. However, for any pair of twist angles (θ^α, θ^β), there exist lattice points from the two moiré patterns that happen to be in close proximity to each other. This situation can be expressed as

$$p_1\boldsymbol{L}_1^\alpha + p_2\boldsymbol{L}_2^\alpha = p_3\boldsymbol{L}_1^\beta + p_4\boldsymbol{L}_2^\beta + \Delta\boldsymbol{L}, \tag{3.7}$$

where p_i (for $i = 1, 2, 3, 4$) are integers, and $\Delta\boldsymbol{L}$ represents the difference.

When $\Delta\boldsymbol{L}$ is significantly smaller than the moiré periods, the electronic structure of the incommensurate system can be approximated by an exactly commen-

surate system, neglecting $\Delta\boldsymbol{L}$. This approximation is achieved by making slight deformations (rotations, expansions, or contractions) to the moiré patterns, causing $\Delta\boldsymbol{L}$ to vanish.

Fig. 3.2(a) illustrates an actual example of commensurate approximant for $(\theta^\alpha, \theta^\beta) = (0, 1.1908°)$, where $(p_1, p_2, p_3, p_4) = (1, 1, -1, 2)$ and $(q_1, q_2, q_3, q_4) = (-1, 3, -3, 2)$. A commensurate approximant can be defined by selecting two nearly commensurate points with integers (p_1, p_2, p_3, p_4) and (q_1, q_2, q_3, q_4). These two points become the exact primitive lattice vectors of the commensurate approximant:

$$\begin{aligned}\begin{pmatrix} \boldsymbol{L}_1^{\mathrm{c}} \\ \boldsymbol{L}_2^{\mathrm{c}} \end{pmatrix} &= \begin{pmatrix} p_1 & p_2 \\ q_1 & q_2 \end{pmatrix} \begin{pmatrix} \boldsymbol{L}_1^{\alpha} \\ \boldsymbol{L}_2^{\alpha} \end{pmatrix} \\ &= \begin{pmatrix} p_3 & p_4 \\ q_3 & q_4 \end{pmatrix} \begin{pmatrix} \boldsymbol{L}_1^{\beta} \\ \boldsymbol{L}_2^{\beta} \end{pmatrix}. \end{aligned} \tag{3.8}$$

Correspondingly, the reciprocal superlattice vectors $\boldsymbol{G}_1^{\mathrm{c}}$ and $\boldsymbol{G}_2^{\mathrm{c}}$ are given by:

$$\begin{aligned}\begin{pmatrix} \boldsymbol{G}_1^{\mathrm{c}} \\ \boldsymbol{G}_2^{\mathrm{c}} \end{pmatrix} &= \left[\begin{pmatrix} p_1 & p_2 \\ q_1 & q_2 \end{pmatrix}^T \right]^{-1} \begin{pmatrix} \boldsymbol{G}_1^{\alpha} \\ \boldsymbol{G}_2^{\alpha} \end{pmatrix} \\ &= \left[\begin{pmatrix} p_3 & p_4 \\ q_3 & q_4 \end{pmatrix}^T \right]^{-1} \begin{pmatrix} \boldsymbol{G}_1^{\beta} \\ \boldsymbol{G}_2^{\beta} \end{pmatrix}, \end{aligned} \tag{3.9}$$

where T represents the transpose operation on the matrix. The relationship between $\boldsymbol{L}_\mu^{\mathrm{c}}$ and $\boldsymbol{G}_\mu^{\mathrm{c}}$ is given by

$$\boldsymbol{L}_1^{\mathrm{c}} = \frac{S_{\mathrm{c}}}{2\pi}(\boldsymbol{G}_2^{\mathrm{c}} \times \boldsymbol{e}_z), \quad \boldsymbol{L}_2^{\mathrm{c}} = -\frac{S_{\mathrm{c}}}{2\pi}(\boldsymbol{G}_1^{\mathrm{c}} \times \boldsymbol{e}_z), \tag{3.10}$$

where $S_{\mathrm{c}}^* = (\boldsymbol{G}_1^{\mathrm{c}} \times \boldsymbol{G}_2^{\mathrm{c}})_z = (2\pi)^2/S_{\mathrm{c}}$ represents the area of the first Brillouin zone of the commensurate approximant, and $(\cdots)_z$ denotes the z-component perpendicular to the plane. Fig. 3.2(b) corresponds to the reciprocal lattice shown in Fig. 3.2(a).

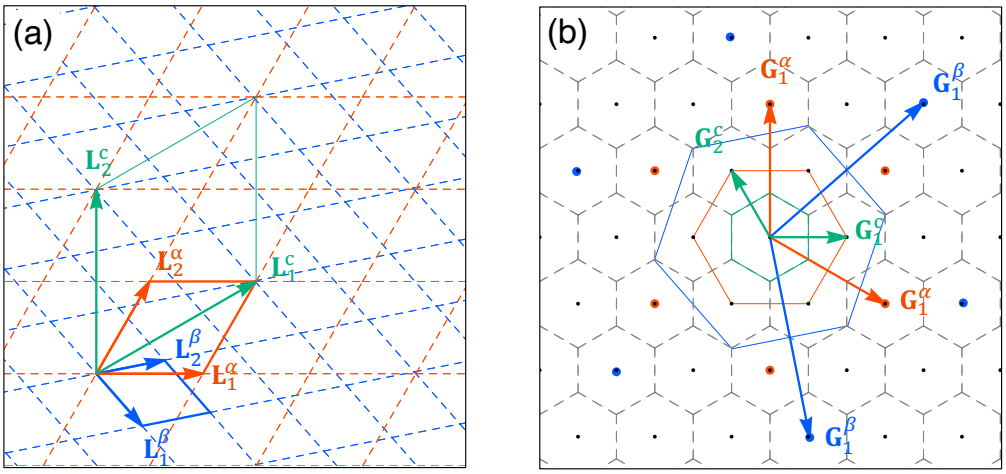

Figure 3.2: (a) Super moiré unit cell and (b) the corresponding reciprocal lattice of the commensurate approximant for $(\theta^\alpha, \theta^\beta) = (0, 1.1908°)$, where $(n_1^\alpha, n_2^\alpha) = (1, 1)$ and $(n_1^\beta, n_2^\beta) = (-1, 3)$.

Subsequently, we examine two series of hBN/graphene/hBN trilayer systems:

$$\begin{aligned} \mathrm{I}: \quad & (\theta^\alpha, \theta^\beta) = (0, \theta); \qquad && 0 \leq \theta \leq 2° \\ \mathrm{II}: \quad & (\theta^\alpha, \theta^\beta) = (\theta, -\theta); \qquad && 0 \leq \theta \leq 2° \end{aligned} \tag{3.11}$$

For each series, we determine a range of $(\theta^\alpha, \theta^\beta)$ values that fulfill the condition where $\Delta \boldsymbol{L}$ is bellow 1% of $|p_1 \boldsymbol{L}_1^\alpha + p_2 \boldsymbol{L}_2^\alpha|$ and $p_1, p_2 \leq n_{\max}$, with $p_{\max} = 12$ and 17 for series I and II, respectively.

3.2 Hamilotonian

Since hBN possesses a wide energy bandgap precisely at the Dirac point of graphene, the low-energy spectrum of the hBN/graphene/hBN system is primarily governed by the presence of Dirac cones originating from graphene. By straightforwardly extending the Hamiltonian of the bilayer graphene-hBN system, we can deduce the Hamiltonian of the trilayer continuum [43, 44, 45, 46, 47, 48, 49, 50, 51]. This Hamiltonian can be expressed in a matrix form of dimensions

6×6:

$$H_{\text{eff}} = \begin{pmatrix} H_{\text{G}} & U^{\alpha\dagger} & U^{\beta\dagger} \\ U^{\alpha} & H_{\text{hBN}} & 0 \\ U^{\beta} & 0 & H_{\text{hBN}} \end{pmatrix}. \tag{3.12}$$

This matrix operates on the basis of $\{A, B, A^{\alpha}, B^{\alpha}, A^{\beta}, B^{\beta}\}$. The H_{G}, a 2×2 matrix, represents the Hamiltonian of graphene and can be approximated as follows:

$$H_{\text{G}} \approx -\hbar v \boldsymbol{k} \cdot \boldsymbol{\sigma}_{\xi}. \tag{3.13}$$

In this equation, $\xi = \pm 1$ corresponds to the valley index of graphene and relates to the wave vector $\boldsymbol{K}_{\xi} = -\xi(2\boldsymbol{a}_1^* + \boldsymbol{a}_2^*)/3$. The relative wave number from the $\boldsymbol{K}_{\xi}$ point is denoted by $\boldsymbol{k}$, while $\boldsymbol{\sigma}_{\xi} = (\xi\sigma_x, \sigma_y)$ represents the Pauli matrices σ_x and σ_y. The H_{hBN} in the second and third diagonal blocks symbolizes the Hamiltonian of monolayer hBN. In this context, we adopt an approximation that solely accounts for the on-site potential as: [43, 47]

$$H_{\text{hBN}} \approx \begin{pmatrix} V_{\text{N}} & 0 \\ 0 & V_{\text{B}} \end{pmatrix}. \tag{3.14}$$

The off diagonal matrix U^{λ} is the interlayer Hamiltonians of the twist angle θ^{λ}, which is given by [47]

$$\begin{aligned} U^{\lambda} = t_0 \Bigg[& \begin{pmatrix} 1 & 1 \\ 1 & 1 \end{pmatrix} + \begin{pmatrix} 1 & \omega^{-\xi} \\ \omega^{\xi} & 1 \end{pmatrix} e^{i\xi \boldsymbol{G}_1^{\lambda} \cdot (\boldsymbol{r} - \boldsymbol{r}_0^{\lambda})} \\ & + \begin{pmatrix} 1 & \omega^{\xi} \\ \omega^{-\xi} & 1 \end{pmatrix} e^{i\xi (\boldsymbol{G}_1^{\lambda} + \boldsymbol{G}_2^{\lambda}) \cdot (\boldsymbol{r} - \boldsymbol{r}_0^{\lambda})} \Bigg], \end{aligned} \tag{3.15}$$

where $t_0 \approx 150\,\text{meV}$ is the interlayer coupling energy, and $\boldsymbol{r}_0^{\lambda}$ is the origin of the moiré pattern of layer λ, which can be changed by sliding the hBN layer relative to graphene [84].

The low-energy effective Hamiltonian for graphene can be derived by employing second-order perturbation theory to eliminate the hBN bases. It can be

explicitly expressed as:

$$H_{\mathrm{G}}^{(\mathrm{eff})} = H_{\mathrm{G}} + V_{\mathrm{hBN}}^{\alpha} + V_{\mathrm{hBN}}^{\beta}, \tag{3.16}$$

Here, the quantities $V_{\mathrm{hBN}}^{\lambda}$ are defined as follows:

$$\begin{aligned} V_{\mathrm{hBN}}^{\lambda} &\equiv U^{\lambda\dagger}(-H_{\mathrm{hBN}})^{-1}U^{\lambda} \\ &= V_0 \begin{pmatrix} 1 & 0 \\ 0 & 1 \end{pmatrix} + \Bigg\{ V_1 e^{i\xi\psi} \Bigg[\begin{pmatrix} 1 & \omega^{-\xi} \\ 1 & \omega^{-\xi} \end{pmatrix} e^{i\xi \boldsymbol{G}_1^{\lambda}\cdot(\boldsymbol{r}-\boldsymbol{r}_0^{\lambda})} \\ &+ \begin{pmatrix} 1 & \omega^{\xi} \\ \omega^{\xi} & \omega^{-\xi} \end{pmatrix} e^{i\xi \boldsymbol{G}_2^{\lambda}\cdot(\boldsymbol{r}-\boldsymbol{r}_0^{\lambda})} + \begin{pmatrix} 1 & 1 \\ \omega^{-\xi} & \omega^{-\xi} \end{pmatrix} e^{i\xi \boldsymbol{G}_3^{\lambda}\cdot(\boldsymbol{r}-\boldsymbol{r}_0^{\lambda})} \Bigg] + \mathrm{h.c.} \Bigg\}, \end{aligned} \tag{3.17}$$

with

$$V_0 = -3t_0^2 \left(\frac{1}{V_{\mathrm{N}}} + \frac{1}{V_{\mathrm{B}}} \right), \tag{3.18}$$

$$V_1 e^{i\psi} = -t_0^2 \left(\frac{1}{V_{\mathrm{N}}} + \omega \frac{1}{V_{\mathrm{B}}} \right). \tag{3.19}$$

Additionally, we have $\boldsymbol{G}_3^{\lambda} = -\boldsymbol{G}_1^{\lambda} - \boldsymbol{G}_2^{\lambda}$, with the approximate values $V_0 \approx 29\,\mathrm{meV}$, $V_1 \approx 21\,\mathrm{meV}$, and $\psi \approx -0.29(\mathrm{rad})$ [47].

By utilizing the effective Hamiltonian described in Eq. (3.12), we proceed to compute the band structure of the approximate commensurate systems introduced in the preceding section. The set of wavevectors that undergo hybridization due to the commensurate double moiré pattern is expressed as $\boldsymbol{q}_{m_1,m_2} = \boldsymbol{k} + m_1\boldsymbol{G}_1^{\mathrm{c}} + m_2\boldsymbol{G}_2^{\mathrm{c}}$, where m_1 and m_2 denote integers, and $\boldsymbol{k}$ represents a residual wavevector confined within the first Brillouin zone of the super-moiré (commensurate approximant) spanned by $\boldsymbol{G}_1^{\mathrm{c}}$ and $\boldsymbol{G}_2^{\mathrm{c}}$. To construct the Hamiltonian matrix within the graphene bases, $\{|\boldsymbol{q}_{m_1,m_2}, A\rangle, |\boldsymbol{q}_{m_1,m_2}, B\rangle\}$, we impose a k-space cut-off such that $|\boldsymbol{q}_{m_1,m_2}| < q_c$, which corresponds to approximately 0.54 eV for $\theta^{\beta} = 0°$. Ultimately, the band diagram is acquired by plotting the eigenvalues of the Hamiltonian matrix as a function of $\boldsymbol{k}$.

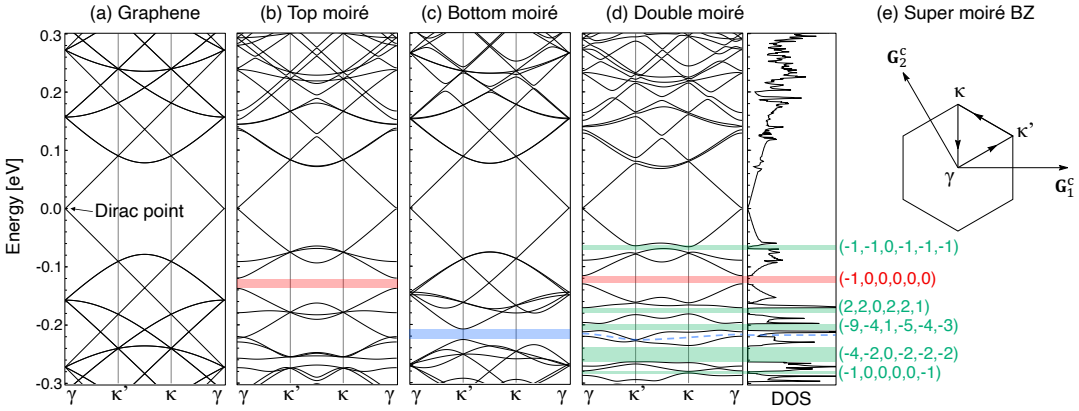

Figure 3.3: Band structure of $(\theta^\alpha, \theta^\beta) = (0°, 1.1908°)$. Panel (d) exhibits the energy band of the complete double moiré potential, depicted along the symmetrical path of the super moiré Brillouin zone illustrated in (e), accompanied by the corresponding density of states (DOS) on the right-hand side. To facilitate comparison, we also present the energy bands of (a) intrinsic graphene without any moiré potentials, (b) solely the top moiré potential, and (c) solely the bottom moiré potential, all plotted along the same trajectory. The first-order gaps arising from the top (bottom) moiré potential are represented by the color red (blue), while the double-moiré gaps are indicated in green. The dashed blue curve in panel (d) represents the position of the first-order gap associated with the bottom moiré potential, which, in reality, remains unopened.

3.3 Results

3.3.1 Electronic spectrum

Illustrating a representative example, we present the band structure of the commensurate approximant with $(\theta^\alpha, \theta^\beta) = (0, 1.1908°)$, as depicted in Fig. 3.2. For convenience, we set the origins of the moiré potentials, $\boldsymbol{r}_0^\alpha$ and bmr_0^β, to zero. Fig. 3.3(d) shows the energy band plotted along the symmetric line of the super moiré Brillouin zone. For comparison, we also provide the band structures for (a) intrinsic graphene without any moiré potential, (b) solely the top moiré potential

($\lambda = \alpha$), (c) solely the bottom moiré potential ($\lambda = \beta$), all depicted along the same path. In all panels, the energy origin (vertical axis) is set at the Dirac point of graphene. In the case of single moiré systems illustrated in Fig. 3.3(b) and (c), the most prominent gap in the valence band (red/blue regions) corresponds to the first-order moiré gap, representing the electron density of one electron (per valley and per spin) per moiré unit cell. Conversely, in the double moiré system, we observe a sequence of higher-order gaps (green) arising from the coexistence of different moiré periods.

In order to investigate the twist-angle dependence of the electronic spectrum, we conduct band calculations for all the systems in series I and II, as defined in Eq. (3.11). For commensurate systems, the band structure is influenced by the relative translation of the moiré potentials, denoted as $\Delta\boldsymbol{r}_0 = \boldsymbol{r}_0^\alpha - \boldsymbol{r}_0^\beta$. The magnitude of this dependence is generally more pronounced in systems with smaller L_{SM} (super-moiré size), and it diminishes rapidly as L_{SM} increases. To obtain averaged results, we compute the density of states (DOS) by averaging over 25 grid points of $\Delta\boldsymbol{r}_0$ for systems with $L_{\mathrm{SM}} < 50$ nm. For systems with larger L_{SM}, we simply set $\Delta\boldsymbol{r}_0$ to zero, as the dependence on $\Delta\boldsymbol{r}_0$ is negligible.

Fig. 3.4(a) illustrates the color map presenting the density of states (DOS) computed for series I, characterized by the twist angles $(\theta^\alpha, \theta^\beta) = (0, \theta^\beta)$. The map shows the DOS variation with respect to θ^β and energy. Notably, brighter colors indicate higher DOS values, while the dark blue color represents the existence of a gap. The upper part of the figure comprises an array of bars representing the different θ^β values within series I. The specific case of $(\theta^\alpha, \theta^\beta) = (0, 1.1908°)$, as examined in Fig. 3.3, is labeled as (ii).

Fig. 3.4(c) showcases the lower segment of (a), delineating the highlighted red and blue curves that represent the first-order gaps of the single moiré potentials $\lambda = \alpha$ and β, respectively. Additionally, notable higher-order gaps are demarcated by green curves. In Fig. 3.4(b), we observe the corresponding energy gap map with the vertical axis converted to electron density. The size of the black

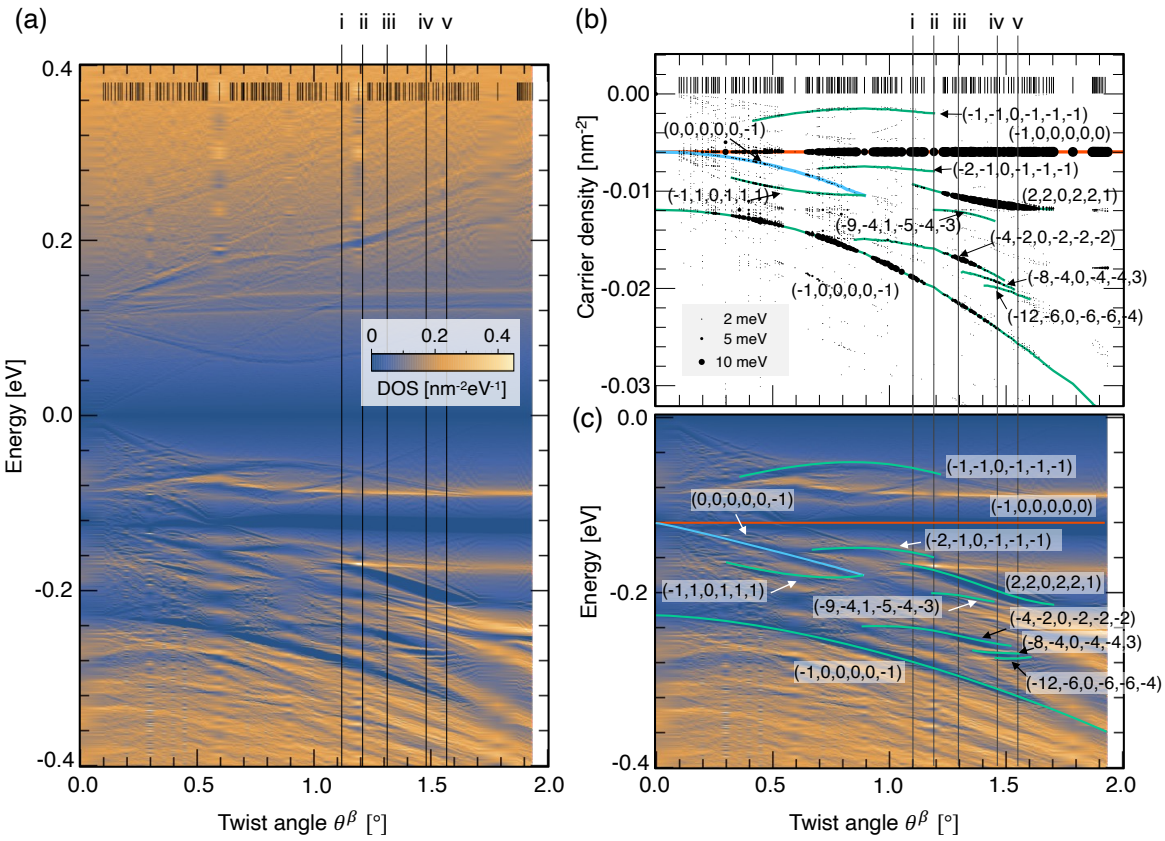

Figure 3.4: (a) Color-coded representation of the density of states (DOS) for series I $[(\theta^\alpha, \theta^\beta) = (0, \theta^\beta)]$, plotted as a function of θ^β and energy. The upper portion of the figure displays an array of bars corresponding to the listed values of θ^β. (c) The lower portion of (a) highlights the first-order gaps of the single moiré patterns $\lambda = \alpha$ and β with red and blue curves, respectively, while the green curves mark higher-order gaps. (b) The accompanying map depicts the energy gaps, where the vertical axis is converted to electron density and the size of black dots represents the gap width.

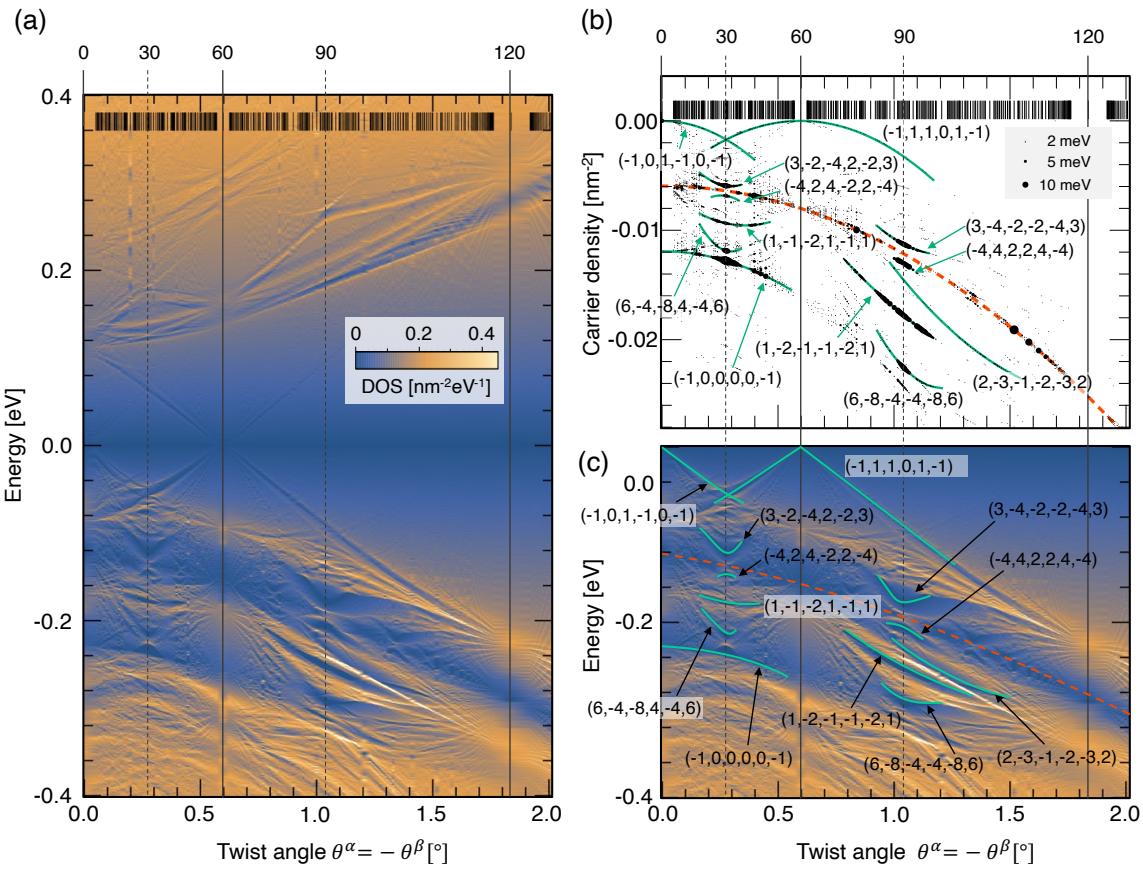

Figure 3.5: Plots similar to Fig. 3.4 are shown for series II $[(\theta^{\alpha}, \theta^{\beta}) = (\theta, -\theta)]$. The numbers at the top (0, 30, $\cdots$, 120) indicate the relative angle between the two moiré patterns, $\phi^{\beta} - \phi^{\alpha}$.

dots in this representation signifies the width of the respective gaps. These plots demonstrate the continuous variation of the spectrum as a function of the twist angle, irrespective of the fact that adjacent approximants in the series exhibit distinct super moiré periods and, consequently, different numbers of minibands.

Fig. 3.4(c) shows the lower part of (a), wherein the red and blue curves highlight the first-order gaps associated with the single moiré potentials $\lambda = \alpha$ and β, respectively. Additionally, typical higher-order gaps are denoted by green curves. Fig. 3.4(b) corresponds to the map of energy gaps, where the vertical axis is transformed into electron density. The size of the black dots in this representation represents the width of the respective gaps. These plots demonstrate the continuous variation of the spectrum as a function of the twist angle, even in the presence of adjacent approximants with distinct super moiré periods and, consequently, different numbers of minibands.

Fig. 3.5 exhibits similar plots for the series II, plotted against $\theta^\alpha = -\theta^\beta$. The numbers at the top (0, 30, $\cdots$, 120) indicate $\phi^\beta - \phi^\alpha$, which corresponds to the relative angle between the two moiré patterns. For $\theta^\alpha \approx 0.5972°$ and $\theta^\alpha \approx 1.8377°$, the relative angles of the two moiré patterns are 60° and 120°, respectively, resulting in complete overlap of the two moiré periods. Consequently, there is a relatively small number of subbands due to this double-period coincidence. However, as we move away from these angles, we observe the emergence of numerous tiny levels, reminiscent of Landau levels in a magnetic field.

The red dashed curve in Figs. 3.5(b) and (c) represents the positions of the first-order gaps for the two moiré patterns, which precisely match due to the condition $|\theta^\alpha| = |\theta^\beta|$. Interestingly, throughout the figure, the first-order gap closes along the dashed line, leaving behind a small region with finite density of states (DOS). The reason for the absence of the first-order gap will be elucidated in the subsequent section.

3.3.2 Topological invariants for band gaps

The microgap structure observed in Fig. 3.4 and 3.5 bears a resemblance to the Hofstadter butterfly [60], which represents the energy spectrum of a two-dimensional periodic lattice subjected to a magnetic field. In essence, the Hofstadter system can be regarded as a one-dimensional Hamiltonian with a double period [104, 105], where a fractal minigap structure emerges as the relative positions of the two periods are altered. Each minigap is characterized by a pair of integers, denoted as p and q, whereby the electron density below the gap is given by the expression $n_e = (pG^\alpha + qG^\beta)/(2\pi)$, with G^α and G^β representing the wavenumbers associated with the two periods. In the context of the hBN/-graphene/hBN system at hand, we encounter a two-dimensional analog of the aforementioned scenario, wherein the double period is specified by $(\boldsymbol{G}_1^\alpha, \boldsymbol{G}_2^\alpha)$ and $(\boldsymbol{G}_1^\beta, \boldsymbol{G}_2^\beta)$. Notably, as we shall demonstrate subsequently, all the observed gaps depicted in Figures 3.4 and 3.5 can be distinctly characterized by *six* topological integers that are associated with specific regions in the k-space.

Let us consider a general situation where the two moire patterns are incommensurate. In this context, we can establish four distinct unit areas by combining the four independent reciprocal lattice vectors, denoted as $\{\boldsymbol{G}_1, \boldsymbol{G}_2, \boldsymbol{G}_3, \boldsymbol{G}_4\} = \{\boldsymbol{G}_1^\alpha, \boldsymbol{G}_2^\alpha, \boldsymbol{G}_1^\beta, \boldsymbol{G}_2^\beta\}$. These unit areas, depicted in Fig. 3.6, can be defined as follows:

$$S_{ij}^* = (\boldsymbol{G}_i \times \boldsymbol{G}_j)_z, \quad S_{ij} = (2\pi)^2/S_{ij}^*, \tag{3.20}$$

Here the notation $(\cdots)_z$ indicates the z-component that is perpendicular to the plane. It should be noted that this component may assume negative values depending on the relative angles between the two vectors. Specifically, S_{12}^* and S_{34}^* represent the Brillouin-zone areas of the individual moiré patterns for $\lambda = \alpha$ and β respectively, while the remaining terms correspond to cross terms that combine the reciprocal vectors of the different moiré patterns.

The areas S_{ij}'s can be regarded as the projection of faces of four-dimensional

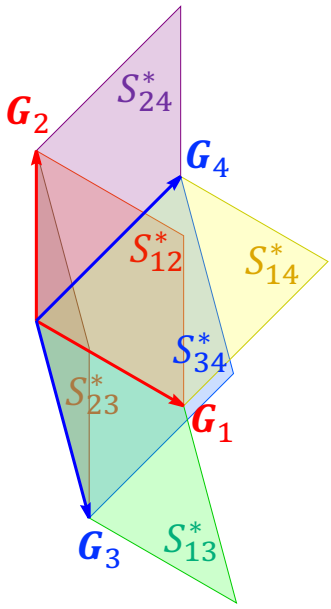

Figure 3.6: Independent unit area elements $\{S^*_{12}, S^*_{13}, S^*_{14}, S^*_{23}, S^*_{24}, S^*_{34}\}$ obtained by cross product of the reciprocal lattice vectors $\{\mathbf{G}_1, \mathbf{G}_2, \mathbf{G}_3, \mathbf{G}_4\}$ in hBN/-graphene/hBN double-moiré system [Eq. (3.20)].

hypercube onto the physical 2D plane, which is analogous to the general argument of the quasicrystal [106].

In a conventional periodic 2D system with primitive reciprocal lattice vectors $\boldsymbol{G}_1$ and $\boldsymbol{G}_2$, the electronic spectrum is separated into Bloch subbands, each of which accomodates the electron density $|\boldsymbol{G}_1 \times \boldsymbol{G}_2|/(2\pi)^2$. In a doubly-periodic 2D system, in contrast, the areas S^*_{ij} all serve as units of the spectrum separation. More specifically, we find that the electron density (per spin and valley) from the Dirac point to any gap in the hBN/graphene/hBN system can be uniquely expressed with *six* integers $\nu_{12}, \nu_{13}, \nu_{14}, \nu_{23}, \nu_{24}, \nu_{34}$ as

$$n_e = \frac{1}{(2\pi)^2} \sum_{\langle i,j \rangle} \nu_{ij} S^*_{ij} = \sum_{\langle i,j \rangle} \frac{\nu_{ij}}{S_{ij}}. \tag{3.21}$$

These integers ν_{ij} are topological invariants i.e., they never changes as long as the gap survives in a continuous change of the moire pattern.

Fig. 3.4(c) shows the values of ν_{ij} determined for significant gaps in case I.

Fig. 3.4(b) represents the same plot, but with the electron density n_e as the vertical axis, where the black dots indicate spectral gaps with their sizes representing the gap width. In the case of commensurate systems, the integers $\nu_{12}, \cdot, \nu_{34}$ can be determined from the commensurate approximants as follows.

When the S^*_{ij}'s have a greatest common divisor $S_{\rm c} = (\boldsymbol{G}^{\rm c}_1 \times \boldsymbol{G}^{\rm c}_2)_z$, they can be expressed as $S^*_{ij} = s_{ij} S^*_{\rm c}$ using integers s_{ij}. The electron density n_e is also quantized in units of $S^*_{\rm c}/(2\pi)^2$, and each band gap is characterized by an integer $r = n_e/[S^*_{\rm c}/(2\pi)^2]$, which is the number of occupied subbands counted from the Dirac point. Thus Eq. (3.21) becomes the Diophantine equation $r = \sum_{\langle i,j \rangle} \nu_{ij}(p_i q_j - p_j q_i)$. For each gap in Fig. 3.4(c), we have the Diophantine equations as many as the number of the data points (i.e., the different systems), and the $(\nu_{12}, \nu_{13}, \nu_{14}, \nu_{23}, \nu_{24}, \nu_{34})$ is obtained as a unique solution of the set of equations. Here note that the area $\sum_{\langle i,j \rangle} \nu_{ij} S^*_{ij}$ is a continuous function of the twist angle, while $S^*_{\rm c}$ (and thus r, s_{ij}) can only be defined for commensurate systems and it discontinuously changes in changing the twist angle. This result indicates that the same $(\nu_{12}, \ldots, \nu_{34})$ are shared by infinitely many commensurate approximants (with $S^*_{\rm c}$ ranging from 0 to infinity) which exist in a close vicinity of a specific $(\theta^\alpha, \theta^\beta)$, and hence it is valid in the limit of $S^*_{\rm c} \to \infty$, i.e., incommensurate systems.

Figures 3.5 (b) and (c) are similar plots for the case II. Here the condition $|\theta^\alpha| = |\theta^\beta|$ enforces $S^*_{12} = S^*_{34}$, and then ν_{12} and ν_{34} becomes indeterminate. To resolve these two integers, we can consider an infinitesimal rotation of either the top or bottom hBN layer. Interestingly, it emerges that $\nu_{12} = \nu_{34}$ for all gaps in case II. This fact can be explicitly demonstrated as follows: Let us start with a case II system $(\theta^\alpha, \theta^\beta) = (\theta, -\theta)$, and then consider two distinct systems: $X : (\theta^\alpha, \theta^\beta) = (\theta + \delta\theta, -\theta)$ and $X' : (\theta^\alpha, \theta^\beta) = (\theta, -\theta - \delta\theta)$. Remarkably, X and X' are identical when the entire system is rotated by 180° with respect to an in-plane axis. Consequently, they exhibit exactly the same energy spectrum. However, the same energy gap is labeled by different sets of integers, denoted as ν_{ij} and $\nu_{ij}{}'$ for X

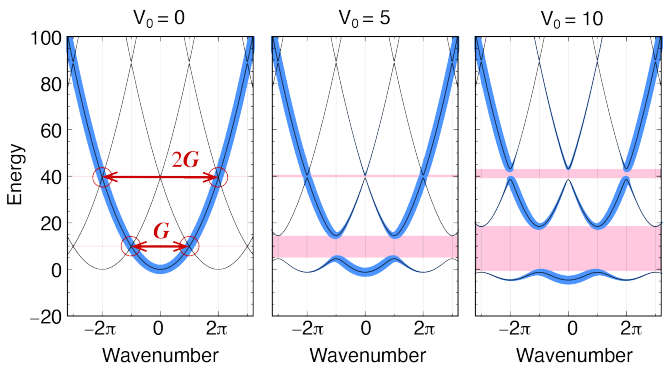

Figure 3.7: Band structure of a one-dimensional Hamiltonian $H = -\partial^2/\partial x^2 + 2V_0 \cos Gx$ with $V_0 = 0, 5, 10$. The black solid lines represent the band dispersion ε_{nk} in the extended zone scheme, and the size of blue points indicates the spectral weight projected onto the plain wave, denoted as $A(q, \varepsilon)$.

and X' respectively, such that $\sum_{\langle i,j \rangle} \nu_{ij} S^*_{ij} = \sum_{\langle i,j \rangle} \nu_{ij}{}' S^*_{ij}{}'$. By interchanging the layers $\lambda = \alpha, \beta$ during the 180° rotation process, the unit areas of X and X' become related as $(S^*_{12}, S^*_{13}, S^*_{14}, S^*_{23}, S^*_{24}, S^*_{34}) = (S^*_{34}{}', S^*_{13}{}', S^*_{14}{}', S^*_{23}{}', S^*_{24}{}', S^*_{12}{}')$. Consequently, the condition $(\nu_{12}, \nu_{13}, \nu_{14}, \nu_{23}, \nu_{24}, \nu_{34}) = (\nu_{34}{}', \nu_{13}{}', \nu_{14}{}', \nu_{23}{}', \nu_{24}{}', \nu 12')$ arises. In the limit of $\delta\theta \to 0$ and the gap persists, we obtain $\nu_{ij} = \nu_{ij}{}'$, leading us to the conclusion that $\nu_{12} = \nu_{34}$. The constraint $\nu_{12} = \nu_{34}$ provides an explanation as to why the first-order gaps of individual moiré potentials, $(\pm 1, 0, 0, 0, 0, 0)$ and $(0, 0, 0, 0, 0, \pm 1)$ cannot open in Fig. 3.5(b).

The interdependence among the six unit areas $S^*_{12}, \cdots, S^*_{34}$ can be disrupted through the uniform distortion of either the top or bottom hBN layer, resulting in the breaking of its 180° symmetry. If we expand the parameter space to include these distorted systems, we would require six topological integers $(\nu_{12}, \cdots, \nu_{34})$ to characterize the minigaps, where the electron density is expressed as $\sum_{\langle i,j \rangle} \nu_{ij} S^*_{ij}$. This scenario is analogous to the situation observed in series II, where ν_{12} and ν_{34} can be differentiated by violating the condition $S^*_{12} = S^*_{34}$.

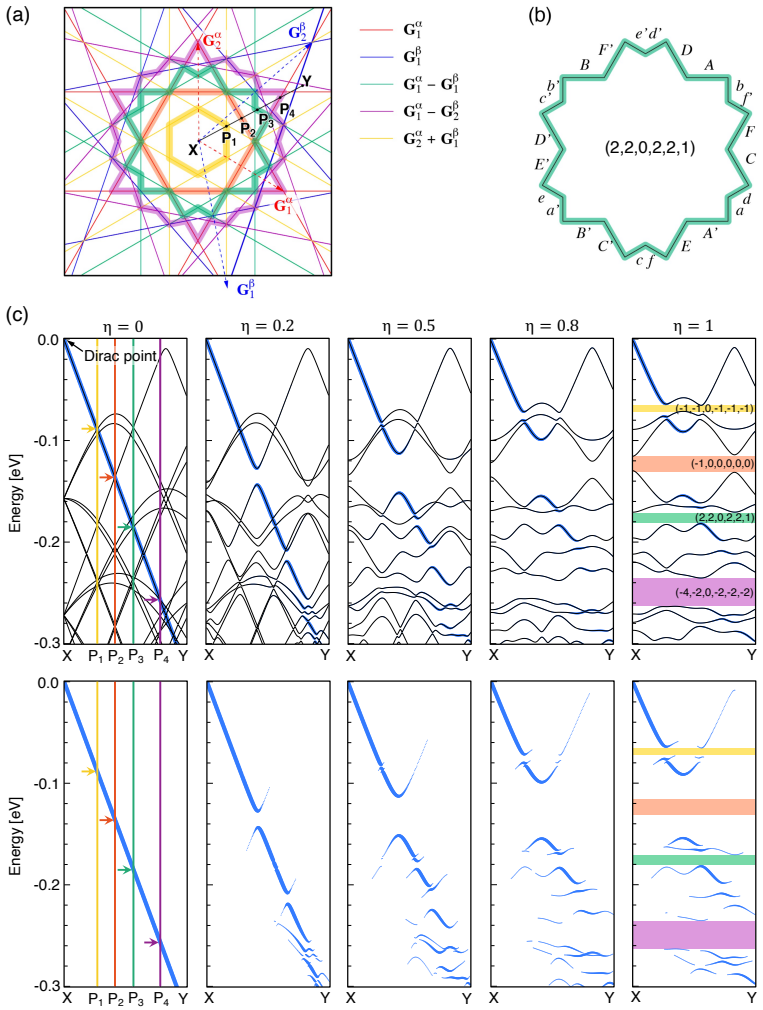

Figure 3.8: (a) The quasi-Brillouin zones are shown for $(\theta^\alpha, \theta^\beta) = (0°, 1.1908°)$, with different colored thick lines corresponding to the four indicated gaps in (c). The thin lines represent the Bragg planes associated with different reciprocal lattice vectors. For instance, the red lines denote the perpendicular bisector of $\boldsymbol{G}_1^\alpha$ and its $60n°$ rotation. (b) The quasi-Brillouin zone is illustrated for the gap $(2, 2, 0, 2, 2, 1)$, where x and x' represent a pair of boundary segments connected by the moiré potential. (c) The band structure along the path from X to Y, as shown in (a) is calculated for $(0°, 1.1908°)$ with the moiré potentials reduced by a factor $\eta\,(0 \leq \eta \leq 1)$. The solid black lines represent the band dispersion plotted in the extended zone scheme, and the blue dots represent the spectral weight $A(\boldsymbol{q}, \varepsilon)$. The bottom panels depict the same plot without the band lines.

3.4 Quasi-Brillouin Zone

Actually, the area $\sum_{\langle i,j\rangle} \nu_{ij} S^*_{ij}$ can be attributed to a specific region within the momentum space, commonly referred to as the quasi-Brillouin zone. In a conventional periodic two-dimensional system defined by $\boldsymbol{G}_1$ and $\boldsymbol{G}_2$, the Brillouin zones (indexed by $n = 1, 2, 3 \cdots$) are delineated by a series of distinct regions enclosed by the Bragg planes, which are the perpendicular bisectors of the reciprocalvectors $n_1\boldsymbol{G}_1 + n_2\boldsymbol{G}_2$ [107]. Notably, each Brillouin zone possesses an identical area of $|\boldsymbol{G}_1 \times \boldsymbol{G}_2|$. Consequently, the carrier density beneath any gap is quantized to an integer multiple of this area.

In a doubly-periodic two-dimensional system, analogously, we can establish the concept of a quasi-Brillouin zone as an enclosed region delineated by the Bragg planes associated with composite reciprocal vectors $p\boldsymbol{G}_1^\alpha + q\boldsymbol{G}_2^\alpha + r\boldsymbol{G}_1^\beta + s\boldsymbol{G}_2^\beta$. This notion of quasi-Brillouin zones has been employed in the study of conventional three-dimensional quasicrystals, such as Al-Mn alloys, to elucidate the presence of pseudogaps and system stability [70]. In the case of incommensurate systems, where the reciprocal space is filled by an infinite number of Bragg planes, the systematic definition of quasi-Brillouin zones, as observed in periodic systems, becomes elusive. Nevertheless, we propose that each individual gap in the spectrum can be associated with a distinct geometric shape, whose area corresponds to $\sum_{\langle i,j\rangle} \nu_{ij} S^*_{ij}$. These shapes may include simple hexagons defined by single reciprocal vectors, as explored in previous studies [26, 30, 31]. However, more generally, they can manifest as non-convex polygons comprising multiple segments derived from different Bragg planes, as depicted in Fig. 3.8(a).

The configuration of the quasi-Brillouin zone associated with a particular gap can be precisely determined by considering the projection of plane waves onto the zero potential limit. To illustrate this scheme, let us consider a simple one-dimensional Hamiltonian with a single periodic potential of the form $H = -\partial^2/\partial x^2 + 2V_0 \cos Gx$, where $G = 2\pi$. The eigenenergies and eigenfunctions are

denoted as ε_{nk} and $|\psi_{nk}\rangle$, respectively, where n represents the band index and k is the Bloch wavenumber confined to the first Brillouin zone ($-\pi \leq k \leq \pi$). Fig. 3.7 displays the calculated band structures for different potential amplitudes $V_0 = 0, 5, 10$. The solid black lines depict the band dispersion ε_{nk} plotted within the extended zone scheme, while the size of the superimposed blue dots corresponds to the spectral weight projected onto the plane wave. This projection is given by the expression

$$A(q, \varepsilon) = \sum_{n,k} |\langle q|\psi_{nk}\rangle|^2 \delta(\varepsilon - \varepsilon_{nk}), \tag{3.22}$$

where $|q\rangle = e^{iqx}$ represents the plane wave with $-\infty < q < \infty$, and the summation over k extends across over the first Brillouin zone. The pink regions indicate the positions of the first and second energy gaps. As the potential amplitude V_0 decreases, the gaps become narrower, and the spectral weight gradually converges to a simple parabolic form $\varepsilon = q^2$. In the limit of $V_0 \to 0$, we can pinpoint the specific points on the parabola where the energy gaps emerge within infinitesimal V_0 (indicated by red circles). Remarkably, these points precisely delineate the boundaries of the Brillouin zone.

The same approach is applicable to the double-period system. In our hBN/-graphene/hBN system, we define the spectral weight as follows:

$$A(\boldsymbol{q}, \varepsilon) = \sum_{\alpha} \sum_{X} |\langle \boldsymbol{q}, X|\psi_\alpha\rangle|^2 \delta(\varepsilon - \varepsilon_\alpha), \tag{3.23}$$

where ε_α and $|\psi_\alpha\rangle$ denote the eigenenergy and eigenstates of the system, respectively. Additionally $|\boldsymbol{q}, X\rangle$ represents the plain wave basis associated with the sublattice $X = A, B$ of the monolayer graphene. For instance, we consider the commensurate approximant corresponding to $(\theta^\alpha, \theta^\beta) = (0°, 1.1908°)$, as depicted in Figs. 3.2 and 3.3. We compute the eigenstates of the Hamiltonian given by Eq. (3.12) by varying the moiré potentials $(V^\alpha_{\text{hBN}}, V^\beta_{\text{hBN}})$ with a reduction factor $\eta\,(0 \leq \eta \leq 1)$. In Fig. 3.8(c), the band structures are illustrated for different values of η ranging from 0 to 1 along a path from X (the graphene's Dirac point) to a specific point Y shown in Fig. 3.8(a). The solid black lines represent the band

dispersion plotted in the extended zone scheme, while the blue dots represent the spectral weight $A(\boldsymbol{q}, \varepsilon)$. At $\eta = 0$, the system exhibits the graphene's Dirac cone. By tracking the gap openings in the spectral weight as η decreases from 1 to 0, we can accurately identify the points where gaps emerge, analogous to the one-dimensional case.

In Fig. 3.8(c), we examine four gaps characterized by distinct indices $(\nu_{12}, ..., \nu_{34})$. The $(-1, 0, 0, 0, 0, 0)$ is the first-order gap of the moiré potential $\lambda = \alpha$, and others are double-moire gaps caused by the coexistence of the two moiré patterns. As we approach the limit $\eta \to 0$, we identify the wave numbers $P_1, \cdots, P_4$ at which these gaps open. By repeating this process for paths in various directions, we ultimately obtain the quasi Brillouin zone on the (k_x, k_y) plane, represented by the trajectories of $P_1, \cdots, P_4$. These trajectories are depicted as thick colored lines in Fig. 3.8(a). The figures comprising the quasi Brillouin zone consist of segments of the Bragg planes, illustrated as thin lines. The first-order gap $(-1, 0, 0, 0, 0, 0)$ yields a regular hexagon, which corresponds to the first Brillouin zone of the moiré potential with $\lambda = \alpha$. The double-moire gap $(-1, -1, 0, -1, -1, -1)$ also results in a hexagonal shape, albeit smaller in size, representing the first Brillouin zone associated with a small reciprocal lattice vectors $\boldsymbol{G}2^{\alpha} + \boldsymbol{G}1^{\beta}$. In contrast, the gaps $(2, 2, 0, 2, 2, 1)$ and $(-4, -2, 0, -2, -2, -2)$ manifest as intricate, flower-like structures composed of multiple segments of Bragg lines. In all cases, the area of these figures is precisely equivalent to $\sum_{\langle i,j \rangle} \nu_{ij} S^*_{ij}$. Analogous to the conventional Brillouin zone in periodic systems, the quasi Brillouin zone is also a closed object, wherein each side of the boundary seamlessly connects to the other side. Consequently, crossing the boundary will never lead one outside of the region.

The quasi Brillouin zone undergoes continuous transformations as the twist angle varies, irrespective of the unit cell size of the commensurate approximants. Fig. 3.9 illustrates this behavior for a slightly different angle $(\theta^{\alpha}, \theta^{\beta}) = (0, 1.2967°)$ [(iii) in Fig. 3.4]. In this case, the super moiré unit area of the system is approximately ten times larger than that of Fig. 3.8(c), resulting in a higher density

of band lines due to the band folding into the smaller Brillouin zone. However, when observing the spectral weight (blue dots), we observe a similar structure to Fig. 3.8(c), with the exception that the gap $(-1, -1, 0, -1, -1, -1)$ is not fully open. Nonetheless, in the limit of $\eta \to 0$, the gaps close at the Bragg planes with the same indices. Consequently, we obtain a quasi Brillouin zone shape that is nearly identical to that shown in Fig. 3.10(iii). In Fig. 3.9, numerous additional band lines overlap but contribute minimally to the spectral weight. As a result, they are disregarded in the determination of the zone boundary. This approach differs from one that sorts all eigenvalues in energy and tracks the same level index in the limit of zero potential [69], which is influenced by all overlapping band lines.

In Fig. 3.10, we present the continuous evolution of the quasi Brillouin zones as a function of the twist angle from (i) to (v) (corresponding to the labels in Fig. 3.4). The figures exhibit continuous changes regardless of the abrupt variations in the precise period of the approximants. The areas of these figures consistently equal $\sum_{\langle i,j \rangle} \nu_{ij} S^*_{ij}$.

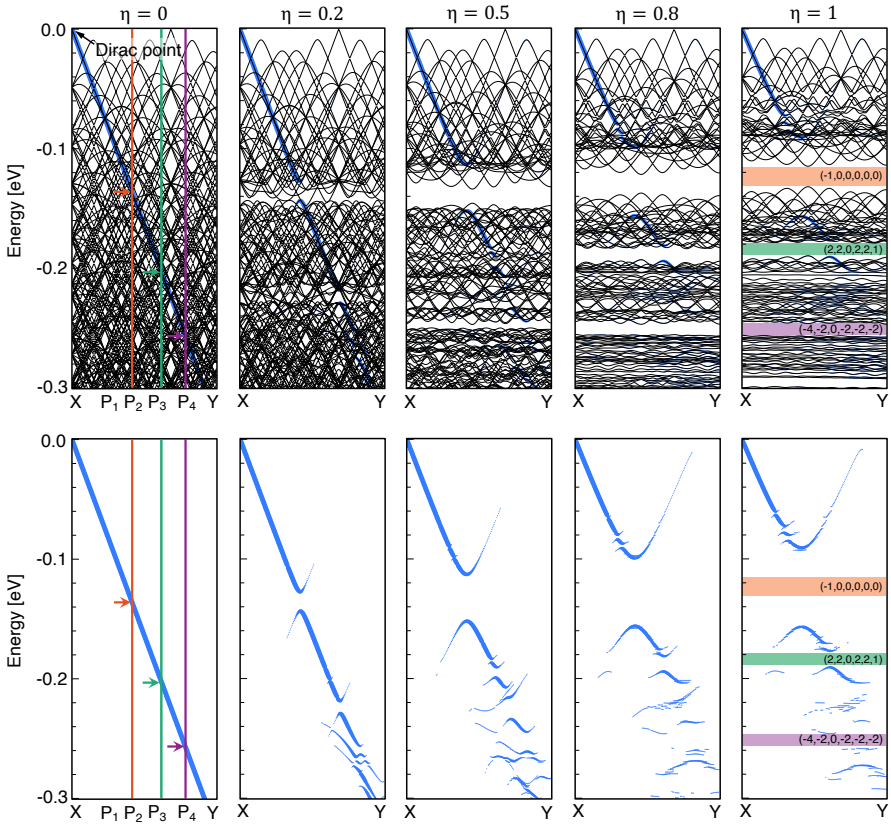

Figure 3.9: Plot resembling Fig. 3.8(c) computed for $(\theta^\alpha, \theta^\beta) = (0°, 1.2967°)$.

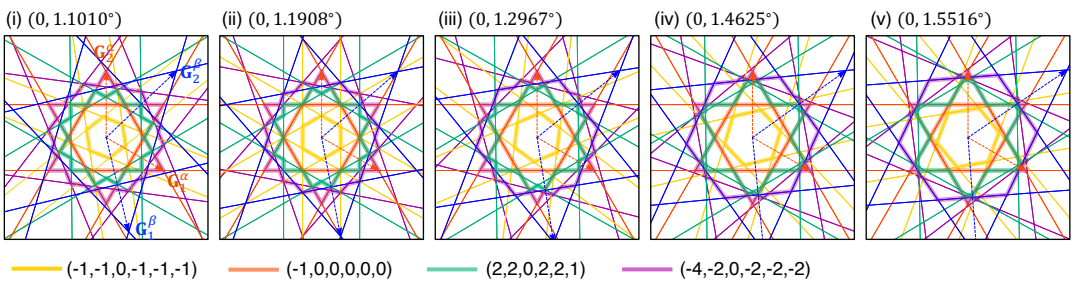

Figure 3.10: Quasi Brillouin zones akin to Fig. 3.8(a) calculated for five distinct angles. The indices (i) to (v) correspond to the labels in Fig. 3.4.

Chapter 4

Twisted quasicrystal

In the preceding chapter, we elucidated the fractal energy bands within the hBN/graphene/hBN doubly periodic system, wherein we discerned characteristic integers nestled within the band gaps. Within this chapter, we expound upon the physical significance of these integers as the Chern number, utilizing a generalized plane wave model. We employed a dual-plane wave potential with a twist, and we present the results of numerical computations that mirror the fractal band gaps akin to those in the prior chapter. Within these fractal band gaps, one encounters characteristic integers that correspond to the dimensions of the quasi-Brillouin zone. Subsequently, we demonstrate how these integers can be derived through the contemplation of adiabatic charge pumping. Finally, we articulate the formulation of the four-dimensional quantum Hall effect, thereby establishing an unequivocal equivalence between these characteristic integers and the second Chern number.

4.1 Zone quantum numbers

4.1.1 General formulation

We consider a doubly-periodic 2D Hamiltonian given by

$$H = \frac{\boldsymbol{p}^2}{2m} + V^\alpha(\boldsymbol{r}) + V^\beta(\boldsymbol{r}). \tag{4.1}$$

Here, $V^\lambda(\boldsymbol{r})\,(\lambda = \alpha, \beta)$ represents a periodic potential defined as

$$V^\lambda(\boldsymbol{r}) = \sum_{m_1,m_2} V^\lambda_{m_1,m_2}\, e^{i(m_1\boldsymbol{b}_1^\lambda + m_2\boldsymbol{b}_2^\lambda)\cdot\boldsymbol{r}}, \tag{4.2}$$

where $\boldsymbol{b}_1^\lambda, \boldsymbol{b}_2^\lambda$ are the reciprocal lattice vectors, previously denoted as $\boldsymbol{G}_1^\lambda, \boldsymbol{G}_2^\lambda$. The real-space lattice vectors are denoted as $\boldsymbol{a}_1^\lambda, \boldsymbol{a}_2^\lambda$, satisfying $\boldsymbol{a}_\mu^\lambda \cdot \boldsymbol{b}_\nu^\lambda = 2\pi\delta_{\mu\nu}$, serving a similar role to $\boldsymbol{L}_1^\lambda, \boldsymbol{L}_2^\lambda$. For simplicity, we fix the labels of the four reciprocal lattice vectors as

$$(\mathbf{b}_1, \mathbf{b}_2, \mathbf{b}_3, \mathbf{b}_4) = (\mathbf{b}_1^\alpha, \mathbf{b}_2^\alpha, \mathbf{b}_1^\beta, \mathbf{b}_2^\beta). \tag{4.3}$$

We propose that in the presence of an energy gap in the spectrum, the electron density below the gap is quantized as

$$n_e = \frac{1}{(2\pi)^2}\sum_{\langle i,j\rangle} \nu_{ij} S^*_{ij} = \sum_{\langle i,j\rangle} \frac{\nu_{ij}}{S_{ij}}. \tag{4.4}$$

Here, ν_{ij} (with $i, j = 1, 2, 3, 4$) are zone quantum numbers that characterize the gap, and $\langle i, j\rangle$ represents a pair of distinct indices. S^*_{ij} and S_{ij} are defined as

$$S^*_{ij} = (\boldsymbol{b}_i \times \boldsymbol{b}_j)_z, \quad S_{ij} = (2\pi)^2/S^*_{ij}, \tag{4.5}$$

where $(\cdots)_z$ denotes the z-component perpendicular to the plane. S^*_{ij} represents the momentum space area spanned by two distinct reciprocal lattice vectors chosen from $\boldsymbol{b}_1, \boldsymbol{b}_2, \boldsymbol{b}_3, \boldsymbol{b}_4$, while S_{ij} corresponds to its real-space counterpart. We have six independent areas $S^*_{12}, S^*_{13}, S^*_{14}, S^*_{23}, S^*_{24}, S^*_{34}$ as illustrated in Fig. 4.1(a), and we have $S^*_{ji} = -S^*_{ij}$ and $S^*_{ii} = 0$ from the definition. Accordingly, we have

six zone quantum numbers $\nu_{12}, \nu_{13}, \nu_{14}, \nu_{23}, \nu_{24}, \nu_{34}$, and we define $\nu_{ji} = -\nu_{ij}$ and $\nu_{ii} = 0$ for consistency. The areas S^*_{ij} can be considered as the projection of faces of four-dimensional hypercube onto the physical 2D plane.

The S_{ij} represents the area of the parallelogram formed by the wave surfaces of $e^{i\boldsymbol{b}_i\cdot\boldsymbol{r}}$ and $e^{i\boldsymbol{b}_j\cdot\boldsymbol{r}}$, as shown in Fig. 4.1(b). For later convenience, we define the lattice vectors

$$\boldsymbol{a}_1^{ij} = \frac{S_{ij}}{2\pi}\,(\boldsymbol{b}_j \times \boldsymbol{e}_z),\ \boldsymbol{a}_2^{ij} = -\frac{S_{ij}}{2\pi}\,(\boldsymbol{b}_i \times \boldsymbol{e}_z), \tag{4.6}$$

where $\boldsymbol{e}_z$ donates the unit vector perpendicular to the 2D plane. The vector set $(\boldsymbol{a}_1^{ij}, \boldsymbol{a}_2^{ij})$ serves as the primitive lattice vectors corresponding to $(\boldsymbol{b}_1^{ij}, \boldsymbol{b}_2^{ij}) \equiv (\boldsymbol{b}_i, \boldsymbol{b}_j)$ in momentum space. It spans the unit cell $S_{ij} = (\boldsymbol{a}_1^{ij} \times \boldsymbol{a}_2^{ij})_z$ as illustrated in Fig. 4.1(b). The lattice vectors of the potential α and β are given by $\boldsymbol{a}_\mu^\alpha = \boldsymbol{a}_\mu^{12}$ and $\boldsymbol{a}_\mu^\beta = \boldsymbol{a}_\mu^{34}$, respectively.

4.1.2 Example: Twisted triangular potentials

In the previous chapter [32], we confirmed the validity of Eq. (3.21) in a double-moiré system consisting of graphene enclosed between hexagonal boron nitride layers. While considering the intrinsic 120° rotational symmetry, we discovered that it is unnecessary to consider a complete set of six independent integers. However, by introducing a slight deformation to break the symmetry, we can obtain six integers. In the subsequent sections, we will provide a comprehensive analysis of the six distinct integers within the framework of the double-period system described by Eq. (4.1) and involving a twisted double triangular potential. The twisted double triangular potential is defined as follows:

$$V^\lambda(\boldsymbol{r}) = 2V_0 \sum_{\mu=1}^{3} \cos[\boldsymbol{b}_\mu^\lambda \cdot (\boldsymbol{r} - \boldsymbol{r}_0^\lambda)]. \tag{4.7}$$

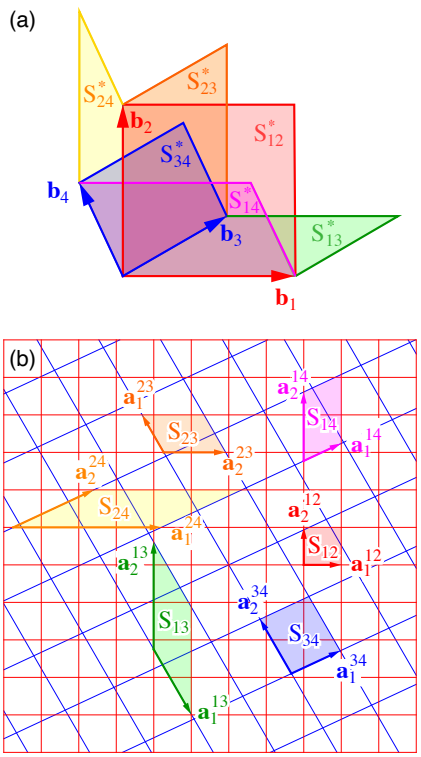

Figure 4.1: (a) Unit areas in momentum space, denoted by $S^*_{ij} = (\boldsymbol{b}_i \times \boldsymbol{b}_j)_z$. (b) Unit areas in real space, represented by S_{ij}, along with the corresponding lattice vectors $\boldsymbol{a}_1^{ij}$ and $\boldsymbol{a}_2^{ij}$. The grid lines in red (blue) depict the wave surfaces of $e^{i\boldsymbol{b}_1\cdot\boldsymbol{r}}$ and $e^{i\boldsymbol{b}_2\cdot\boldsymbol{r}}$ ($e^{i\boldsymbol{b}_3\cdot\boldsymbol{r}}$ and $e^{i\boldsymbol{b}_4\cdot\boldsymbol{r}}$).

Here, $\boldsymbol{r}_0^\lambda$ represents the origin of the potential for configuration λ. The reciprocal vectors for $\lambda = \alpha$ are given by:

$$\boldsymbol{b}_1^\alpha = \frac{2\pi}{a}\begin{pmatrix} 1 \\ -1/\sqrt{3} \end{pmatrix}, \quad \boldsymbol{b}_2^\alpha = \frac{2\pi}{a}\begin{pmatrix} 0 \\ 2/\sqrt{3} \end{pmatrix},$$
$$\boldsymbol{b}_3^\alpha = -\boldsymbol{b}_1^\alpha - \boldsymbol{b}_2^\alpha. \tag{4.8}$$

For $\lambda = \beta$, these vectors are defined as follows:

$$\boldsymbol{b}_\mu^\beta = R(\theta)\ \boldsymbol{b}_\mu^\alpha. \tag{4.9}$$

Here, $R(\theta)$ represents a 2D rotation matrix with an angle θ. The corresponding primitive lattice vectors are given by:

$$\boldsymbol{a}_1^\alpha = a\begin{pmatrix} 1 \\ 0 \end{pmatrix}, \quad \boldsymbol{a}_2^\alpha = a\begin{pmatrix} 1/2 \\ \sqrt{3}/2 \end{pmatrix},$$
$$\boldsymbol{a}_\mu^\beta = R(\theta)\ \boldsymbol{a}_\mu^\alpha. \tag{4.10}$$

Fig. 4.2 illustrates the potential profile for (a) a single potential, (b) a double potential with $\theta = 7°$ and (c) $\theta = 30°$. Throughout the following discussion, we will consider the potential amplitude, which remains identical in both α and β, as $V_0 = 0.213\varepsilon_0$, where $\varepsilon_0 = \hbar^2/(2ma^2)$.

In general, the potentials denoted as α and β lack a shared period, resulting in the absence of global translational symmetry within the system. In this analysis, we determine the energy spectrum using commensurate approximants. These approximants are derived by introducing slight deformations to the periodicity of either α or β, thereby creating a finite super unit cell with an area denoted as S_c. A series of commensurate approximants is prepared to mimic the continuous rotation of the twist angle between the two potentials. Subsequently, the energy bands and the density of states (DOS) are calculated for all systems. For each approximant, the DOS is averaged over the relative translation $\Delta\boldsymbol{r}_0 = \boldsymbol{r}_0^\alpha - \boldsymbol{r}_0^\beta$ to yield a continuous spectrum as a function of the twist angle.

Fig. 4.3(a) illustrates the density map of the density of states (DOS) as a function of θ and energy. In this representation, a brighter color corresponds to a larger DOS, while the dark blue region indicates the presence of a gap. This density map is similar to the plots shown in Fig. 3.4 and Fig. 3.5. The upper section of the figure displays an array of bars that represent the commensurate approximants considered in the calculation. On the other hand, Fig. 4.3(b) is a corresponding plot in which the vertical axis is converted to the electron density. In this plot, dots are used to indicate energy gaps, and the size of the dots reflects the width of the corresponding gap.

The zone quantum numbers ν_{ij} corresponding to each energy gap can be determined through the following procedure. In a commensurate approximant, the momentum space areas S^*_{ij} share a greatest common divisor $S^*_{\mathrm{c}} = (2\pi)^2/S_{\mathrm{c}}$ and can be expressed as $S^*_{ij} = s_{ij}S^*_{\mathrm{c}}$ where s_{ij} are integers. Additionally, the electron density below a given band gap is quantized as $n_e = [S^{\mathrm{c}}/(2\pi)^2]r$, where the integer r represents the number of occupied Bloch subbands. Consequently, Eq. (3.21) transforms into a Diophantine equation $r = \sum_{\langle i,j\rangle} \nu_{ij}s_{ij}$. By considering more than six commensurate approximants that share the same energy gap, we obtain a system of Diophantine equations, with the number of equations equal to the number of approximants. Through this process, we ultimately determine the integers ν_{ij} as a unique solution. It is important to note that the original double triangular potential, as described by Eq. (4.7), imposes constraints on the S^*_{ij} values, such as $S^*_{12} = S^*_{34}$ and $S^*_{13} = S^*_{24}$, due to its high spatial symmetry. These constraints hinder the complete identification of ν_{ij}. However, by including systems with slightly broken symmetry within the set of commensurate approximants, this issue is resolved.

At the bottom of Fig. 4.3, we present the zone quantum numbers (ν_{12}, ν_{13}, ν_{14}, ν_{23}, ν_{24}, ν_{34}) that have been identified for several significant gaps labeled in Fig. 4.3(a) and (b). In the low twist angle regime, the series M_n represents the

moiré gaps, which can be expressed as follows:

$$M_n = n(1, 0, -1, 1, 0, 1). \tag{4.11}$$

In this region, the system is governed by a long-range moiré pattern, as observed in Fig. 4.2(b). The discrete levels separated by M_n can be interpreted as the Bloch subbands of the moiré superlattice. The reciprocal lattice vectors for the moiré period are given by:

$$\boldsymbol{G}_1^{\mathrm{M}} = \boldsymbol{b}_1 - \boldsymbol{b}_3, \quad \boldsymbol{G}_2^{\mathrm{M}} = \boldsymbol{b}_2 - \boldsymbol{b}_4. \tag{4.12}$$

The area of the moiré Brillouin zone is determined by:

$$S_{\mathrm{M}}^* = (\boldsymbol{G}_1^{\mathrm{M}} \times \boldsymbol{G}_2^{\mathrm{M}})_z = S_{12}^* - S_{14}^* + S_{23}^* + S_{34}^*, \tag{4.13}$$

which corresponds to the values $(1, 0, -1, 1, 0, 1)$. Eq. (4.11) reveals that the momentum space area is quantized by S_{M}^*. In the large angle region ($\theta \gg 1°$), the system deviates from the long-wavelength picture, and a single periodicity is no longer sufficient to effectively describe it. At $\theta = 30°$, in particular, the system exhibits quasicrystalline behavior with 12-fold rotational symmetry [38, 39, 40, 37, 41, 42], as depicted in Fig. 4.2(c). It is observed that the zone quantum numbers consistently follow the form:

$$Q_{m,n} = (m, n, 2n, -n, n, m). \tag{4.14}$$

he corresponding electronic density, as given by Eq. (3.21), is expressed as $n_e = (\sqrt{3}m + 3n)/a^2$, indicating the existence of two distinct units, $\sqrt{3}/a^2$ and $3/a^2$, to quantify the electronic spectrum.

The constraint imposed on the zone quantum numbers, as given by Eq. (4.14), can be elucidated through the following explanation. By defining $\boldsymbol{b}'i$ $(i = 1, 2, 3, 4)$ as the 30° rotation of $\boldsymbol{b}_i$, we establish the relation $(\boldsymbol{b}'_1, \boldsymbol{b}'_2, \boldsymbol{b}'_3, \boldsymbol{b}'_4) = (\boldsymbol{b}_3, \boldsymbol{b}_4, \boldsymbol{b}_1 + \boldsymbol{b}_2, -\boldsymbol{b}_1)$. Consequently, the associated areas $S_{ij}^{*\prime} = (\boldsymbol{b}'_i \times \boldsymbol{b}'_j)_z$ can be expressed in terms of the original areas, such as $S_{12}^{*\prime} = S_{34}^*$, $S_{13}^{*\prime} = -S_{13}^* - S_{23}^*$, among

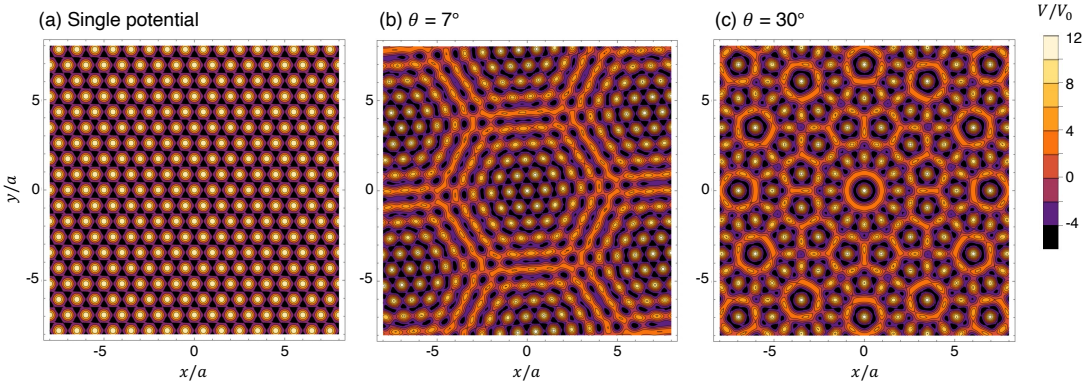

Figure 4.2: Contour plots illustrating: (a) a solitary triangular potential, (b) the configuration of twisted double triangular potentials at $\theta = 7°$, and (c) the case of $\theta = 30°$. [Refer to Eq. (4.7).]

others. When the system exhibits invariance under the 30° rotation, we expect the equation $\sum_{\langle i,j \rangle} \nu_{ij} S^*_{ij} = \sum_{\langle i,j \rangle} \nu_{ij} S^{*\prime}_{ij}$ to hold, with identical values of ν_{ij}. By utilizing the relationship between $S^{*\prime}_{ij}$ and S^*_{ij}, we derive constraints for ν_{ij}, ultimately leading to the emergence of Eq. (4.14). In Fig. 4.3, the other gaps are designated as $A, B, C, \ldots$. We observe that the zone quantum numbers for these gaps consistently follow the form of $(m, n, r, n-r, n, m)$. This behavior can be explained by the coexistence of the 120° rotational symmetry, which necessitates the form $(m, n, r, n-r, n, m')$, and the reflection symmetry with respect to the in-plane axis between $\boldsymbol{b}_1$ and $\boldsymbol{b}_3$, which requires $(m, n, r, n-r, n', m)$. The constraints imposed on the zone quantum numbers are verified through a similar reasoning as in the case of the 12-fold symmetry.

4.1.3 Quasi Brillouin zones

The quantity $\sum_{\langle i,j \rangle} \nu_{ij} S^*_{ij}$ corresponds to an area in momentum space known as the quasi Brillouin zone (qBZ). The boundary of the qBZ for a specific gap is defined as a collection of k-points on the original free-electron band where the gap begins to open in the limit of an infinitesimal potential [32]. Generally, the qBZ is a polygon composed of multiple segments corresponding to Bragg planes,

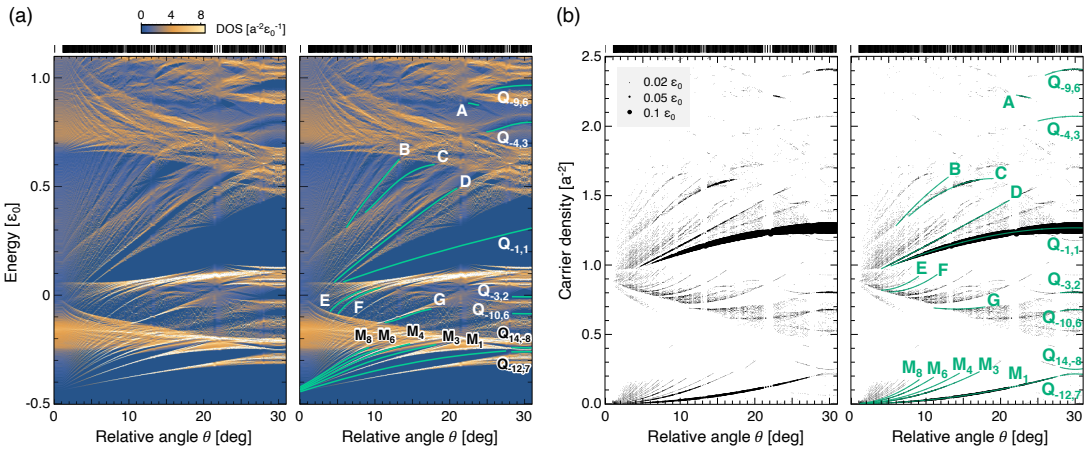

M_1 :(1,0,-1,1,0,1)	$Q_{-9,6}$:(-9,6,12,-6,6,-9)	$Q_{-10,6}$:(-10,6,12,-6,6,-10)	A:(-4,2,6,-4,2,-4)	E:(14,-1,-14,13,-1,14)
M_3 :(3,0,-3,3,0,3)	$Q_{-4,3}$:(-4,3,6,-3,3,-4)	$Q_{14,-8}$:(14,-8,-16,8,-8,14)	B:(-5,3,7,-4,3,-5)	F:(11,-1,-11,10,-1,11)
M_4 :(4,0,-4,4,0,4)	$Q_{-1,1}$:(-1,1,2,-1,1,-1)	$Q_{-12,7}$:(-12,7,14,-7,7,-12)	C:(-7,3,9,-6,3,-7)	G:(4,-1,-4,3,-1,4)
M_6 :(6,0,-6,6,0,6)	$Q_{-3,2}$:(-3,2,4,-2,2,-3)		D:(1,1,0,1,1,1)	
M_8 :(8,0,-8,8,0,8)				

Figure 4.3: (a) A density map illustrating the Density of States (DOS) as a function of θ and energy in twisted double triangular potentials. The right panel highlights and labels the major gaps. The upper section of the figures represents the array of bars representing the commensurate approximants employed in the calculation. (b) The corresponding plot with the vertical axis transformed to represent the electron density, where the size of the dots indicates the width of the respective gaps. The table at the bottom presents the zone quantum numbers $(\nu_{12}, \nu_{13}, \nu_{14}, \nu_{23}, \nu_{24}, \nu_{34})$ for the highlighted gaps.

which are the perpendicular bisectors of the composite reciprocal lattice vectors $\boldsymbol{G} = m_1\boldsymbol{b}_1 + m_2\boldsymbol{b}_2 + m_3\boldsymbol{b}_3 + m_4\boldsymbol{b}_4$. Let us consider the twisted triangular potential considered in the previous section. The qBZ for the moiré gap M_n is found to be the n-th Brillouin zone defined by the moiré reciprocal vectors $\boldsymbol{G}_1^{\mathrm{M}}$ and $\boldsymbol{G}_2^{\mathrm{M}}$ [Eq. (4.12)]. However, for general twist angles, the qBZ does not align with any Brillouin zone of a periodic system. In the leftmost panels of Fig. 4.4(a) and (b), we present the qBZs of the gaps $Q{-}1,1$ and $Q{-}3,2$, respectively, at $\theta = 30°$. The areas of these qBZs can be easily computed using the decomposition illustrated in the right two panels. For example, the area of the qBZ for the gap $Q_{-1,1}$ [Fig. 4.4(a)] is expressed as the sum of three squares, g_1, g_2, g_3, and two hexagons, h_1, h_2, given by $S^(Q_{-1,1}) = (g_1 + g_2 + g_3) - (h_1 + h_2)$. We have $g_1 = (\boldsymbol{b}_3 \times \boldsymbol{b}_2)_z = -S^*_{23}$, $g_2 = S^*_{14} + S^*_{24}$, $g_3 = S^*_{13} + S^*_{14}$, $h_1 = S^*_{12}$, and $h_2 = S^*_{34}$. Consequently, we obtain $S^*(Q_{-1,1}) = -S^*_{12} + S^*_{13} + 2S^*_{14} - S^*_{23} + S^*_{24} - S^*_{34}$, which agrees with the zone quantum numbers $(-1, 1, 2, -1, 1, -1)$ obtained in the previous section.

Similarly, the area of the quasi Brillouin zone (qBZ) for the gap $Q_{-3,2}$ can be expressed as $S^*(Q_{-3,2}) = p_1 + p_2 + p_3 - 2q_1 - q_2$, as depicted in Fig. 4.4(b). Here, p_1 corresponds to the Wigner-Seitz cell in the reciprocal lattice spanned by $\boldsymbol{b}_1$ and $\boldsymbol{b}_3$, thus $p_1 = S^*_{13}$. The quantities q_1 (hexagon) and q_2 (six triangles) represent the first and second Brillouin zones defined by the primitive vectors $\boldsymbol{b}_1 - \boldsymbol{b}_3$ and $\boldsymbol{b}_2 - \boldsymbol{b}_4$. Consequently, we have $q_1 = q_2 = [(\boldsymbol{b}_1 - \boldsymbol{b}_3) \times (\boldsymbol{b}_2 - \boldsymbol{b}_4)]_z = S^*_{12} + S^*_{34} - S^*_{14} + S^*_{23}$. Hence, the area $S^*(Q{-}3,2)$ yields the zone quantum numbers $(-3, 2, 4, -2, 2, -3)$.

At a twist angle of 30°, symmetry constraints such as $g_1 = g_2 = g_3$ are satisfied, and one might perceive that the decomposition of the qBZ area into S^*_{ij}'s is not unique. However, the area quantization with the same ν_{ij} remains strictly valid when the potential is perturbed to break the symmetry. This guarantees the uniqueness of the decomposition.

Fig. 17 showcases the qBZs of (a) $Q_{-1,1}$ and (b) $Q_{-3,2}$ in the twisted triangular potential with $\theta = 30°$. The right two panels in each row illustrate the

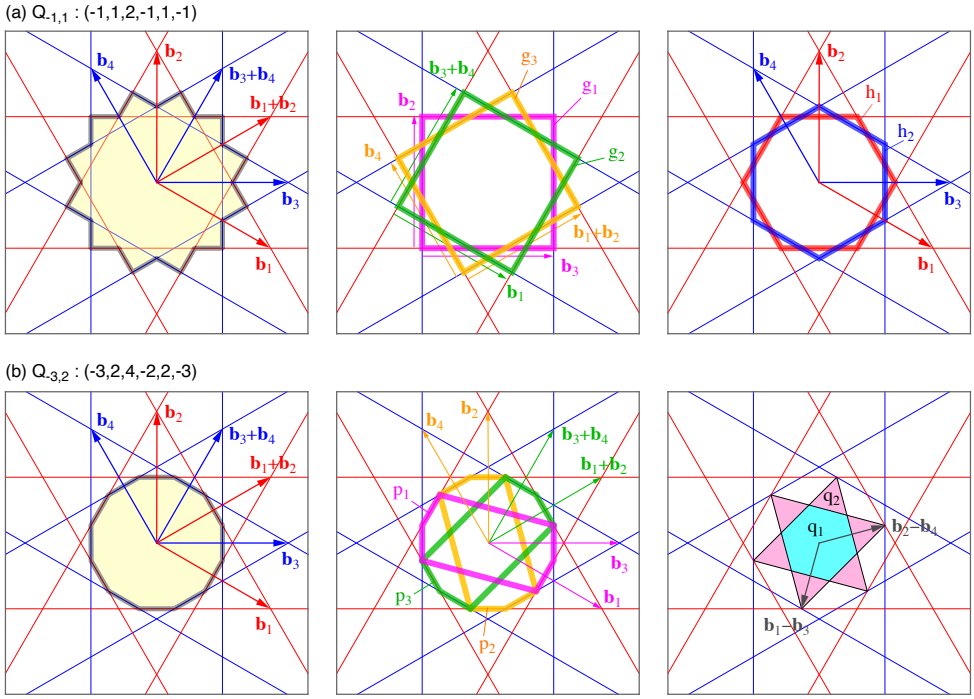

Figure 4.4: the qBZs of (a) $Q_{-1,1}$ and (b) $Q_{-3,2}$ in the twisted triangular potential with $\theta = 30°$. The right two panels in each row illustrate the decomposition of the qBZ into the primitive Brillouin zones.

decomposition of the qBZ into the primitive Brillouin zones.

At 30°, we have the symmetry constraints such as $g_1 = g_2 = g_3$ and one might think the decomposition of the qBZ area into S^*_{ij}'s is not unique. However, the area quantization with the same ν_{ij} strictly holds when the potential is deformed to break the symmetry, and this guarantees a uniqueness of the decomposition.

By using the serial notation Eq. (3.6), Eq. (3.9) can simply be written as

$$\boldsymbol{b}_i = p_i \boldsymbol{b}^{\mathrm{c}}_1 + q_i \boldsymbol{b}^{\mathrm{c}}_2. \tag{4.15}$$

Accordingly, the unit areas Eq. (4.5) become

$$S^*_{ij} = (p_i q_j - p_j q_i) S^*_{\mathrm{c}}, \tag{4.16}$$

where $S^*_{\mathrm{c}} = (\boldsymbol{b}^{\mathrm{c}}_1 \times \boldsymbol{b}^{\mathrm{c}}_2)_z = (2\pi)^2/S_{\mathrm{c}}$ is the area of the first Brillouin zone of the

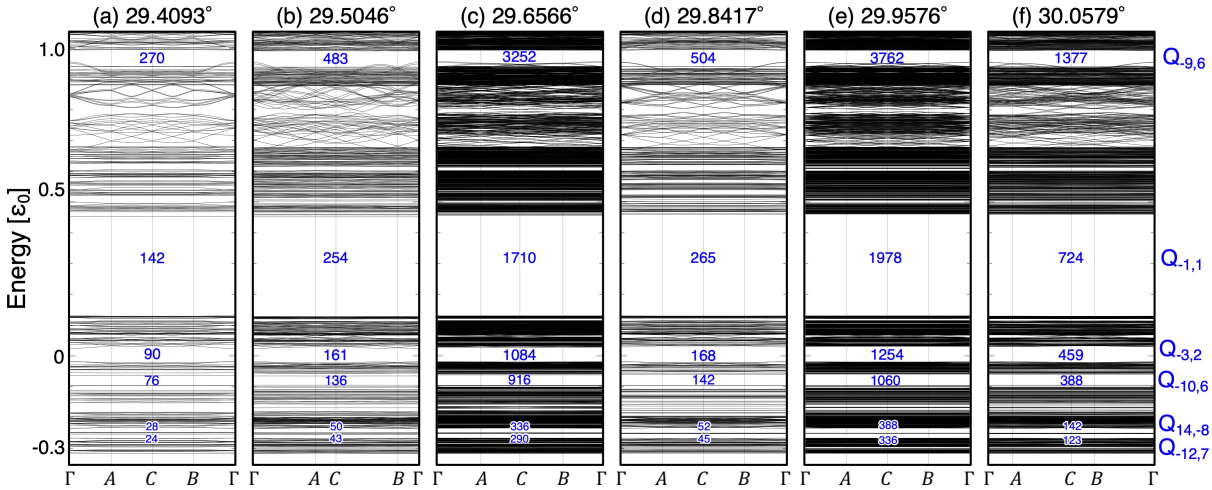

Figure 4.5: Band structures of commensurate approximants (a) to (f) (specified in Table 4.1) for the twisted double triangular potential in the vicinity of approximately 30 degrees. The path followed in the Brillouin zone is denoted as $(\Gamma, A, C, B, \Gamma) \equiv (0, \boldsymbol{b}_1^{\mathrm{c}}/2, (\boldsymbol{b}_1^{\mathrm{c}} + \boldsymbol{b}_2^{\mathrm{c}})/2, \boldsymbol{b}_2^{\mathrm{c}}/2, 0)$. Within the gaps, the integers indicate the number of bands located below each respective gap, denoted as r.

	(a)	(b)	(c)	(d)	(e)	(f)
θ	29.4093	29.5046	29.6566	29.8417	29.9576	30.0579
p_1	3	3	25	11	11	11
p_2	8	8	9	4	30	30
p_3	8	8	34	15	30	30
p_4	3	3	-9	-4	11	11
q_1	-8	-9	-27	-4	-30	-11
q_2	11	34	37	15	41	15
q_3	-3	9	-10	4	-11	-4
q_4	11	25	37	11	41	15
$r[Q_{-9,6}]$	270	483	3252	504	3762	1377
$r[Q_{-1,1}]$	142	254	1710	265	1978	724
$r[Q_{-3,2}]$	90	161	1084	168	1254	459
$r[Q_{-10,6}]$	76	136	916	142	1060	388
$r[Q_{14,-8}]$	28	50	336	52	388	142
$r[Q_{-12,7}]$	24	43	290	45	336	123

Table 4.1: Twist angle θ and the indeces $(p_1, p_2, p_3, p_4; q_1, q_2, q_3, q_4)$ of the commensurate approximants (a) to (f). The $r[Q_{m,n}]$ is the number of the occupied bands below the gap $Q_{m,n}$.

commensurate approximant. Eq. (3.21) becomes the Diophantine equation,

$$r = \sum_{\langle i,j \rangle} \nu_{ij}(p_i q_j - p_j q_i), \tag{4.17}$$

where $r \equiv n_e/[S_{\mathrm{c}}^*/(2\pi)^2]$ is for the number of the bands below the gap.

In determination of the zone quantum numbers ν_{ij}, we consider a series of commensurate approximants near the target system, and solve a set of Diophantine equations Eq. (4.17) for all the approximants. As an example, we show in Fig. 4.5 the band structures of six commensurate approximants (a) to (f) for the double triangular potential near $\theta = 30°$ [see, Fig. 4.3], which are specified by $(p_1, p_2, p_3, p_4; q_1, q_2, q_3, q_4)$ in Table 4.1. The Brillouin zone path is taken as $(\Gamma, A, C, B, \Gamma) \equiv (0, \boldsymbol{b}_1^{\mathrm{c}}/2, (\boldsymbol{b}_1^{\mathrm{c}} + \boldsymbol{b}_2^{\mathrm{c}})/2, \boldsymbol{b}_2^{\mathrm{c}}/2, 0)$. Table 4.1 also shows the number of the occupied bands r for some major gaps $Q_{m,n}$. The six systems have very close potential profiles and similar spectral structures, while it have completely different sizes of the commensurate unit cells and thus different numbers of bands below the same gap. For the largest gap $Q_{-1,1}$, for instance, the number of the bands are $r = 142, 254, 1710, 265, 1978, 724$ for the six systems, and accordingly we have six independent equations of Eq. (4.17) with six unknown variables ν_{ij}. By solving the set of the equations, we find $\nu_{ij} = (-1, 1, 2, -1, 1, -1)$ as a unique solution. All other approximants sharing the same gap have the same solution of ν_{ij}.

4.2 Adiabatic charge pumping

In this section, we demonstrate that the zone quantum numbers, as introduced in the preceding section, serve as descriptors for the adiabatic charge pumping occurring during the relative sliding of the doubly periodic potential.

4.2.1 1D systems

Initially, we examine a one-dimensional doubly periodic Hamiltonian given by

$$H = \frac{p^2}{2m} + V_1(x) + V_2(x), \tag{4.18}$$

where $V_i(x) = \sum_m V_{i,m}, e^{imb_i x}$ (with $i = 1, 2$) represents a periodic potential characterized by a period of $a_i = 2\pi/b_i$.

where $V_i(x) = \sum_m V_{i,m}\, e^{imb_i x} (i = 1, 2)$ is a periodic potential with the period of $a_i = 2\pi/b_i$. Now, let us contemplate a cyclic process wherein one of the periodic potentials, denoted as $V_i(x)$, undergoes an adiabatic translation over the span of its period a_i, while the other remains fixed. This translated potential is elegantly expressed as follows:

$$V_i\Big(x - \frac{\phi_i}{2\pi} a_i\Big) = \sum_m V_{i,m}\, e^{im(b_i x - \phi_i)}, \tag{4.19}$$

In this context, an incremental increase in ϕ_i from 0 to 2π corresponds to a unitary translation of $V_i(x)$ spanning a distance of a_i.

We establish ΔP_i as the variation in electric polarization ensuing from a unitary translation. In one spatial dimension (1D), ΔP_i assumes the dimension of electronic density, defined as the quantity of electrons per unit length, multiplied by length, rendering it dimensionless. It is imperative to observe that our definition of polarization excludes the contribution of the electric charge, represented by $-e$. In this context, we posit the following proposition: In instances where the Fermi energy resides within a band gap, the alteration in polarization per cycle, denoted as ΔP_i, and the electron density situated beneath the energy gap, denoted as n_e, exhibit the following relationship:

$$\Delta P_i = 2\pi \frac{\partial n_e}{\partial b_i}. \tag{4.20}$$

Eq. (4.20) can be established through the following contemplation. Let us engage in an adiabatic process wherein the wavenumber b_i undergoes a slight modification to $b_i + \delta b_i$. As elucidated in Fig. 4.6, the corresponding alteration of

$V_i(x)$ at a point situated at a considerable distance from the origin ($|x| \gg a_i$) can be conceived as a parallel translation of the unchanging potential $V_i(x)$. Taking into account the phase factor $b_i x - \phi_i$ in Eq. (4.19), the transition from b_i to $b_i + \delta b_i$ can be encompassed by an adjustment of ϕ_i denoted as $\delta\phi_i = -\delta b_i, x$. This adjustment engenders a phase shift in the effective translation at point x. Since this procedure corresponds to $n = \delta\phi_i/(2\pi)$ cycles of a unitary translation, the quantity of electrons traversing through the point x is expressed as $n\Delta P_i = -\Delta P_i \delta b_i, x/(2\pi)$. In light of the uninterrupted flow of electric charge, this must be in harmony with the shift in the number of electrons within the region spanning from 0 to x. This begets the equation $-\Delta P_i \delta b_i, x/(2\pi) = -x\delta n_e$, culminating in the derivation of Eq. (4.20).

In the doubly-periodic system, as defined by Eq. (4.18), each spectral gap exhibits distinctive characteristics denoted by a pair of integers, m_1 and m_2. These integers determine the electron density beneath the gap, as expressed in the following equation:

$$n_e = \frac{1}{2\pi}(m_1 b_1 + m_2 b_2) = \frac{m_1}{a_1} + \frac{m_2}{a_2}, \tag{4.21}$$

Utilizing Eq. (4.20), we deduce $\Delta P_i = m_i$, signifying that m_i electrons traverse any given cross-section of the system. It is noteworthy that these integers, m_1 and m_2, correspond precisely to the first Chern numbers [97, 98, 88, 84].

4.2.2 2D systems

The same rationale applies to a doubly-periodic two-dimensional Hamiltonian, as delineated in Eq. (4.1). We deliberate upon an adiabatic translation of the periodic potential V^λ ($\lambda = \alpha$ or β), as specified in Eq. (4.2), by $\boldsymbol{a}_\mu^\lambda$. Our objective is to quantify the alteration in electric polarization throughout this procedure.

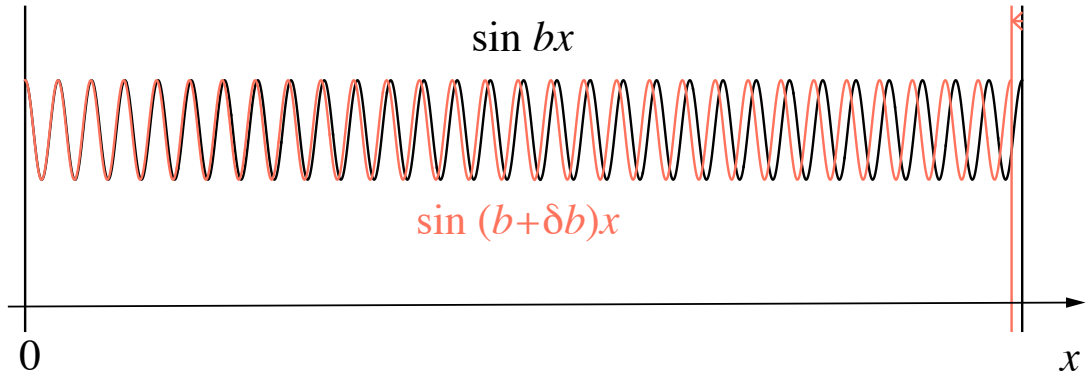

Figure 4.6: Schamatic picture of an adiabatic process slightly changing the wavenumber of a 1D periodic potential. At a point far from the origin ($|x| \gg 2\pi/b$), the change can be viewed as a parallel translation of the potential.

The parallel translation of $V^\lambda(\boldsymbol{r})$ is articulated as follows:

$$\begin{aligned} &V^\lambda\Big(\boldsymbol{r} - \frac{\phi_1^\lambda}{2\pi}\boldsymbol{a}_1^\lambda - \frac{\phi_2^\lambda}{2\pi}\boldsymbol{a}_2^\lambda\Big) \\ &= \sum_{m_1,m_2} V^\lambda_{m_1,m_2}\, e^{im_1(\boldsymbol{b}_1^\lambda\cdot\boldsymbol{r}-\phi_1^\lambda)+im_2(\boldsymbol{b}_2^\lambda\cdot\boldsymbol{r}-\phi_2^\lambda)} \end{aligned} \tag{4.22}$$

where we used $\boldsymbol{a}_\mu^\lambda \cdot \boldsymbol{b}_\nu^\lambda = 2\pi\delta_{\mu\nu}$. An increase of ϕ_μ^λ from 0 to 2π gives a unit translation of the potential V^λ by $\boldsymbol{a}_\mu^\lambda$.

The situation can be systematically described by a generalized Hamitonian $H = \boldsymbol{p}^2/(2m) + V$ with

$$\begin{aligned} &V(\boldsymbol{r};\phi_1,\ldots,\phi_N) = \\ &\qquad \sum_{m_1,\ldots,m_N} V_{m_1,\cdots m_N}\, e^{i\sum_{i=1}^N m_i(\boldsymbol{b}_i\cdot\boldsymbol{r}-\phi_i)}. \end{aligned} \tag{4.23}$$

The current double-period system corresponds to $N = 4$, where $\boldsymbol{b}_1,\ldots,\boldsymbol{b}_4$ are given by Eq. (3.6), and

$$(\phi_1,\phi_2,\phi_3,\phi_4) = (\phi_1^\alpha,\phi_2^\alpha,\phi_1^\beta,\phi_2^\beta). \tag{4.24}$$

We contemplate a cyclic procedure in which the parameter ϕ_i corresponding to a specific index i undergoes an adiabatic augmentation from 0 to 2π. When the Fermi energy resides within a band gap, we can demonstrate that the alteration

in electric polarization throughout this process is encapsulated by the equation:

$$\Delta \boldsymbol{P}_i = 2\pi \frac{\partial n_e}{\partial \boldsymbol{b}_i}, \tag{4.25}$$

This equation represents the two-dimensional analogue of Eq. (4.20). Now, it is pertinent to note that $\Delta \boldsymbol{P}_i$ assumes the dimension of electronic density (defined as the number of electrons per unit area) multiplied by length.

Eq. (4.25) is derived as follows. Let us contemplate the modification of the potential $V(\boldsymbol{r})$ when $\boldsymbol{b}_i$ is transformed into $\boldsymbol{b}_i + \delta \boldsymbol{b}_i$. In a manner akin to the one-dimensional scenario, the alteration at a point distanced significantly from the origin ($|\boldsymbol{r}| \gg 2\pi/|\boldsymbol{b}_i|$) is analogous to a parallel translation, denoted as $\delta\phi_i = -\delta \boldsymbol{b}_i \cdot \boldsymbol{r}$. It is crucial to recognize the presence of the phase factor $\boldsymbol{b}_i \cdot \boldsymbol{r} - \phi_i$ in Eq. (4.23). This induces a change in polarization at the point $\boldsymbol{r}$ given by $\Delta \boldsymbol{P}_i \delta\phi_i/(2\pi) = \Delta \boldsymbol{P}_i(-\delta \boldsymbol{b}_i \cdot \boldsymbol{r})/(2\pi)$. The quantity of electrons traversing a line segment from $\boldsymbol{r}$ to $\boldsymbol{r} + d\boldsymbol{r}$ is expressed as:

$$dN_e = [(d\boldsymbol{r} \times \boldsymbol{e}_z) \cdot \Delta \boldsymbol{P}_i](\delta \boldsymbol{b}_i \cdot \boldsymbol{r})/(2\pi). \tag{4.26}$$

Now, we contemplate a substantial closed trajectory denoted as C situated within the two-dimensional plane. Let N_e represent the count of electrons encompassed by C. Upon altering $\boldsymbol{b}_i$ to $\boldsymbol{b}_i + \delta \boldsymbol{b}_i$, we assess the modification in N_e by conducting an integration of Eq. (4.26) along the trajectory. This yields:

$$\begin{aligned} \delta N_e = \oint_C dN_e &= \frac{1}{2\pi} \oint_C [(d\boldsymbol{r} \times \boldsymbol{e}_z) \cdot \Delta \boldsymbol{P}_i](\delta \boldsymbol{b}_i \cdot \boldsymbol{r}) \\ &= \frac{S}{2\pi} \Delta \boldsymbol{P}_i \cdot \delta \boldsymbol{b}_i \end{aligned} \tag{4.27}$$

Wherein, S represents the expanse delineated by the confines of C, and we employ the correlation $\oint_C (d\boldsymbol{r} \times \boldsymbol{e}_z)\mu r_\nu = S\delta_{\mu\nu}$ in the two-dimensional realm.

As a consequence, given that $n_e = N_e/S$, we ultimately arrive at Eq. (4.25).

In a two-dimensional doubly-periodic configuration, the electron density beneath an energy gap undergoes quantization, a principle rigorously established in the preceding section. Employing Equation (4.25) in conjunction with Equation

(3.21), we can explicitly compute the charge pumping, denoted as $\Delta \boldsymbol{P}_i$. This calculation yields:

$$\begin{aligned}\Delta \boldsymbol{P}_i &= \frac{1}{2\pi}\sum_{\langle k,j\rangle}\nu_{kj}\frac{\partial S^*_{kj}}{\partial \boldsymbol{b}_i} \\ &= \frac{1}{2\pi}\sum_{j}\nu_{ij}(\boldsymbol{b}_j\times\boldsymbol{e}_z),\end{aligned} \tag{4.28}$$

It is noteworthy that we have employed the relationship $S^*_{ij} = (\boldsymbol{b}_i \times \boldsymbol{b}_j)\cdot \boldsymbol{e}_z = (\boldsymbol{b}_j \times \boldsymbol{e}_z)\cdot \boldsymbol{b}_i$ in this derivation.

By making use of the real space lattice vectors as expressed in Eq. (4.6), we can reformulate Eq. (4.28) as follows:

$$\Delta \boldsymbol{P}_i = \sum_j \frac{\nu_{ij}}{S_{ij}}\boldsymbol{a}_1^{ij}. \tag{4.29}$$

The physical interpretation of Equation (4.29) unfolds as follows: Equation (3.21) conveys that within each unit area S_{ij}, ν_{ij} electrons find their abode. When, for example, ϕ_1 undergoes a transition from 0 to 2π (i.e., the movement of V^α by $\boldsymbol{a}_1^\alpha$), the wavefront associated with $\boldsymbol{b}_1$ shifts by a single period. This translates to displacements in the unit areas S_{12}, S_{13}, S_{14} by $\boldsymbol{a}_1^{12}, \boldsymbol{a}_1^{13}, \boldsymbol{a}_1^{14}$ correspondingly [Refer to Fig. 4.1 (b)]. For each $j = 2, 3, 4$, the electron density of ν_{1j}/S_{1j} relocates by $\boldsymbol{a}_1^{1j}$, culminating in a modification in polarization described by $\Delta \boldsymbol{P}_1 = \sum_{j=2,3,4}(\nu_{1j}/S_{1j})\boldsymbol{a}_1^{1j}$.

4.3 4D quantum Hall effect and the second Chern numbers

In the subsequent discussion, we elucidate the concept of adiabatic pumping, previously expounded upon in an alternative fashion, employing the dimensional reduction technique associated with the four-dimensional (4D) quantum Hall effect (QHE) [79, 108, 75, 109, 110, 111, 112]. We shall establish that the zone quantum number ν_{ij} precisely corresponds to the second Chern number.

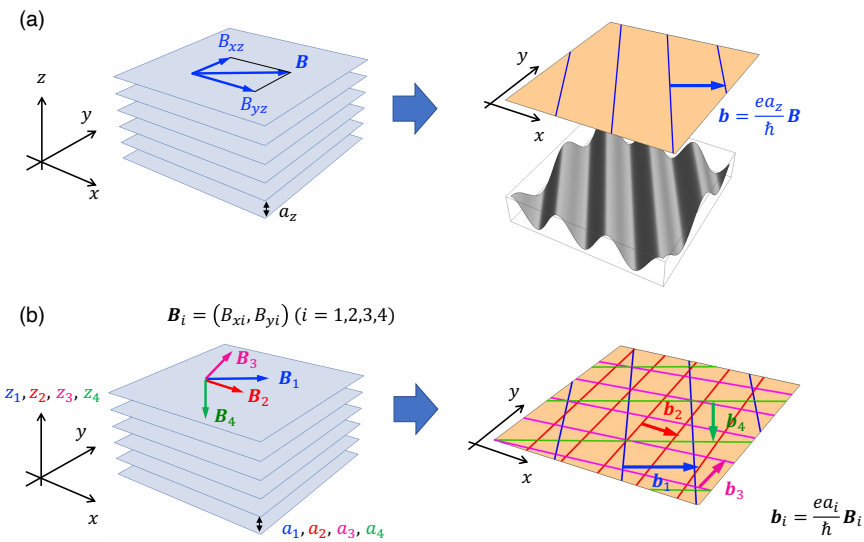

Figure 4.7: (a) Right: Three-dimensional stack of 2D free-electron systems under in-plane magnetic field. Note that the vector $\boldsymbol{B}$ is given by $\boldsymbol{B} = (B_{yz}, B_{xz}) = (B_x, -B_y)$, which is not the natural expression of the magnetic field (B_x, B_y). Left: the corresponding 2D system after the dimensional reduction (see the text). The wavevector $\boldsymbol{b}$ of the sinusoidal wave is proportional to $\boldsymbol{B}$ in the left panel. (b) Six-dimensional stack of 2D free-electron systems under in-plane magnetic field (right) and the corresponding 2D system with four sinusoidal potentials (left).

To illustrate this concept, we begin with the three-dimensional Quantum Hall Effect (QHE) as a straightforward example. Imagine an unbounded stack of two-dimensional free-electron systems, as depicted in Fig. 4.7(a). These systems are continuous in the x and y dimensions while discrete in the z direction, featuring a lattice spacing of a_z. In the context of the z dimension, we assume nearest-neighbor tight-binding interactions denoted as t_z between adjacent layers. We subject this system to a magnetic field characterized by $B_{\mu\nu} = \partial_\mu A_\nu - \partial_\nu A_\mu$. Specifically, we consider a uniform, in-plane magnetic field denoted as $(B_{yz}, B_{zx}, 0)$. The vector potential $\boldsymbol{A}$ is expressed as $\boldsymbol{A} = (0, 0, A_z)$, where $A_z = B_{xz}x + B_{yz}y$ (it's important to note that $B_{xz} = -B_{zx}$). The dynamics of an electron are governed by the Schrödinger equation:

$$\frac{\boldsymbol{p}^2}{2m}\Psi(x,y,z) - t_z\Big[e^{i\frac{e}{\hbar}A_z a_z}\Psi(x,y,z+a_z) + e^{-i\frac{e}{\hbar}A_z a_z}\Psi(x,y,z-a_z)\Big] = E\Psi(x,y,z), \tag{4.30}$$

Wherein, we have $\boldsymbol{p} = -i\hbar(\partial_x, \partial_y)$, representing the in-plane momentum. As the Hamiltonian exhibits periodicity in the z dimension, we can factorize the wavefunction as $\Psi(x,y,z) = \psi(x,y)e^{ik_z z}$. Consequently, Equation (4.30) simplifies into a two-dimensional Schrödinger equation:

$$\frac{\boldsymbol{p}^2}{2m}\psi - 2t_z\cos(\boldsymbol{b}\cdot\boldsymbol{x} + \phi_z)\psi = E\psi, \tag{4.31}$$

Here, $\boldsymbol{b} = (ea_z/\hbar)(B_{xz}, B_{yz})$, $\boldsymbol{x} = (x, y)$, and $\phi_z = k_z a_z$. The system now operates in two dimensions, featuring a solitary sinusoidal potential with wave number $\boldsymbol{b}$. Notably, the phase factor ϕ_z corresponds to the wavenumber in the z direction.

Expanding into higher dimensions presents a straightforward progression. We delve into the realm of a six-dimensional (6D) system, spanning $(x, y, z_1, z_2, z_3, z_4)$ space. This configuration maintains continuity along the x and y axes while embracing discreteness along the $z_i, (i = 1, 2, 3, 4)$ dimensions. Within this intricate framework, we introduce a uniform magnetic field, with B_{yi} encompassing the yz_i-plane and B_{ix} $(= -B_{xi})$ permeating the $z_i x$-plane. To describe this, we formulate the vector potential $\boldsymbol{A} = \sum_{i=1}^{4}(B_{xi}x + B_{yi}y)\boldsymbol{e}_i$, where $\boldsymbol{e}_i$ signifies the unit

vector aligned with the z_i direction. Fig. 4.7(b) provides a schematic representation of this system. Given the Hamiltonian's periodicity with respect to each z_i, we express the wavefunction as $\Psi(x, y, z_1, z_2, z_3, z_4) = \psi(x, y)e^{i\sum_i k_i z_i}$, where k_i denotes the Bloch wavenumber defined within the range $\pi/a_i < k_i \leq \pi/a_i$. The 6D Schrödinger equation is reduced to (x, y) space as

$$\frac{\boldsymbol{p}^2}{2m}\psi - \sum_{i=1}^{4} 2t_i \cos(\boldsymbol{b}_i \cdot \boldsymbol{x} + \phi_i)\psi = E\psi, \tag{4.32}$$

where

$$\boldsymbol{b}_i = \frac{ea_i}{\hbar}(B_{xi}, B_{yi}), \quad \phi_i = k_i a_i. \tag{4.33}$$

This is tantamount to the 2D double-periodic system under investigation in this paper. The inclusion of higher harmonic terms within $\boldsymbol{b}_i$ can be achieved by postulating additional layer hopping in the z_i direction.

The electromagnetic response of the system is characterized by the second Chern number [79, 108, 75, 109, 110, 111, 112]. Let us now turn our attention to a commensurate approximant, wherein the periodicities of $\boldsymbol{b}_i (i = 1, 2, 3, 4)$ converge into a common super unit cell. Here, we introduce the definition of the Bloch wavenumber (k_x, k_y) within the corresponding super Brillouin zone. The Bloch Hamiltonian governing the 6D system is expressed as $H(k_x, k_y, k_1, k_2, k_3, k_4)$. Within this context, we delve into the 4D subspace $k_\mu = (k_x, k_y, k_i, k_j)$ by selecting two indices i, j from the set 1,2,3,4, while keeping the remaining two wavenumbers fixed. When the spectrum of 4D Hamiltonian $H(k_x, k_y, k_i, k_j)$ is gapped, the second Chern number for the gap is defined as [79, 108, 75, 109, 110, 111, 112],

$$C_{ij}^{(2)} = \frac{1}{32\pi^2}\int_{\mathrm{BZ}} d^4k\, \epsilon^{\mu\nu\lambda\rho}\mathrm{Tr}[\mathcal{F}_{\mu\nu}\mathcal{F}_{\lambda\rho}] \ \in \mathbb{Z}. \tag{4.34}$$

Here BZ stands for the 4D Brillouin zone (a 4D torus), $\epsilon^{\mu\nu\lambda\rho}$ is the antisymmetric tensor of rank 4 and $\mathcal{F}_{\mu\nu}$ is a matrix defined by

$$\begin{aligned} \mathcal{F}_{\mu\nu}^{\alpha\beta} &= \partial_\mu \mathcal{A}_\nu^{\alpha\beta} - \partial_\nu \mathcal{A}_\mu^{\alpha\beta} + i[\mathcal{A}_\mu, \mathcal{A}_\nu]^{\alpha\beta}, \\ \mathcal{A}_\mu^{\alpha\beta}(\boldsymbol{k}) &= -i\langle\alpha, \boldsymbol{k}|\partial_\mu|\beta, \boldsymbol{k}\rangle, \end{aligned} \tag{4.35}$$

where $\partial_\mu = \partial/\partial k_\mu$, $|\alpha, \boldsymbol{k}\rangle$ is the eigenstates of the α-th band, and the indeces α and β run over all the bands below the gap. It is alternatively expressed as [79]

$$C_{ij}^{(2)} = -\frac{1}{8\pi^2}\int_{\mathrm{BZ}} d^4k\, \epsilon^{\mu\nu\lambda\rho}\mathrm{Tr}\Big[P\frac{\partial P}{\partial k_\mu}\frac{\partial P}{\partial k_\nu}P\frac{\partial P}{\partial k_\lambda}\frac{\partial P}{\partial k_\rho}\Big] \tag{4.36}$$

where $P(\boldsymbol{k}) = \sum_{\alpha\in\mathrm{occ}}|\alpha, \boldsymbol{k}\rangle\langle\alpha, \boldsymbol{k}|$ is the projection operator to the eigenstates below the gap. Note that we have six second Chern numbers depending on the choice of $i, j (i \neq j)$ from 1,2,3,4.

When the Fermi energy is in the gap, the electro-magnetic response of the 4D system is given by [79, 108, 75, 109, 110, 111, 112]

$$j_\mu^{(4\mathrm{D})} = \frac{e^3}{h^2}C_{ij}^{(2)}\epsilon^{\mu\nu\lambda\rho}B_{\nu\lambda}E_\rho, \tag{4.37}$$

Here, $j_\mu^{(4\mathrm{D})}$ represents the electric current density within the 4D space. Upon the application of a weak electric field E_i to the system, the wavenumber k_i adiabatically evolves to $k_i + (e/\hbar)A_i(t)$, where $E_i = -\partial A_i/\partial t$. In the context of a cyclic process, where $\phi_i = k_i a_i$ undergoes a transition from 0 to 2π within a time period T, the corresponding electric field is given by:

$$E_i = -\frac{h}{ea_i}\frac{1}{T}. \tag{4.38}$$

In accordance with Eq. (4.37), the electric field E_i elicits an electrical current $(j_x, j_y)^{(4\mathrm{D})} = (e^3/h^2)C_{ij}^{(2)}(-B_{yj}, B_{xj})E_i$. The corresponding two-dimensional current density per a singular stratum is expressed as $j_\mu^{(2\mathrm{D})} = j_\mu^{(4\mathrm{D})}a_i a_j$, resulting in

$$(j_x, j_y)^{(2\mathrm{D})} = -\frac{e}{2\pi}C_{ij}^{(2)}(b_{j,y}, -b_{j,x})\frac{1}{T}, \tag{4.39}$$

utilizing Eqs. (4.33) and (4.38). The complete alteration in polarization throughout the progression ($\phi_i : 0 \to 2\pi$) is denoted as $\Delta\boldsymbol{P}_i = \boldsymbol{j}^{(2\mathrm{D})}T/(-e)$. Through the addition of the summation over index j, we ultimately derive

$$\Delta\boldsymbol{P}_i = -\frac{1}{2\pi}\sum_j C_{ij}^{(2)}(\boldsymbol{b}_j \times \boldsymbol{e}_z). \tag{4.40}$$

It is evident that Eq. (4.40) precisely mirrors the structure of Eq. (4.28). Upon juxtaposing the two equations, we promptly deduce

$$\nu_{ij} = -C_{ij}^{(2)}, \tag{4.41}$$

signifying that the zone quantum numbers coincide with the second Chern numbers.

By employing Eq. (4.36), we conducted a numerical evaluation of $C_{ij}^{(2)}$ for select commensurate approximants within the context of the twisted triangular potential series expounded in Section 4.1.2. This analysis conclusively corroborated the concordance with $-\nu_{ij}$.

Inasmuch as Eq. (4.36) encompasses the integration over the Brillouin zone of the commensurate approximant, one might surmise that $C_{ij}^{(2)}$ explicitly hinges on the Brillouin zone dimensions (inversely related to the commensurate unit cell dimensions), a parameter that ostensibly lacks intrinsic significance. However, in actuality, the integrand $\mathrm{Tr}[\cdots]$ itself exhibits proportionality to the count of subbands residing beneath the energy gap (commensurate with the unit cell dimensions). This proportionality effectively annuls the contribution of the Brillouin zone integral, bestowing upon us invariant integers, which remain unaffected by the commensurate period.

Chapter 5

Conclusion

In this thesis, we present comprehensive studies on the energy spectrum and and topological gap labeling in quasi-periodic double moiré systems.

In Chapter 3, we consider the electronic band structure of hBN/graphene/hBN trilayer system, as a representative example of the double moiré systems We calculated the energy spectrum as a function of the two twist angles, by employing the effective continuum Hamiltonian method. We discovered that the energy spectrum exhibits a fractal pattern akin to the Hofstadter's butterfly, where an intricate mini-gap structure continuously changes with the twist angle.

An important observation is that each mini-gap are characterized by a unique set of six integers, which are associated with six Brillouin zones arising from the redundant periodicities. More specifically, the electron density below any single gap in the spectrum can be written as an integer linear combination of the six Brillouin zone areas with the six integer coefficients. For each gap, the six integers remain invariant upon a continuous change of the twist angles, regardless of the commensurability of the double moiré pattern. We also found that the associated momentum-space area given by the six integers corresponds to a certain geometric shape which we referred to as the quasi Brillouin zone. Its snow-flake like structure is defined by multiple Bragg planes, and it can be uniquely identified by the spectral distribution in the zero potential limit.

In Chapter 4, we explore the topological origin of the gap-labeling integers in 2D quasi periodic systems. First, we demonstrated that fractal energy spectrum as in hBN/graphene/hBN trilayer can also be seen in mre general doubly-periodic systems, which are described by a continuum Hamiltonian with a pair of periodic potentials. There the gaps can be characterized by six integers as well. Subsequently, we considered an adiabatic charge pumping induced by the relative sliding of the periodic potentials, and found that the pumped charge when the Fermi energy is in a certain gap is expressed by the six gap-labeling integers for the gap. Finally, we demonstrated a formal mapping between the adiabatic charge pumping and 4D quantum Hall effect, and found that six gap-labeling integers are equivalent to the second Chern numbers which quantize 4D Hall effect. These topological characterization of energy gaps is generally applicable to any quasi-periodic systems having redundant reciprocal vectors more than spacial dimensions. If the system has n independent reciprocal lattice vectors in a d-dimensional space, we have ${}_nC_d$ different choices of the fundamental Brillouin zones. For example, the Penrose tile has 5 reciprocal vectors in 2 dimension, thus we have 10 fundamental Brillouin zones and zone quantum numbers.

In conclusion, the thesis established that energy gaps in quasi-periodic 2D systems must be labelled by a set of multiple topologically-invariant integers. The topological characterization proposed in this study can be applied to other quasi-periodic 2D systems, such as twisted trilayer graphene [61, 62, 63, 64], twisted bilayer graphene on hBN [113, 114, 115], 30° twisted bilayer graphene [39, 37, 41, 42], and also twisted trilayer of transiton metal dichalcogenides. The effective continuum approach combined with the commensurate approximant method employed in this thesis would be useful to capture the spectral features and the gap-labeling integers in incommensurate systems, which are typically challenging to address by the conventional atom-based methods.

Bibliography

[1] K. S. Novoselov, A. K. Geim, S. V. Morozov, D.-e. Jiang, Y. Zhang, S. V. Dubonos, I. V. Grigorieva, and A. A. Firsov, "Electric field effect in atomically thin carbon films," *science*, vol. 306, no. 5696, pp. 666–669, 2004.

[2] P. Wallace, "The band theory of graphite," *Phys. Rev.*, vol. 71, no. 9, p. 622, 1947.

[3] J. Hass, F. Varchon, J. Millan-Otoya, M. Sprinkle, N. Sharma, W. de Heer, C. Berger, P. First, L. Magaud, and E. Conrad, "Why multilayer graphene on 4h-sic (0001 [over]) behaves like a single sheet of graphene," *Phys. Rev. Lett.*, vol. 100, no. 12, p. 125504, 2008.

[4] J. Lopes dos Santos, N. Peres, and A. Castro Neto, "Graphene bilayer with a twist: Electronic structure," *Phys. Rev. Lett.*, vol. 99, no. 25, p. 256802, 2007.

[5] E. Mele, "Commensuration and interlayer coherence in twisted bilayer graphene," *Phys. Rev. B*, vol. 81, no. 16, p. 161405, 2010.

[6] G. Trambly de Laissardière, D. Mayou, and L. Magaud, "Localization of dirac electrons in rotated graphene bilayers," *Nano Lett.*, vol. 10, no. 3, pp. 804–808, 2010.

[7] S. Shallcross, S. Sharma, E. Kandelaki, and O. Pankratov, "Electronic structure of turbostratic graphene," *Phys. Rev. B*, vol. 81, no. 16, p. 165105, 2010.

[8] E. Morell, J. Correa, P. Vargas, M. Pacheco, and Z. Barticevic, "Flat bands in slightly twisted bilayer graphene: Tight-binding calculations," *Phys. Rev. B*, vol. 82, no. 12, p. 121407, 2010.

[9] R. Bistritzer and A. MacDonald, "Moiré bands in twisted double-layer graphene," *Proc. Natl. Acad. Sci.*, vol. 108, no. 30, p. 12233, 2011.

[10] P. Moon and M. Koshino, "Energy spectrum and quantum hall effect in twisted bilayer graphene," *Phys. Rev. B*, vol. 85, p. 195458, May 2012.

[11] G. T. de Laissardiere, D. Mayou, and L. Magaud, "Numerical studies of confined states in rotated bilayers of graphene," *Phys. Rev. B*, vol. 86, no. 12, p. 125413, 2012.

[12] Y. Cao, V. Fatemi, S. Fang, K. Watanabe, T. Taniguchi, E. Kaxiras, and P. Jarillo-Herrero, "Unconventional superconductivity in magic-angle graphene superlattices," *Nature*, vol. 556, no. 7699, p. 43, 2018.

[13] Y. Cao, V. Fatemi, A. Demir, S. Fang, S. L. Tomarken, J. Y. Luo, J. D. Sanchez-Yamagishi, K. Watanabe, T. Taniguchi, E. Kaxiras, R. C. Ashoori, and P. Jarillo-Herrero, "Correlated insulator behaviour at half-filling in magic-angle graphene superlattices," *Nature*, vol. 556, p. 80, 2018.

[14] L. Zou, H. C. Po, A. Vishwanath, and T. Senthil, "Band structure of twisted bilayer graphene: Emergent symmetries, commensurate approximants, and wannier obstructions," *Phys. Rev. B*, vol. 98, no. 8, p. 085435, 2018.

[15] M. Koshino, N. F. Yuan, T. Koretsune, M. Ochi, K. Kuroki, and L. Fu, "Maximally localized wannier orbitals and the extended hubbard model for twisted bilayer graphene," *Phys. Rev. X*, vol. 8, no. 3, p. 031087, 2018.

[16] X. Lu, P. Stepanov, W. Yang, M. Xie, M. A. Aamir, I. Das, C. Urgell, K. Watanabe, T. Taniguchi, G. Zhang, *et al.*, "Superconductors, orbital

magnets and correlated states in magic-angle bilayer graphene," *Nature*, vol. 574, no. 7780, pp. 653–657, 2019.

[17] M. Yankowitz, S. Chen, H. Polshyn, Y. Zhang, K. Watanabe, T. Taniguchi, D. Graf, A. F. Young, and C. R. Dean, "Tuning superconductivity in twisted bilayer graphene," *Science*, vol. 363, no. 6431, pp. 1059–1064, 2019.

[18] C. Berger, Z. Song, X. Li, X. Wu, N. Brown, C. Naud, D. Mayou, T. Li, J. Hass, A. N. Marchenkov, E. H. Conrad, P. N. First, and W. A. de Heer, "Electronic confinement and coherence in patterned epitaxial graphene," *Science*, vol. 312, no. 5777, pp. 1191–1196, 2006.

[19] G. Li, A. Luican, J. M. B. Lopes dos Santos, A. Neto, A. Reina, J. Kong, and E. Andrei, "Observation of van hove singularities in twisted graphene layers," *Nature Physics*, vol. 6, no. 2, pp. 109–113, 2009.

[20] D. Miller, K. Kubista, G. Rutter, M. Ruan, W. de Heer, P. First, and J. Stroscio, "Structural analysis of multilayer graphene via atomic moiré interferometry," *Phys. Rev. B*, vol. 81, no. 12, p. 125427, 2010.

[21] A. Luican, G. Li, A. Reina, J. Kong, R. Nair, K. Novoselov, A. Geim, and E. Andrei, "Single-layer behavior and its breakdown in twisted graphene layers," *Phys. Rev. Lett.*, vol. 106, no. 12, p. 126802, 2011.

[22] J. L. Dos Santos, N. Peres, and A. C. Neto, "Continuum model of the twisted graphene bilayer," *Physical review B*, vol. 86, no. 15, p. 155449, 2012.

[23] P. Moon and M. Koshino, "Optical absorption in twisted bilayer graphene," *Phys. Rev. B*, vol. 87, p. 205404, May 2013.

[24] N. R. Finney, M. Yankowitz, L. Muraleetharan, K. Watanabe, T. Taniguchi, C. R. Dean, and J. Hone, "Tunable crystal symmetry in graphene–boron

nitride heterostructures with coexisting moiré superlattices," *Nature nanotechnology*, vol. 14, no. 11, pp. 1029–1034, 2019.

[25] L. Wang, S. Zihlmann, M.-H. Liu, P. Makk, K. Watanabe, T. Taniguchi, A. Baumgartner, and C. Schönenberger, "New generation of moiré superlattices in doubly aligned hbn/graphene/hbn heterostructures," *Nano letters*, vol. 19, no. 4, pp. 2371–2376, 2019.

[26] Z. Wang, Y. B. Wang, J. Yin, E. Tóvári, Y. Yang, L. Lin, M. Holwill, J. Birkbeck, D. Perello, S. Xu, *et al.*, "Composite super-moiré lattices in double-aligned graphene heterostructures," *Sci. Adv.*, vol. 5, no. 12, p. eaay8897, 2019.

[27] Y. Yang, J. Li, J. Yin, S. Xu, C. Mullan, T. Taniguchi, K. Watanabe, A. K. Geim, K. S. Novoselov, and A. Mishchenko, "In situ twistronics of van der waals heterostructures," *Sci. Adv.*, vol. 6, no. 49, p. eabd3655, 2020.

[28] M. Onodera, K. Kinoshita, R. Moriya, S. Masubuchi, K. Watanabe, T. Taniguchi, and T. Machida, "Cyclotron resonance study of monolayer graphene under double moiré potentials," *Nano letters*, vol. 20, no. 6, pp. 4566–4572, 2020.

[29] M. Kuiri, S. K. Srivastav, S. Ray, K. Watanabe, T. Taniguchi, T. Das, and A. Das, "Enhanced electron-phonon coupling in doubly aligned hexagonal boron nitride bilayer graphene heterostructure," *Phys. Rev. B*, vol. 103, no. 11, p. 115419, 2021.

[30] M. Andelkovic, S. P. Milovanovic, L. Covaci, and F. M. Peeters, "Double moiré with a twist: Supermoiré in encapsulated graphene," *Nano letters*, vol. 20, no. 2, pp. 979–988, 2020.

[31] N. Leconte and J. Jung, "Commensurate and incommensurate double moire interference in graphene encapsulated by hexagonal boron nitride," *2D Materials*, vol. 7, no. 3, p. 031005, 2020.

[32] H. Oka and M. Koshino, "Fractal energy gaps and topological invariants in hbn/graphene/hbn double moiré systems," *Phys. Rev. B*, vol. 104, p. 035306, Jul 2021.

[33] M. Koshino and H. Oka, "Topological invariants in two-dimensional quasicrystals," *Physical Review Research*, vol. 4, no. 1, p. 013028, 2022.

[34] C. Dean, A. Young, I. Meric, C. Lee, L. Wang, S. Sorgenfrei, K. Watanabe, T. Taniguchi, P. Kim, K. Shepard, and J. Hone, "Boron nitride substrates for high-quality graphene electronics," *Nat. Nanotechnol.*, vol. 5, no. 10, pp. 722–726, 2010.

[35] D. Lee, C. Riedl, T. Beringer, A. Castro Neto, K. von Klitzing, U. Starke, and J. Smet, "Quantum hall effect in twisted bilayer graphene," *Phys. Rev. Lett.*, vol. 107, no. 21, p. 216602, 2011.

[36] J. D. Sanchez-Yamagishi, T. Taychatanapat, K. Watanabe, T. Taniguchi, A. Yacoby, and P. Jarillo-Herrero, "Quantum hall effect, screening, and layer-polarized insulating states in twisted bilayer graphene," *Phys. Rev. Lett.*, vol. 108, no. 7, p. 076601, 2012.

[37] P. Moon, M. Koshino, and Y.-W. Son, "Quasicrystalline electronic states in 30° rotated twisted bilayer graphene," *Phys. Rev. B*, vol. 99, no. 16, p. 165430, 2019.

[38] P. Stampfli, "A Dodecagonal Quasiperiodic Lattice in Two Dimensions," *Helv. Phys. Acta*, vol. 59, no. 5-7, pp. 1260–1263, 1986.

[39] S. J. Ahn, P. Moon, T.-H. Kim, H.-W. Kim, H.-C. Shin, E. H. Kim, H. W. Cha, S.-J. Kahng, P. Kim, M. Koshino, *et al.*, "Dirac electrons in a dodecagonal graphene quasicrystal," *Science*, vol. 361, no. 6404, pp. 782–786, 2018.

[40] W. Yao, E. Wang, C. Bao, Y. Zhang, K. Zhang, K. Bao, C. K. Chan, C. Chen, J. Avila, M. C. Asensio, *et al.*, "Quasicrystalline 30 twisted bilayer graphene as an incommensurate superlattice with strong interlayer coupling," *Proceedings of the National Academy of Sciences*, vol. 115, no. 27, pp. 6928–6933, 2018.

[41] J. A. Crosse and P. Moon, "Quasicrystalline electronic states in twisted bilayers and the effects of interlayer and sublattice symmetries," *Phys. Rev. B*, vol. 103, p. 045408, Jan 2021.

[42] H. Ha and B.-J. Yang, "Macroscopically degenerate localized zero-energy states of quasicrystalline bilayer systems in the strong coupling limit," *Phys. Rev. B*, vol. 104, p. 165112, Oct 2021.

[43] M. Kindermann, B. Uchoa, and D. Miller, "Zero-energy modes and gate-tunable gap in graphene on hexagonal boron nitride," *Phys. Rev. B*, vol. 86, no. 11, p. 115415, 2012.

[44] J. Wallbank, A. Patel, M. Mucha-Kruczyński, A. Geim, and V. I. Fal'ko, "Generic miniband structure of graphene on a hexagonal substrate," *Phys. Rev. B*, vol. 87, no. 24, p. 245408, 2013.

[45] M. Mucha-Kruczyński, J. Wallbank, and V. Fal'ko, "Heterostructures of bilayer graphene and h-bn: Interplay between misalignment, interlayer asymmetry, and trigonal warping," *Phys. Rev. B*, vol. 88, no. 20, p. 205418, 2013.

[46] J. Jung, A. Raoux, Z. Qiao, and A. H. MacDonald, "Ab initio theory of moiré superlattice bands in layered two-dimensional materials," *Phys. Rev. B*, vol. 89, no. 20, p. 205414, 2014.

[47] P. Moon and M. Koshino, "Electronic properties of graphene/hexagonal-boron-nitride moiré superlattice," *Phys. Rev. B*, vol. 90, p. 155406, Oct 2014.

[48] C. Dean, L. Wang, P. Maher, C. Forsythe, F. Ghahari, Y. Gao, J. Katoch, M. Ishigami, P. Moon, M. Koshino, T. Taniguchi, K. Watanabe, K. Shepard, J. Hone, and P. Kim, "Hofstadter/'s butterfly and the fractal quantum hall effect in moire superlattices," *Nature*, vol. 497, no. 7451, pp. 598–602, 2013.

[49] L. A. Ponomarenko, R. V. Gorbachev, G. L. Yu, D. C. Elias, R. Jalil, A. A. Patel, A. Mishchenko, A. S. Mayorov, C. R. Woods, J. R. Wallbank, M. Mucha-Kruczynski, B. A. Piot, M. Potemski, I. V. Grigorieva, K. S. Novoselov, F. Guinea, V. I. Fal'ko, and A. K. Geim, "Cloning of dirac fermions in graphene superlattices," *Nature*, vol. 497, no. 7451, pp. 594–597, 2013.

[50] B. Hunt, J. Sanchez-Yamagishi, A. Young, M. Yankowitz, B. LeRoy, K. Watanabe, T. Taniguchi, P. Moon, M. Koshino, P. Jarillo-Herrero, and R. Ashoori, "Massive dirac fermions and hofstadter butterfly in a van der waals heterostructure," *Science*, vol. 340, no. 6139, pp. 1427–1430, 2013.

[51] G. L. Yu, R. V. Gorbachev, J. S. Tu, A. V. Kretinin, Y. Cao, R. Jalil, F. Withers, L. A. Ponomarenko, B. A. Piot, M. Potemski, D. C. Elias, X. Chen, K. Watanabe, T. Taniguchi, I. V. Grigorieva, K. S. Novoselov, V. I. Fal'ko, A. K. Geim, and A. Mishchenko, "Hierarchy of hofstadter states and replica quantum hall ferromagnetism in graphene superlattices," *Nature physics*, vol. 10, pp. 525–529, 2014.

[52] J. Xue, J. Sanchez-Yamagishi, D. Bulmash, P. Jacquod, A. Deshpande, K. Watanabe, T. Taniguchi, P. Jarillo-Herrero, and B. LeRoy, "Scanning tunnelling microscopy and spectroscopy of ultra-flat graphene on hexagonal boron nitride," *Nat. Mater.*, vol. 10, no. 4, pp. 282–285, 2011.

[53] M. Yankowitz, J. Xue, and B. J. LeRoy, "Graphene on hexagonal boron nitride," *Journal of Physics: Condensed Matter*, vol. 26, no. 30, p. 303201, 2014.

[54] B. Sachs, T. Wehling, M. Katsnelson, and A. Lichtenstein, "Adhesion and electronic structure of graphene on hexagonal boron nitride substrates," *Phys. Rev. B*, vol. 84, no. 19, p. 195414, 2011.

[55] C. Ortix, L. Yang, and J. van den Brink, "Graphene on incommensurate substrates: Trigonal warping and emerging dirac cone replicas with halved group velocity," *Phys. Rev. B*, vol. 86, no. 8, p. 081405, 2012.

[56] M. Bokdam, T. Amlaki, G. Brocks, and P. J. Kelly, "Band gaps in incommensurable graphene on hexagonal boron nitride," *Phys. Rev. B*, vol. 89, p. 201404, May 2014.

[57] P. San-Jose, A. Gutiérrez-Rubio, M. Sturla, and F. Guinea, "Spontaneous strains and gap in graphene on boron nitride," *Phys. Rev. B*, vol. 90, no. 7, p. 075428, 2014.

[58] J. C. Song, P. Samutpraphoot, and L. S. Levitov, "Topological bloch bands in graphene superlattices," *Proceedings of the National Academy of Sciences*, vol. 112, no. 35, pp. 10879–10883, 2015.

[59] M. Neek-Amal and F. Peeters, "Graphene on boron-nitride: Moiré pattern in the van der waals energy," *Appl. Phys. Lett.*, vol. 104, no. 4, p. 041909, 2014.

[60] D. Hofstadter, "Energy levels and wave functions of bloch electrons in rational and irrational magnetic fields," *Phys. Rev. B*, vol. 14, no. 6, p. 2239, 1976.

[61] Z. Zhu, S. Carr, D. Massatt, M. Luskin, and E. Kaxiras, "Twisted trilayer graphene: a precisely tunable platform for correlated electrons," *Phys. Rev. Lett.*, vol. 125, no. 11, p. 116404, 2020.

[62] F. Lin, J. Qiao, J. Huang, J. Liu, D. Fu, A. S. Mayorov, H. Chen, P. Mukherjee, T. Qu, C.-H. Sow, *et al.*, "Heteromoiré engineering on magnetic bloch transport in twisted graphene superlattices," *Nano Letters*, vol. 20, no. 10, pp. 7572–7579, 2020.

[63] J. M. Park, Y. Cao, K. Watanabe, T. Taniguchi, and P. Jarillo-Herrero, "Tunable strongly coupled superconductivity in magic-angle twisted trilayer graphene," *Nature*, vol. 590, no. 7845, pp. 249–255, 2021.

[64] Z. Hao, A. Zimmerman, P. Ledwith, E. Khalaf, D. H. Najafabadi, K. Watanabe, T. Taniguchi, A. Vishwanath, and P. Kim, "Electric field–tunable superconductivity in alternating-twist magic-angle trilayer graphene," *Science*, vol. 371, no. 6534, pp. 1133–1138, 2021.

[65] X. Zhang, K.-T. Tsai, Z. Zhu, W. Ren, Y. Luo, S. Carr, M. Luskin, E. Kaxiras, and K. Wang, "Correlated insulating states and transport signature of superconductivity in twisted trilayer graphene superlattices," *Physical review letters*, vol. 127, no. 16, p. 166802, 2021.

[66] A. Fischer, Z. A. Goodwin, A. A. Mostofi, J. Lischner, D. M. Kennes, and L. Klebl, "Unconventional superconductivity in magic-angle twisted trilayer graphene," *npj Quantum Materials*, vol. 7, no. 1, p. 5, 2022.

[67] Y. Mao, D. Guerci, and C. Mora, "Supermoiré low-energy effective theory of twisted trilayer graphene," *Physical Review B*, vol. 107, no. 12, p. 125423, 2023.

[68] C. Mora, N. Regnault, and B. A. Bernevig, "Flatbands and perfect metal in trilayer moiré graphene," *Physical review letters*, vol. 123, no. 2, p. 026402, 2019.

[69] J.-M. Gambaudo and P. Vignolo, "Brillouin zone labelling for quasicrystals," *New J. Phys.*, vol. 16, no. 4, p. 043013, 2014.

[70] A. Smith and N. Ashcroft, "Pseudopotentials and quasicrystals," *Phys. Rev. Lett.*, vol. 59, no. 12, p. 1365, 1987.

[71] M. Verbin, O. Zilberberg, Y. E. Kraus, Y. Lahini, and Y. Silberberg, "Observation of topological phase transitions in photonic quasicrystals," *Phys. Rev. Lett.*, vol. 110, no. 7, p. 076403, 2013.

[72] C. Janot, "Quasicrystals," in *Neutron and Synchrotron Radiation for Condensed Matter Studies: Applications to Solid State Physics and Chemistry*, pp. 197–211, Springer, 1994.

[73] D. Levine and P. J. Steinhardt, "Quasicrystals: a new class of ordered structures," *Physical review letters*, vol. 53, no. 26, p. 2477, 1984.

[74] F. Mei, S.-L. Zhu, Z.-M. Zhang, C. Oh, and N. Goldman, "Simulating z 2 topological insulators with cold atoms in a one-dimensional optical lattice," *Physical Review A*, vol. 85, no. 1, p. 013638, 2012.

[75] H. M. Price, O. Zilberberg, T. Ozawa, I. Carusotto, and N. Goldman, "Four-dimensional quantum hall effect with ultracold atoms," *Phys. Rev. Lett.*, vol. 115, no. 19, p. 195303, 2015.

[76] K. Viebahn, M. Sbroscia, E. Carter, J.-C. Yu, and U. Schneider, "Matter-wave diffraction from a quasicrystalline optical lattice," *Physical review letters*, vol. 122, no. 11, p. 110404, 2019.

[77] L. Sanchez-Palencia and L. Santos, "Bose-einstein condensates in optical quasicrystal lattices," *Physical Review A*, vol. 72, no. 5, p. 053607, 2005.

[78] A. Uri, S. C. de la Barrera, M. T. Randeria, D. Rodan-Legrain, T. Devakul, P. J. D. Crowley, N. Paul, K. Watanabe, T. Taniguchi, R. Lifshitz,

L. Fu, R. C. Ashoori, and P. Jarillo-Herrero, "Superconductivity and strong interactions in a tunable moiréquasicrystal," *Nature*, vol. 620, no. 7975, pp. 762–767, 2023.

[79] Y. E. Kraus, Z. Ringel, and O. Zilberberg, "Four-dimensional quantum hall effect in a two-dimensional quasicrystal," *Phys. Rev. Lett.*, vol. 111, no. 22, p. 226401, 2013.

[80] D.-T. Tran, A. Dauphin, N. Goldman, and P. Gaspard, "Topological hofstadter insulators in a two-dimensional quasicrystal," *Phys. Rev. B*, vol. 91, no. 8, p. 085125, 2015.

[81] M. A. Bandres, M. C. Rechtsman, and M. Segev, "Topological photonic quasicrystals: Fractal topological spectrum and protected transport," *Physical Review X*, vol. 6, no. 1, p. 011016, 2016.

[82] J. D. Cain, A. Azizi, M. Conrad, S. M. Griffin, and A. Zettl, "Layer-dependent topological phase in a two-dimensional quasicrystal and approximant," *Proceedings of the National Academy of Sciences*, vol. 117, no. 42, pp. 26135–26140, 2020.

[83] M. I. Rosa, M. Ruzzene, and E. Prodan, "Topological gaps by twisting," *Communications Physics*, vol. 4, no. 1, pp. 1–10, 2021.

[84] M. Fujimoto, H. Koschke, and M. Koshino, "Topological charge pumping by a sliding moiré pattern," *Phys. Rev. B*, vol. 101, no. 4, p. 041112, 2020.

[85] Y. Zhang, Y. Gao, and D. Xiao, "Topological charge pumping in twisted bilayer graphene," *Phys. Rev. B*, vol. 101, no. 4, p. 041410, 2020.

[86] Y. Su and S.-Z. Lin, "Topological sliding moiré heterostructure," *Phys. Rev. B*, vol. 101, no. 4, p. 041113, 2020.

[87] L.-J. Lang, X. Cai, and S. Chen, "Edge states and topological phases in one-dimensional optical superlattices," *Phys. Rev. Lett.*, vol. 108, no. 22, p. 220401, 2012.

[88] Y. E. Kraus, Y. Lahini, Z. Ringel, M. Verbin, and O. Zilberberg, "Topological states and adiabatic pumping in quasicrystals," *Phys. Rev. Lett.*, vol. 109, no. 10, p. 106402, 2012.

[89] Y. E. Kraus and O. Zilberberg, "Topological equivalence between the fibonacci quasicrystal and the harper model," *Phys. Rev. Lett.*, vol. 109, no. 11, p. 116404, 2012.

[90] I. I. Satija and G. G. Naumis, "Chern and majorana modes of quasiperiodic systems," *Phys. Rev. B*, vol. 88, no. 5, p. 054204, 2013.

[91] S. Ganeshan, K. Sun, and S. D. Sarma, "Topological zero-energy modes in gapless commensurate aubry-andré-harper models," *Phys. Rev. Lett.*, vol. 110, no. 18, p. 180403, 2013.

[92] M. Verbin, O. Zilberberg, Y. Lahini, Y. E. Kraus, and Y. Silberberg, "Topological pumping over a photonic fibonacci quasicrystal," *Phys. Rev. B*, vol. 91, no. 6, p. 064201, 2015.

[93] M. Lohse, C. Schweizer, O. Zilberberg, M. Aidelsburger, and I. Bloch, "A thouless quantum pump with ultracold bosonic atoms in an optical superlattice," *Nature Physics*, vol. 12, no. 4, pp. 350–354, 2016.

[94] P. Marra and M. Nitta, "Topologically quantized current in quasiperiodic thouless pumps," *Phys. Rev. Res.*, vol. 2, no. 4, p. 042035, 2020.

[95] O. Zilberberg, "Topology in quasicrystals," *Optical Materials Express*, vol. 11, no. 4, pp. 1143–1157, 2021.

[96] M. Yoshii, S. Kitamura, and T. Morimoto, "Topological charge pumping in quasiperiodic systems characterized by the bott index," *Phys. Rev. B*, vol. 104, no. 15, p. 155126, 2021.

[97] D. Thouless, "Quantization of particle transport," *Phys. Rev. B*, vol. 27, no. 10, p. 6083, 1983.

[98] Q. Niu, "Quantum adiabatic particle transport," *Phys. Rev. B*, vol. 34, no. 8, p. 5093, 1986.

[99] T. Ando, "Theory of electronic states and transport in carbon nanotubes," *J. Phys. Soc. Jpn.*, vol. 74, no. 3, pp. 777–817, 2005.

[100] M. Koshino, "Interlayer interaction in general incommensurate atomic layers," *New J. Phys.*, vol. 17, no. 1, p. 015014, 2015.

[101] J. Slater and G. Koster, "Simplified lcao method for the periodic potential problem," *Phys. Rev.*, vol. 94, no. 6, p. 1498, 1954.

[102] J. Sławińska, I. Zasada, and Z. Klusek, "Energy gap tuning in graphene on hexagonal boron nitride bilayer system," *Phys. Rev. B*, vol. 81, no. 15, p. 155433, 2010.

[103] L. Liu, Y. Feng, and Z. Shen, "Structural and electronic properties of h-bn," *Phys. Rev. B*, vol. 68, no. 10, p. 104102, 2003.

[104] P. G. Harper, "The general motion of conduction electrons in a uniform magnetic field, with application to the diamagnetism of metals," *Proceedings of the Physical Society. Section A*, vol. 68, no. 10, p. 879, 1955.

[105] S. Aubry and G. André, "Analyticity breaking and anderson localization in incommensurate lattices," *Ann. Israel Phys. Soc*, vol. 3, no. 133, p. 18, 1980.

[106] S. Walter and S. Deloudi, *Crystallography of quasicrystals: concepts, methods and structures*, vol. 126. Springer Science & Business Media, 2009.

[107] N. W. Ashcroft, N. D. Mermin, *et al.*, *Solid state physics*, vol. 2005. Saunders College, Philadelphia,, 1976.

[108] X.-L. Qi, T. L. Hughes, and S.-C. Zhang, "Topological field theory of time-reversal invariant insulators," *Phys. Rev. B*, vol. 78, no. 19, p. 195424, 2008.

[109] H. M. Price, O. Zilberberg, T. Ozawa, I. Carusotto, and N. Goldman, "Measurement of chern numbers through center-of-mass responses," *Phys. Rev. B*, vol. 93, no. 24, p. 245113, 2016.

[110] M. Lohse, C. Schweizer, H. M. Price, O. Zilberberg, and I. Bloch, "Exploring 4d quantum hall physics with a 2d topological charge pump," *Nature*, vol. 553, no. 7686, pp. 55–58, 2018.

[111] O. Zilberberg, S. Huang, J. Guglielmon, M. Wang, K. P. Chen, Y. E. Kraus, and M. C. Rechtsman, "Photonic topological boundary pumping as a probe of 4d quantum hall physics," *Nature*, vol. 553, no. 7686, pp. 59–62, 2018.

[112] L. Lu, H. Gao, and Z. Wang, "Topological one-way fiber of second chern number," *Nat. Commun.*, vol. 9, no. 1, pp. 1–7, 2018.

[113] J. Shi, J. Zhu, and A. MacDonald, "Moiré commensurability and the quantum anomalous hall effect in twisted bilayer graphene on hexagonal boron nitride," *Phys. Rev. B*, vol. 103, no. 7, p. 075122, 2021.

[114] J. Shin, Y. Park, B. L. Chittari, J.-H. Sun, and J. Jung, "Electron-hole asymmetry and band gaps of commensurate double moire patterns in twisted bilayer graphene on hexagonal boron nitride," *Phys. Rev. B*, vol. 103, no. 7, p. 075423, 2021.

[115] X. Huang, L. Chen, S. Tang, C. Jiang, C. Chen, H. Wang, Z.-X. Shen, H. Wang, and Y.-T. Cui, "Moiré imaging in twisted bilayer graphene aligned on hexagonal boron nitride," *arXiv preprint arXiv:2102.08594*, 2021.

Acknowledgement

First and foremost, I would like to express my deep gratitude to my supervisor, Prof. Mikito Koshino. His long-term guidance, keen observations, continuous support, in-depth professional discussions, and valuable advice have enabled me to complete this research. Especially during times when the results did not meet my expectations, his generous support was a significant strength to me. His interest and enthusiasm in discussing my research are irreplaceable to me.

Similarly, I extend my heartfelt thanks to Prof. Takuto Kawakami. He consistently responded to various questions, doubts, and concerns that I had during the progressing of my research, allowing me to consult with him with peace of mind.

Additionally, I sincerely thank Prof. Kazuhiko Kuroki, Prof. Tetsuya Onogi, and Prof. Yasuhiro Niimi for participating as committee members in the defense of my dissertation. Their insightful questions and meaningful comments greatly enhanced the value of my research.

I also express my gratitude to all the members of the laboratory, especially Mr. Manato Fujimoto, Mr. Masaru Hitomi, and Mr. Naoto Nakatsuji. The daily discussions and enjoyable casual conversations have been a significant motivation for me. I am particularly grateful to Mr. Kazuki Yamamoto for advancing research related to my study. My thanks also go to the secretaries, Ms. Mari Homma and Ms. Yuki Harada. Their everyday conversations and consultations provided me with much encouragement and courage, for which I am deeply grateful. Once again, I would like to thank all the members of the laboratory.

I owe a deep sense of gratitude to the Interactive Materials Science Cadet Program. This program allowed me to learn about materials science from multiple perspectives, meet people from other fields, and gain valuable experiences. I received a lot of valuable pieces of advice from Prof. Kenji Iijima, which came from his broad perspective and experience. I am also very thankful to the secretaries, Ms. Miwa Shimizu, Ms. Yasuko Ueda, and Ms. Aki Okubo for their support beyond the program framework. Additionally, the financial assistance from the Project of Support for Pioneering Research Initiated by the Next Generation in Osaka University was a significant support in continuing my doctoral course.

Finally, I would like to express my gratitude to my family, especially my parents, Masaki Oka and Tamiko Oka. Although they humbly expressed that they couldn't understand the content of my research, their constant support and understanding were crucial in my ability to continue my studies.

In conclusion, I am grateful for encountering this research topic. The journey was challenging at times, but the theme itself was very attractive, and I feel fortunate to have been involved in this non-trivial problem. In completing this study, I dedicate my heartfelt thanks to everyone and everything involved.